

# Linking in situ Crystallisation and Magma Replenishment via Sill Intrusion in the Rum Western Layered Intrusion, NW Scotland

**DOI:**
10.1093/petrology/egy073

**Document Version**
Accepted author manuscript



# Linking *in situ* Crystallisation and Magma Replenishment *via* Sill Intrusion in the Rum Western Layered Intrusion, NW Scotland

Luke N. Hepworth[1*], Brian O'Driscoll[2*], Ralf Gertisser[1], J. Stephen Daly[3,4], C. Henry Emeleus[5]

[1]*School of Geography, Geology, and the Environment, Keele University, Keele ST5 5BG, UK*

[2]*School of Earth and Environmental Sciences, University of Manchester, Oxford Road, Manchester M13 9PL, UK;*

[3]*UCD School of Earth Sciences and UCD Earth Institute, University College Dublin, Belfield, Dublin 4, Ireland*

[4]*Irish Centre for Research in Applied Geosciences, Belfield, Dublin 4, Ireland*

[5]*Department of Earth Sciences, Durham University, South Road, Durham DH1 3LE, UK*

[*]Corresponding authors: l.n.hepworth@keele.ac.uk; brian.odriscoll@manchester.ac.uk

## ABSTRACT

The construction of layered mafic-ultramafic intrusions has traditionally been attributed to gravity-driven accumulation, involving the mechanical settling of crystals onto the magma chamber floor, at the interface between the crystal mush at the base and overlying replenishing magma, such that the layered sequence of cumulates (i.e., the crystal mush) at the floor aggrades upwards. The Rum Western Layered Intrusion (WLI) is a ~250 m sequence of layered peridotite cumulates comprising the structurally lowest portion of the Rum Layered Suite (RLS). As such, it is taken to represent the oldest sequence in the RLS and has been assumed to young upwards. The WLI hosts the largest proportion of harrisite, a cumulate composed of skeletal olivine that formed by *in situ* crystallisation, in the Rum layered intrusion. Harrisite layers in the WLI ubiquitously exhibit extremely irregular upward-oriented apophyses, up to several metres high and metres across, alongside laterally extensive dome-like structures; features consistent with intrusive, sill-like emplacement of harrisite. The distribution and abundance of harrisite therefore points to chaotic sill-like emplacement of the magmas that produced at least half of the WLI cumulate. This probably occurred various ambient crystal mush temperatures and punctuated intervals during cumulate formation. The harrisite layers

are associated with numerous Cr-spinel seams occurring along the tops, bases, and interiors of these layers, suggesting they formed *in situ* alongside harrisite sills within the crystal mush. Detailed quantitative textural and mineral chemical analysis of Cr-spinel seams support a simple *in situ* crystallisation process for their formation. It is suggested the Cr-spinel seams form within melt channels that develop along the same hot tears that allowed the harrisite parental melts to enter the crystal mush. The chemistry and texture of Cr-spinel is controlled by the volume of through-flow of melt through the melt channel. Where melt flux through channels was high, sulphide and platinum-group minerals are more abundant, highlighting the key economic implications of this model for the platinum-group element enrichment of chromitite horizons in layered intrusions. We also highlight the role of infiltration metasomatism at multiple levels of the WLI, where porous percolation of interstitial melt and reactive liquid flow played a key role in cumulate formation, supporting the notion of layered intrusion growth by incremental sill emplacement.

**Keywords:** harrisite; Cr-spinel; *in situ* crystallisation; sill emplacement; crystal mush, infiltration metasomatism

## INTRODUCTION

Our understanding of the way that layered mafic-ultramafic intrusions are constructed is dominated by gravity-driven accumulation, where crystal settling from a column of magma produces a crystal pile at the magma chamber floor (Wager & Deer, 1939; Brown, 1956; Wager *et al*., 1960; Jackson, 1961; Wadsworth, 1961; Emeleus *et al*., 1996; Campbell, 1978; Sparks & Huppert, 1984; Huppert *et al*., 1986; McBirney & Nicolas, 1997; Holness, 2005; 2007; Tegner *et al*., 2009; Brandiss *et al*., 2014; Holness *et al*, 2017; O'Driscoll & VanTongeren, 2017). In open systems, replenishing magma enters the chamber at the interface between the resident magma and the crystal pile. Long-held views envisage the crystal mush at the floor of the magma chamber solidifying as a static mass, which may undergo chemical and thermal exchange with the magma above but is kinematically immobile (see discussion by Maier *et al*., 2013 and references therein). Alternative models for layered intrusion development by *in situ* crystallisation focus on a boundary layer at the magma chamber floor and

around the intrusion margins as the zone where intrusion growth primarily occurs (O'Driscoll *et al*., 2010; Latypov *et al*., 2013; Latypov *et al*., 2015).

The recent identification of out-of-sequence (not upward forming order) layers in the Bushveld Complex (South Africa) by Mungall *et al.* (2016), as well as in the Stillwater Complex by Wall *et al* (2018), by applying high-precision U-Pb geochronology has cast doubt on the classic paradigm that all layered intrusions are constructed from the bottom up. Although controversial, Mungall *et al.* (2016) suggest that the platinum-enriched horizons are associated with out-of-sequence layers, which develop due to sill-emplacement into semi- or completely solidified cumulate. Layered intrusion formation by sill emplacement, where magma replenishment occurs into the crystal mush, has been invoked for other layered intrusions (including Rum) based on detailed field evidence (e.g., Bédard *et al*., 1988; Tegner & Robins, 1996; Hepworth *et al*., 2017). The mechanisms of sill-emplacement in layered intrusions require careful consideration of the physical and mechanical state of the crystal framework being intruded (Marsh, 2002; Holness *et al*., 2007; Humphreys & Holness, 2010; Namur *et al*., 2013; Hepworth *et al*., 2017). Enhancing our understanding of the behaviour of the crystal mush and the complex physical and chemical processes that may occur within a semi-solid framework during syn-magmatic intrusion is thus an important goal in further elucidating the mechanisms by which the precious-metal deposits typically associated with these layered mafic-ultramafic intrusions form, as well as the formation of layered intrusions more generally.

In this contribution, we argue for non-traditional models of layered intrusion construction, i.e., sill emplacement. We present detailed field and petrological observations of the Rum Western Layered Intrusion (WLI; NW Scotland) and discuss the physical, thermal, and chemical processes occurring *within* the crystal mush that produced the WLI, including a detailed discussion on harrisite sills. We argue that our combined evidence points to a sequence of cumulate in the WLI that does not young upwards and propose instead that the WLI represents a dynamic and incrementally developed crystal mush that was intruded repeatedly by picritic and basaltic magmas. A model is also presented for the petrogenesis of Cr-spinel seams throughout the WLI, whereby seams represent melt channels formed along hot tears or shear zones that form within the crystal mush. Our conclusions highlight implications for the associated platinum-group element (PGE) concentration that must also occur

within the crystal mush, with key insights for mineralisation in much larger, economically exploited layered intrusions.

## GEOLOGICAL SETTING

### The Rum Layered Suite

The Rum Layered Suite (RLS) is a classic example of an open-system layered intrusion. It formed at 60.53 ±0.08 Ma (Hamilton *et al*., 1998) as part of the British and Irish Palaeogene Igneous Province (BIPIP; Emeleus *et al*. 1996; Emeleus & Bell, 2005; Emeleus & Troll, 2014). The RLS can be divided into three distinct portions; the Eastern Layered Intrusion (ELI), the Central Intrusion (CI), and the Western Layered Intrusion (WLI; see below) (Fig. 1). The ELI is well-studied and has traditionally been held up as a type example of open-system magma chamber behaviour, with each major successive replenishment event represented by the sixteen coupled peridotite-troctolite ± olivine gabbro macro-rhythmic units that comprise the intrusion (Brown, 1956; Volker & Upton, 1990). Early models invoked batch fractionation of successive cumulus phases and crystal settling to account for the transition from ultramafic to felsic cumulate, which was adapted where field observations pointed to multiple replenishment events within a single unit (e.g., Renner & Palacz, 1987; Holness *et al*., 2005; Holness & Winpenny, 2008). The construction of the ELI from the bottom up has been challenged for specific parts of its stratigraphy over the past ~30 years. Bédard *et al*. (1988) suggested that much of the upper portion of the ELI was emplaced as sills. Holness *et al*. (2005; 2007) focused on the Unit 9 peridotite and demonstrated that it was likely to have been emplaced into a pre-existing crystal mush, by documenting the effects of magma intrusion on the overlying cumulate. More recently, a detailed study of Unit 10 reported evidence for the peridotite portion forming incrementally, from numerous, small volume replenishment events within the crystal mush (Hepworth *et al*., 2017).

### The Western Layered Intrusion

The WLI comprises the structurally lowest portion of the RLS and can be sub-divided into three composite parts (Fig. 2), from top to bottom as follows: the Ard Mheall Member (AMP), the

Transitional Member (TSM), and the Harris Bay Member (HBM) (Wadsworth, 1961). Unlike the ELI, the WLI consists almost entirely of layered peridotite. The WLI (specifically 'Harris Bay') is the type locality of harrisite (Harker, 1908), an unusual variety of olivine cumulate comprising coarse, skeletal, branching and hopper olivine morphologies (Donaldson, 1974; O'Driscoll *et al*., 2007a). Harrisite is a key example of *in situ* crystallisation in layered intrusions, first documented by Wager *et al*. (1960). By comparison with the ELI, the WLI has lacked detailed attention in the literature for the past ~60 years. The most recent comprehensive description of the WLI is by Wadsworth (1961), whilst more recent research has focused on specific aspects of the petrogenesis of harrisite (e.g., Donaldson, 1974; 1976; 1982; O'Driscoll *et al*., 2007a). Wadsworth (1961) suggested that, much like the ELI, the WLI also represents an open-system, formed of multiple replenishment events. In the absence of obvious macro-rhythmic units, these replenishment events were suggested by Wadsworth to be recorded by harrisite layers, with so-called 'normal' or granular-textured peridotite representing periods between replenishment events, the latter formed by crystal settling of olivine from the overlying magma. Subsequently, the limited number of investigations into the formation of the WLI has broadly supported these ideas but has revealed more complexity in the variety of inferred magma chamber processes, such as invoking mobilisation of crystal slurries from unstable sidewalls (e.g., Worrell, 2002; O'Driscoll *et al*., 2007a). O'Driscoll *et al*. (2007a) supported some of the original concepts of Wadsworth (1961), highlighting the importance of the small volume replenishment events, and pointing to rapid crystallisation of harrisite from deeply undercooled picritic magma. The latter authors envisaged these processes operating on the magma chamber floor, with crystal settling or density current deposition considered to be the main process responsible for the formation of the granular-textured peridotite between picritic replenishment events.

## FIELD RELATIONSHIPS

Many of the lithologies described here, such as harrisite and some granular-textured peridotites, are not true peridotites in that they contain <50 vol.% olivine. They are more accurately classified as olivine gabbro, troctolite, or melatroctolite in the scheme of Le Maitre (2002). However, for ease of comparison with the previous literature, we refer to WLI lithologies containing skeletal (or hopper)

olivine crystals and intercumulus plagioclase ± clinopyroxene as harrisite, and granular olivine-textured rocks as 'peridotites', or as 'feldspathic peridotite' where particularly plagioclase-rich. Where clinopyroxene is a particularly prominent intercumulus phase (>30 vol.%), as in some of the Transitional Member rocks, the prefix 'wehrlitic' is applied, and 'dunitic' to distinguish particularly high (>90 vol.%) cumulus olivine contents. Thus, a 'wehrlitic peridotite' is a rock comprising abundant cumulus olivine plus intercumulus plagioclase, with >30 vol.% intercumulus clinopyroxene.

**The Western Layered Intrusion**

The WLI was remapped as part of this study (Fig. 2). Our new map distinguishes the same three members as Wadsworth (1961), but here we propose a new sub-division of the Ard Mheall Member; the Ard Mheall Peridotite (AMP) and Upper Ard Mheall Peridotite (UAM). The exposed WLI is a roughly 'half-bowl'-shaped layered body that dips shallowly towards the Long Loch Fault (LLF), the putative feeder zone in the centre of the RLS (Fig. 1). The dip of layering varies between the UAM/AMP, TSM and HBM. The dip of the layering across all parts of the WLI generally steepens with proximity to the LLF (to ~60°), with the AMP/UAM showing an average dip of ~20° to the east. Some layers within the UAM are noted to dip westward at roughly 20°, a feature that is variable throughout the member. The TSM dips ~20° to the west like the overlying AMP. The HBM is much shallower, dipping ~10° to the west, and its layers are horizontal with distance away from the LLF (i.e., in the lower portions of the HBM). Thickness estimates of the different members are consistent with those of Wadsworth (1961); the HBM is ~120 m thick, the TSM is ~53 m, and the AMP (incl. UAM) is ~245 m thick, totalling approximately 420 m of WLI peridotite cumulate (see Online Appendix 1). The contact between the AMP and TSM appears gradual over a vertical distance of a few metres, marked by a noticeable change in lithology (to wehrlitic-peridotite). The boundary between the TSM and HBM is exposed on the south-eastern edge of the WLI, where there is a sharp change from olivine-gabbros to wehrlitic peridotite.

**Ard Mheall Member**

*Ard Mheall Peridotite (AMP)*

The AMP is the thickest peridotite body in the WLI, comprising approximately 245 m of well-layered peridotites that host ubiquitous Cr-spinel seams throughout. It is well-exposed all around Ard Mheall Mountain, where the layering dips shallowly (10–15º) towards the CI (Fig. 2), with less exposure in the east where the dip of layering also becomes much steeper (40–60º). The AMP was logged in eight sections across the WLI; the complete high-resolution versions of the logs are accessible in Online Appendix 2. Correlation of individual layers or even packages of layers is not possible over distances of more than a few hundreds of metres. Petrological 'facies' have been identified in the logged sections, which illustrate peridotite variation (and features), and also the relationships between peridotite and Cr-spinel seams. A summary of the petrological facies scheme is illustrated in Figure 3.

*Harrisite*

Harrisite is the most common peridotite in the AMP and comprises texturally variable olivine crescumulate–orthocumulates (see Wager *et al*., 1960). Harrisite layer thicknesses range considerably (i.e., <0.1 m to >5 m). Individual harrisite layers may vary in thickness along strike as well as taper, bifurcate, and terminate (Facies A; Figs. 3; 4a). While harrisite layers are generally stratabound in nature and define the most obvious layering present in the WLI, the topology of the upper and lower surfaces of each layer can vary significantly (Fig. 4b–e). Harrisite layers can be flat on both bounding surfaces, or more commonly display prominent apophyses on their upper surfaces (Fig. 4b; Facies B). Undulose 'erosional' bases (Fig. 3; Facies B) including rarer undercutting apophyses on their lower surfaces (Fig. 4d) are also observed. The latter features are not mutually exclusive and can occur together in individual layers. The apophyses commonly found in harrisites in the WLI range in amplitude from several centimetres to several metres in height. In the case of metre-scale structures, they clearly cross-cut existing magmatic layering in granular-textured peridotite (Figs 3: Facies C; 4e;). Dome-like protrusions of harrisite are also documented, that cross-cut 2–3 metres of overlying layering but extend for >10 m laterally (Fig. 3; Facies D). Thick bodies (>1 m) of harrisite contain internal layering defined by variable olivine crystal morphology i.e., composite layers (Fig. 3; Facies E). Morphological variation in olivine can be significant between layers, although generally hopper

morphologies dominate over branching and dendritic forms (Fig. 4f). There does not appear to be any consistent relationship between olivine morphology and layer thickness, but there is a correlation of olivine morphology with structural height through the AMP, with the base containing the highest concentration of skeletal and branching olivine habits, while the central and upper portions of the AMP contain finer-grained hopper olivine. The morphologies of olivine crystals within individual layers (typically <1 mm) occasionally change at the base of the layer, with hopper varieties grading into more branching and skeletal varieties with height in the layer (Fig. 3; Facies F). Granular-textured peridotite autoliths are observed in harrisite layers throughout the AMP ranging from <5 cm to >1 m in diameter (Fig. 3; Facies G). Foliation of olivine is observed at the outcrop-scale within harrisite. This foliation is non-pervasive but can trace out dome-like structures (Fig. 4g) from the alignment of elongate, branching olivine crystals (Figs.3; Facies H; 4j). Vertical (and sub-vertical) plagioclase veining is seen most commonly with height approaching the UAM. Clinopyroxene and gabbroic pegmatite veins occur sparsely.

*Granular-textured peridotite*

Granular-textured peridotite is abundant throughout the AMP. It generally has significantly less intercumulus material (i.e., plagioclase and clinopyroxene) than harrisite (i.e., <15 vol.%). Packages of granular-textured peridotite are often internally layered, with a relatively limited range of layer thicknesses (5–20 cm). Layering is generally defined by the presence of Cr-spinel seams. Layering can also be defined by a gradational reduction in porosity (vol.% intercumulus proportion) towards the top of an individual layer, reversing sharply with the successive layer, often repeating several times in thicker sections of layered rock (Fig. 3; Facies I). Perturbations in fine-scale layering occur in close proximity to harrisite layers with high-amplitude apophyses, such as the upward flexure of layering adjacent to vertical harrisite contacts (Fig. 4e). Blocks of layered granular-textured peridotite are incorporated into harrisite, and from the random attitudes of the layering can be seen to have undergone some rotation (Fig. 4i). Coarser-grained (~2–3 mm olivine) bodies of granular-textured peridotite taper and terminate like harrisite layers. Where lateral variations in layer thickness occur, irregular upper surfaces may also be present (Fig. 3; Facies A and L). An alternating relationship

between coarse (~2 mm olivine) and finer-grained (≤1 mm olivine) granular-textured peridotite is common, where fine-grained peridotite with a lower proportion of intercumulus material (<10%) occurs between coarser-grained (and Cr-spinel seam bearing) peridotite bodies (Fig. 3; Facies J), with a similar relationship between harrisite and granular-textured peridotite. Layer parallel foliation defined by the preferred alignment of tabular olivine crystals is common in granular-textured peridotites and is variably pervasive at the outcrop-scale. In both harrisite and granular-textured peridotite, clinopyroxene content broadly increases approaching the UAM (where it is >15 vol.%) though this abundance can still vary from layer to layer.

*Porphyritic peridotite*

A third peridotite type can be identified in the AMP termed 'porphyritic peridotite'. This peridotite forms layers much like the granular-textured peridotite, but contains large, up to 7 cm long megacrysts of hopper and tabular olivine (Fig. 4j). The proportion of the olivine megacrysts varies significantly, sometimes comprising the bulk of thin peridotite layers or as low as 5 vol.% of a layer (Figs. 3; Facies K; 4j). The host material is always fine to medium-grained granular-textured peridotite. Porphyritic-peridotite layers where the olivine megacrysts comprise a significant proportion (i.e., >50 vol.%) of the layer are ubiquitously thin (<5 cm), and often repeated in regular intervals (see Online Appendix 2). Megacrysts are often common with proximity to harrisite bodies, but this is not consistent throughout the AMP (Fig. 3; Facies K). Porphyritic peridotite bodies typically exhibit a strong foliation, defined by the olivine megacrysts, though fine-grained olivine crystals in the groundmass also contribute to the foliation in these cases. O'Driscoll *et al*. (2007a; 2015) reported imbrication-like structures in some of the olivine megacrystic layers. This feature was not observed during this investigation.

*Cr-spinel seams*

Cr-spinel seams are extremely abundant in the AMP (see logs in Online Appendix 2), occurring in all varieties of peridotite. Individual seams are not laterally extensive and can rarely be traced for more than several tens of metres along strike. The thickness of Cr-spinel seams is highly variable, ranging

from 2–30 mm. The thickness of individual seams can vary laterally over several metres, as can the modal abundance of Cr-spinel in seams. Discrete layers of granular-textured peridotite can be relatively enriched in Cr-spinel, creating diffuse seams up to 5 cm thick which can be traced for several tens of metres. The textures of many of the Cr-spinel seams in the AMP (and WLI more broadly) are comparable to those in the Unit 12 and Unit 10 peridotite in the ELI, which were described as 'chain-textured' by O'Driscoll *et al*. (2010) and Hepworth *et al*. (2017). This texture is characterised by Cr-spinel forming chain-like aggregates around cumulus olivine crystals. The intercumulus silicate fraction comprises plagioclase with rare clinopyroxene. Unlike Cr-spinel seams in the Unit 12 and 10 peridotites, seams in the WLI can also be formed of chromitite (>60 vol.% Cr-spinel), containing little to no cumulus olivine at all. Thus, the AMP Cr-spinel seams can be divided into similar groups as those suggested for Unit 10 by Hepworth *et al.* (2017), based on their relationship to their host peridotite: granular-textured peridotite-hosted seams, boundary seams, harrisite-hosted seams, foliated peridotite-hosted seams, and an additional group of chromitite seams.

Granular-textured peridotite-hosted seams exhibit no textural or mineralogical variation in the peridotite above or below the seam (Figs. 3; Facies I) and can be undulose (Figs. 4h; 5a). Boundary seams occur with a distinct textural or mineralogical variation in the peridotite on either side of the seam, e.g., a Cr-spinel seam between harrisite and granular-textured peridotite (Fig. 5b). Boundary Cr-spinel seams occur on the base (Fig. 3; Facies L), the top (Fig. 3; Facies M), or more rarely both surfaces of harrisite and granular-textured peridotite layers (Fig. 3; Facies N). Foliated peridotite (including harrisite)-hosted seams occur where cumulus olivine defines a foliation within (and less commonly outside) the upper and lower limits of the Cr-spinel seam. Harrisite-hosted seams occur within harrisite layers and contain Cr-spinel that is coarse-grained (>1 mm in diameter). Chromitite seams have little (<5%) or no cumulus olivine within the limits of the Cr-spinel seam and tend to be particularly thick (>10 mm) (Fig. 5c). Chromitite seams are most commonly found within harrisite layers but can also occur within granular-textured peridotite. Chromitites can also develop laterally from another variety of Cr-spinel seam (Fig. 5d). These seams tend to be discontinuous and very irregular, with depressions and culminations along strike (Figs. 3; Facies O; 5e). Harrisite-hosted (and chromitite) seams in the WLI may occur with vertical or sub-vertical orientations, so are not typically

stratiform like those reported in Unit 10 of the ELI (Hepworth *et al*., 2017). Cr-spinel seams in granular-textured peridotite can be locally cross-cut by upward-oriented harrisite apophyses (Fig. 4h), and by plagioclase veins. In the former case, the Cr-spinel seam is also deformed, following the broad amplitude of the underlying harrisites upper surface.

*Upper Ard Mheall Member (UAM)*

The UAM is situated at the top of the WLI at Ard Mheall and in the same structural position on the eastern side of the WLI, where it contains layers that dip steeply toward the adjacent CI (Fig. 2). In both localities, the UAM has a minimum thickness of ~30 m. The boundary between the AMP and UAM appears to occur over a 5–10 m thick interval, where mm–cm-sized intercumulus clinopyroxene oikocrysts are developed across the boundary. There is a change in outcrop colour from brown to grey, marking the transition into the UAM, caused by the increased abundance of intercumulus plagioclase and widespread plagioclase veining (Fig. 6a). The UAM is considerably less well-layered than the AMP peridotites and where layering does exist, it appears to be caused by the variation in abundance of intercumulus phases, particularly clinopyroxene (Fig. 6b). The dip of this layering is concordant to that measured in the AMP, dipping shallowly to moderately toward the east. Stratabound mm–cm scale plagioclase veining also defines a layering structure in the UAM, which dips shallowly to the west. Harrisite is present in the UAM but is less common than in the AMP, occurring as vertically-oriented sheets, cross-cutting magmatic layering in the host rock (Figs. 3; Facies P; 6c). Broadly, an increase in the abundance of intercumulus clinopyroxene is the most distinctive feature of the UAM (Fig.3; Facies Q), where this mineral comprises up to 40 vol.% of the wehrlitic peridotites (Fig. 6b, d). Abundant, vertically-oriented plagioclase veins locally cross-cut layering and are continuous at the outcrop-scale (Fig. 3; Facies R). Cr-spinel seams are not observed throughout the entire UAM. Exposures of the UAM to the east, in closer proximity to the CI, also contain abundant intercumulus clinopyroxene. Clinopyroxene veining is also present, in contrast to the Ard Mheall UAM exposures. Close to the boundary with the CI, irregularly shaped troctolite autoliths (<20 cm) occur in the UAM peridotites, a phenomenon not observed in the western UAM. Base-metal sulphides are unusually common in some of the eastern exposures of the UAM.

**The Transitional Member (TSM)**

The TSM is a ~50 m thick layered peridotite body that crops out between the AMP and the HBM (see Online Appendix 2 for structural position). The layering has an average dip of ~20º towards the NE. The contact between the AMP and TSM is marked by a gradational transition downwards from layered feldspathic and dunitic-peridotites (AMP) to a red-weathered wehrlitic-peridotite (TSM) over <5 m from the AMP. The TSM is well-layered like the AMP and contains both harrisite and granular-textured peridotite types (Fig. 7a). The range of thicknesses of layers is like those in the AMP, though harrisite layers are generally thinner (i.e., typical range of 0.2–2 m). Fine-scale layering in the granular-textured peridotites occurs at the cm-scale, with layers defined by variations in intercumulus material and/or the presence of Cr-spinel seams (Fig. 7b). The irregular tops and basal surfaces of harrisite layers occur in the TSM (Fig. 7c, d), though the amplitude of the apophyses observed is considerably less (<1 m) than in the AMP. Upward-oriented harrisite apophyses sometimes connect with overlying harrisite layers (Fig. 7d). Olivine within the harrisite are dominated by coarse-grained, bladed to branching shapes, often >10 cm in length (Fig. 7e). Harrisite bodies towards the top of the TSM are texturally heterogeneous, with clinopyroxene-poor layers containing large, irregular patches of hopper olivine, like morphologies in the AMP (Fig. 7f). The TSM cumulates have noticeably more intercumulus material (>20 vol.%) than those in the AMP, and although feldspathic-peridotites exist within the member, wehrlitic peridotites are dominant. Feldspathic peridotite is only found adjacent to Cr-spinel seams. The wehrlitic peridotites have a high proportion of rounded, cm-sized clinopyroxene oikocrysts (Fig. 7a). Cr-spinel seams in the TSM are less common than in the AMP, but display identical lithological relationships to those in the AMP (Fig. 7b). The Cr-spinel seams are extremely discontinuous, rarely extending laterally for more than a few metres, but they can change significantly in thickness and Cr-spinel concentration along strike, like they do in the AMP. Thick sheets (>10 cm) of gabbroic pegmatite are also common in the upper portion of the TSM (Fig. 7e).

**The Harris Bay Member (HBM)**

The HBM is approximately 120 m thick and comprises the structurally lowest exposed portion of the WLI (Fig. 2). The boundary with the overlying TSM is sharp, with a shallow dip <15° toward the N–

NE. In the lowermost part of the HBM, layering is horizontal. A schematic cross section through the WLI thus suggests onlap of the HBM by the overlying members (see Online Appendix 1). The contact of the HBM with the Western Granite is well-exposed at Harris Bay (Fig. 2), where the HBM clearly intrudes into the granite (see Greenwood, 1987 and Online Appendix 3). Discrete sheet-like lobes of the HBM protrude into the granite, defining an irregular and complex boundary zone (see Online Appendix 3).

The HBM is well-layered, but unlike the overlying members, consists of a high proportion of feldspathic cumulates (e.g., olivine-gabbro). There is a noticeable increase in the proportion of gabbroic cumulate towards the top of the member, such that the most olivine-rich lithologies crop out towards the base (at sea level). Layer thicknesses are relatively consistent throughout the member, with layers rarely exceeding 1 m, and on average are ~0.5 m thick. There is a broad decrease in the thickness that individual layers attain towards the top of the HBM, where layers are generally <0.5 m (Fig. 8a). Harrisite layers exhibit apophyses on their upper surfaces as reported for the overlying members, and large (up to 1 m long) olivine crystals are present in some outcrops (Fig. 8b). Individual harrisite layers also bifurcate (Fig. 8c). Granular-textured peridotite layers occur between harrisite layers that also display internal, finer-scale layering (1–2 cm thick). Cr-spinel seams are absent in the HBM, with layering is defined by relatively small changes in the intercumulus mineralogy. Foliation of tabular olivine crystals is present, most commonly surrounding harrisite layers where it may be very strong (e.g., Fig. 8d). The thickness of gabbroic layers varies between 0.1–0.5 m thick (Fig. 8e). The layers are typically intercalated with harrisite but can form successions of several metres comprising gabbro alone. The HBM gabbro is variable in texture and mineralogy at the outcrop scale, defining individual layers of melagabbro, gabbro, and leucogabbro (Fig. 8f). Melagabbros are particularly coarse-grained (3–5 mm) whereas leucogabbros tend to be fine-grained (~1 mm) (Fig. 8e, f).

## PETROGRAPHY

The term cumulus and intercumulus are used here as purely descriptive textural terms, the former describing primocryst/phenocryst phases (forming the cumulate framework), and the latter describing

the material occurring in the interstices of the cumulus phases, with no implied genetic or timing implications.

## Ard Mheall Member

### *Ard Mheall Peridotite*

#### *Harrisite*

The cumulus mineral phase in harrisite is ubiquitously olivine, which varies in abundance depending on the dominant crystal morphology. Highly-skeletal harrisites have a sub-equal proportion of cumulus and intercumulus material, while hopper olivine-dominated harrisite tends to have a lower intercumulus component (i.e., 10–30 vol.%). The morphology of olivine crystals in the AMP is variable but strongly dominated by hopper olivine crystal shapes (typical abundances >60 vol.%), with subordinate branching and skeletal forms. The crystal size of olivine in harrisite varies significantly in the AMP but has an approximate minimum crystal size (length) of 5 mm, including within lithologies containing both hopper and skeletal olivine. However, it is not uncommon for olivine crystals to greatly exceed 5 cm in length, particularly the highly skeletal and branching varieties. Hopper olivine crystals tend to be more restricted in size, with an average grain size of ~1 cm. Euhedral Cr-spinel crystals are found outside Cr-spinel seams in accessory proportions (<1 vol.%). Accessory Cr-spinel in harrisites is often coarser-grained than in the other peridotite types, up to 1 mm in diameter (Fig. 5f). Finer grained (<0.1 mm) Cr-spinel occurs as rare inclusions in olivine. No skeletal Cr-spinel crystals were observed. The intercumulus mineralogy of the AMP harrisites is dominated by plagioclase, with clinopyroxene present in typical proportions of <10 vol.%. This is consistent across the range of harrisite morphologies. However, approaching the UAM boundary, clinopyroxene content increases to >15 vol.%. Intercumulus plagioclase throughout the AMP comprises coarse-grained (1–3 cm) oikocrysts. Where present, subordinate intercumulus clinopyroxene occurs as similarly-sized oikocrysts. Plagioclase displays patchy optical zoning, particularly near Cr-spinel seams (Fig. 9a), and clinopyroxene can also be optically zoned, though this is rare (Fig. 9b). The olivine foliation observed at the outcrop-scale is also apparent in thin section,

controlled by elongate and branching olivine crystals (Fig. 9c). Trace amounts of secondary serpentine, chlorite, calcite, epidote and kaersutite occur in the interstices of the olivine framework.

*Granular-textured peridotite*

Granular-textured peridotites consist of ~70 vol.% rounded, euhedral (~0.5–3 mm) olivine crystals. A subordinate proportion of tabular and hopper olivine morphologies is present in most samples. A general observation is that the coarser-grained the peridotite, the greater the proportion of tabular and hopper olivine crystals. Euhedral Cr-spinel crystals occur in the interstitial areas and are also rarely present as inclusions in olivine. The intercumulus fraction typically comprises <15 vol.% of the granular-textured peridotites. For the most part, 1-5 mm plagioclase oikocrysts are dominant, though subordinate clinopyroxene oikocrysts of a similar size to the plagioclase also occur. Patchy compositional zoning is occasionally observed in both plagioclase and clinopyroxene oikocrysts (Fig. 9b). The volume proportion of intercumulus material can vary significantly between layers and can be as low as ~5 vol.%, where the rock is dunitic-peridotite. In such cases, the olivine triple-junctions have apparent dihedral angles approaching 120º (Fig. 9d). Such a texture is also common in granular-textured peridotite autoliths that occur within harrisite layers. The development of a foliation, carried by tabular olivine crystals, is common, especially adjacent to Cr-spinel seams (e.g., Fig. 9c). Trace amounts of secondary serpentine, chlorite, epidote, calcite and kaersutite–titano-pargasite amphibole occur in the interstices of the olivine framework.

*Porphyritic peridotite*

The granular-textured peridotite that contains olivine megacrysts has a similar mineralogy and texture to granular-textured peridotite, except for the cm-sized (0.75–7 cm) euhedral olivine crystals that predominantly occur concentrated into layers throughout (Fig. 10a), as described above. The finer-grained granular-textured peridotite hosting the olivine megacrysts is dunitic, with a proportion of intercumulus plagioclase <10 vol. %. The olivine crystals in the granular-textured peridotite are fine-grained (~1 mm) and euhedral, commonly exhibiting apparent dihedral angles at olivine three-grain-junctions that approach 120º (Fig. 10b). Unlike the fine-grained olivine crystals, the megacrysts

contain abundant crystallographically-constrained skeletal magnetite inclusions (Fig. 10a, b) (see also O'Driscoll *et al*. 2015). In the porphyritic peridotite, these inclusions only occur in the olivine megacrysts (i.e., they are absent in the fine-grained olivine in the granular-textured peridotite). However, it should be noted that magnetite inclusions are also observed in other harrisitic olivine crystals throughout the WLI (e.g., Fig. 10b, c).

*Cr-spinel seams*

Cr-spinel seams in the AMP exhibit a range of textures, but most are chain-textured, where the Cr-spinel crystals occur poikilitically enclosed in intercumulus plagioclase or clinopyroxene, distributed between and around the cumulus olivine crystal framework (Fig. 9c). In chain-textured seams, Cr-spinel is often observed within embayments in cumulus olivine crystals (Fig. 9a). Chromitite seams, where little to no cumulus olivine occurs within the seam, are less common. Cr-spinel crystal morphologies in seams vary slightly, depending on their host peridotite. For example, in granular-textured peridotite hosted Cr-spinel seams, Cr-spinel has a size range of 0.05–0.3 mm, while harrisite-hosted seams tend to be coarser-grained, with crystals up to ~0.8 mm in size, and an average size of 0.4 mm. Chromitite seams often host particularly coarse-grained (up to ~1.3 mm-sized) Cr-spinel crystals as well (Fig. 9e). Cr-spinel crystals in all seams are mostly euhedral. However, in some texturally distinct zones within composite chromitite seams, the crystal faces are notably lobate. It should also be noted that this texturally distinct zone in composite chromitite seams is not a uniform thickness on seam margins (see Fig. 18). Aggregates of Cr-spinel crystals occur in some samples, resulting in irregularly-shaped glomerocrysts. Within these, the constituent crystal boundaries can be resolved using reflected light microscopy. In chromitite seams, plagioclase is the only intercumulus phase (typically comprising ≤30 vol.% of the seam) and is typically severely altered. In some instances, chromitite seams appear to cross-cut olivine crystals, such that a given olivine crystal is in optical continuity on either side of the seam, so presumably predates the formation of the seam (Fig. 9e). This microtextural relationship has previously been reported for Cr-spinel seams in the ELI Unit 12 peridotite by O'Driscoll *et al*. (2010). Well-rounded inclusions are very common in coarser-grained Cr-spinel crystals in harrisite-hosted and chromitite seams. The inclusions define internal

zones within Cr-spinel crystals or can be concentrated in crystal cores (see Fig. 9e). The inclusions have a variety of compositions, including kaersutite, plagioclase, clinopyroxene, and base-metal sulphide (in one of the latter instances including a Pt-arsenide grain). Amphibole (kaersutite) is the most common type of inclusion. Ilmenite exsolution occurs in Cr-spinel crystals in the WLI but is much less a feature of Cr-spinel in seams, than accessory Cr-spinel in the various types of peridotite.

Base-metal sulphides, alloys and native metals are present in the AMP cumulates, especially in close (mm–cm) proximity to Cr-spinel seams. Chromitite seams have a higher abundance of sulphides than chain-textured Cr-spinel seams. Common sulphide phases include chalcopyrite ($CuFeS_2$), pentlandite (Fe, $Ni_9S_8$), chalcocite ($Cu_2S$), heazlewoodite ($Ni_3S_2$), with less common bornite ($Cu_5FeS_4$), pyrrhotite (FeS) and native copper. The sulphides typically attached to the edges of Cr-spinel crystals. Where base-metal sulphides are in contact with Cr-spinel, the latter displays alteration to sieve-textured ferrian chromite (Fig. 9f). Platinum-group minerals (PGM; e.g., sperrylite) with upper grainsize limits of ~1 µm, can also be observed, closely associated with base-metal sulphides.

*Upper Ard Mheall Member (UAM)*

The texture of the UAM peridotites resembles the granular-textured peridotites in the AMP, but with key mineralogical variations. Olivine is the dominant cumulus phase, with sparse cumulus Cr-spinel (also occurs as rare inclusions in olivine). Olivine crystals are equant (typically <3 mm), with less common tabular and hopper crystal morphologies. Rare harrisite layers are dominated by cm-sized hopper olivine crystal morphologies, as observed in the AMP. The volume proportion of intercumulus material in the granular-textured peridotite is higher than in the AMP (i.e., 15–25 vol.%). The intercumulus mineralogy is dominated by plagioclase but clinopyroxene is more abundant (15–40 vol.%) than in the AMP. Intercumulus plagioclase oikocrysts are coarse-grained, typically >5 mm, with clinopyroxene oikocrysts typically in the size range 0.5–1 cm, occasionally up to ~3 cm. While plagioclase oikocrysts tend to be equant, clinopyroxene-oikocrysts are both equant and elongate. Patchy compositional zoning is present in both intercumulus phases. A foliation, defined by olivine crystals, is locally developed.

**The Transitional Member**

The cumulus mineralogy of harrisites in the TSM comprises coarse-grained, skeletal and bladed olivine crystals, up to several cm in size. Rare euhedral Cr-spinel (<0.2 mm) crystals are present between olivine crystals. Inclusions (<0.1 mm) of Cr-spinel are also found rarely within olivine. The intercumulus volume proportion constitutes >30 vol.% of TSM harrisites and as much as 40–50 vol.%. The intercumulus proportion is made of coarse-grained plagioclase and clinopyroxene oikocrysts, typically as rounded crystal forms (0.5–2 cm in diameter). Plagioclase is slightly more abundant than clinopyroxene, typically making up 50–60 vol.% of the intercumulus fraction. Patchy compositional zoning is present in both intercumulus phases (Fig. 11a, b).

Olivine in wehrlitic-peridotites has a very similar texture to that observed in the AMP granular-textured peridotites. Rounded–equant olivine crystals (0.5–3 mm), with subordinate hopper crystals, are dominant. Olivine crystals are smaller in size (≤0.5 mm) near or within some Cr-spinel seams. Cumulus clinopyroxene crystals also occur rarely in the wehrlitic-peridotites, displaying weakly developed exsolution lamellae (Fig. 11c). The proportion of intercumulus material is >20 vol.%, with plagioclase and clinopyroxene the dominant phases. Plagioclase is more abundant than clinopyroxene (approximate ratio of 60:40). Both occur as 0.5–2 cm rounded oikocrysts, with some more irregular clinopyroxene oikocrysts present. Both intercumulus phases display patchy compositional zoning, more commonly in the clinopyroxene (Fig. 11b).

Feldspathic peridotite in the TSM is dominated by intercumulus plagioclase, comprising >50 vol.% of the rock. This lithology only occurs near Cr-spinel seams in the TSM (Fig. 11d). Olivine is the only cumulus mineral, with a tendency to form elongate, skeletal forms <1 cm in length (Fig. 11a). Fine-grained Cr-spinel is present outside the seams, distributed around olivine crystals. Plagioclase oikocrysts are rounded–elongate, and 1–5 mm in diameter, and display patchy optical zoning (Fig. 11a). Intercumulus clinopyroxene is rare (≤5 vol.%) and has a similar size range of sizes to plagioclase but exhibits more irregular–rounded crystal shapes. Secondary serpentine, chlorite, epidote and particularly kaersutite are present in greater quantities than in the AMP (i.e., 1–3 vol.%) in all peridotite types in the TSM.

Cr-spinel seams are rare in the TSM but share similar characteristics to those found elsewhere in the WLI, except that clinopyroxene oikocrysts are more abundant in the seams than plagioclase. Cr-

spinel seams in the TSM have higher proportions of intercumulus material, notably where clinopyroxene is the primary intercumulus phase (Fig. 11e), and plagioclase is almost absent (<5 vol.%). Olivine crystals poikilitically enclosed in intercumulus clinopyroxene are often significantly smaller and more rounded than olivines outside of the oikocrysts (Fig. 11f) and can define relict zones within the oikocryst where the olivine crystals remain in optical continuity with each other (Fig. 11f). Cr-spinel crystals in seams in the TSM are largely subhedral–anhedral and are typically 0.05–0.4 mm in diameter. There are larger numbers of fine-grained crystals (~ 0.05 mm), particularly where poikilitically enclosed by clinopyroxene. Irregularly-shaped aggregates of Cr-spinel are common.

Base-metal sulphide minerals are more common in the TSM than in the AMP (Fig. 11g), and comprise chalcopyrite, pentlandite and abundant pyrrhotite. The pentlandite has a lower Ni:Fe ratio than pentlandite in the AMP, with noticeably lower Ni contents (see Online Appendix 5). Sulphides are particularly abundant in feldspathic peridotites but are also common in harrisites and wehrlitic-peridotites (Fig. 11g). The sulphides are often attached to or close to Cr-spinel crystals. As before, alteration of the Cr-spinel where in close proximity to base-metal sulphide is ubiquitous (Fig. 11g).

**The Harris Bay Member**

*Peridotite*

The cumulus mineralogy of harrisite in the HBM comprises olivine and plagioclase. Olivine typically occurs as coarse-grained (up to ~1 m long, in some cases, more commonly ~50 cm), skeletal and bladed crystals that do not appear to show any preferred orientation (Fig. 12a). Plagioclase also occurs as a cumulus phase. Cumulus plagioclase crystals are coarse-grained (1–5 mm), euhedral–subhedral tabular crystals that commonly display optical zonation, including oscillatory zoning (Fig. 12b). Intercumulus plagioclase is abundant in harrisite occurring as anhedral oikocrysts, ~1–5 mm in diameter, though some larger (up to 10 mm) oikocrysts are also present. Optical zoning is present, though less commonly than in cumulus plagioclase, and is not observed as frequently as in the AMP and TSM. Intercumulus clinopyroxene comprises ~30–40 vol.% of the total intercumulus fraction, with very coarse ~5–20 mm, anhedral oikocrysts that locally display strong, patchy zoning (e.g., Fig. 12c). Disseminated Cr-spinel crystals (<0.2 mm grainsize) occur throughout the harrisites, in the

interstices of the silicate framework. Phlogopite and calcic-amphibole are also present in quantities ranging between 1–3 vol.%, as well as occasional serpentine, chlorite, calcite and sparse apatite. Where present, the amphibole can also exhibit complex optical zoning (Fig. 12d).

Granular-textured peridotites in the HBM have mineral modes akin to those recorded in harrisite, though olivine is not as coarse-grained or skeletal (typically <5 mm), and the overall grainsize of plagioclase is also smaller (i.e., <2 mm). Olivine is ubiquitously cumulus, while plagioclase is intercumulus and rarely cumulus. Granular-textured peridotites in the HBM are often wehrlitic. Plagioclase (cumulus and intercumulus) and intercumulus clinopyroxene exhibit compositional zoning. Cr-spinel and magnetite are present as <0.2 mm euhedral–subhedral crystals, typically found in the interstices of the olivine framework but also as rare inclusions in olivine. Slightly higher than trace abundances (typically 1–3 vol.%) of secondary phlogopite, amphibole, serpentine, chlorite, calcite and apatite are also present.

*Gabbros*

The olivine-gabbros in the HBM contain olivine, plagioclase and clinopyroxene. There is significant variation in the textures between the melagabbros, olivine gabbros, and leucogabbros, although the textural configuration of olivine, plagioclase, and clinopyroxene is broadly the same in all gabbro types. In the melagabbros, olivine makes up ≤15 vol.% of the mineralogy, and exhibits distinctly anhedral, morphologies (0.25–3 mm in length). Olivine is often severely altered to serpentine and fine-grained iddingsite-chlorite mixtures. Plagioclase is abundant (>60 vol.%) and exhibits subhedral crystal shapes and crystal sizes ranging from 0.5–3 mm. Compositional zonation is ubiquitous in plagioclase, with oscillatory zoning rarely observed. Clinopyroxene is also abundant, as cumulus crystals ~2–3 mm in diameter and mm to cm-sized oikocrysts. Both intercumulus and cumulus pyroxenes are commonly zoned, with distinctly ‘spongy’ rims present on some cumulus crystals. The olivine-gabbro is mineralogically like the melagabbro, but exhibits a finer-grained texture, with olivine (<1 mm), plagioclase (<2 mm) and clinopyroxene (<3 mm) crystals all consistently smaller. Olivine and clinopyroxene are less abundant than in melagabbro, <10 vol.%, and <25 vol.%, respectively. Optical zoning is present in both plagioclase and clinopyroxene as in the melagabbros.

Spinel (mostly magnetite) in the gabbros exhibits highly skeletal morphologies, forming elongated needles and blades (Fig. 12f). The leucogabbros are finer-grained than the other gabbro types with olivine, plagioclase, and clinopyroxene having grainsizes ≤1 mm. Plagioclase is ubiquitously altered, exhibiting a 'dusty' appearance as result of saussuritization. Olivine comprises <5 vol.% in the leucogabbros and is typically highly altered to iddingsite-chlorite mixtures. Clinopyroxene is cumulus in appearance, less altered than plagioclase and typically <1 mm in diameter. Cumulus crystals, and rarer intercumulus crystals, of perthitic alkali-feldspar (orthoclase) are present (Fig. 12e). Pockets of quartz are also found within the leucogabbros. Apatite is also observed at higher than trace amounts within all gabbros. Base metal sulphides (e.g., chalcopyrite and pyrrhotite) are observed in close spatial association with spinel in all three gabbro types.

## QUANTITATIVE TEXTURAL ANALYSIS

### Crystal Size Distribution (CSD) Analysis

*Method*

Crystal Size Distribution (CSD) analysis provides a means to study the kinematics of crystal nucleation and growth in rocks, independent of experimental or thermodynamic methods (Cashman & Marsh, 1988; Marsh, 1998; Boorman *et al*., 2004). Simple crystallisation in open (steady-state)- or closed (batch)- magma system end-members should produce a straight (log-linear) CSD profile that reflects increasing nucleation of crystals as the magma solidifies (Marsh, 1998). Deviation from an ideal log-linear profile (e.g., kinking or curvature) has been attributed to a variety of magmatic processes such as crystal accumulation or removal (Marsh, 1998), coexistence of more than one crystal population (i.e., in crystal cargos or slurries; Higgins, 1994; Marsh, 1998), and postcumulus processes such as crystal annealing, coarsening (e.g., Ostwald ripening) or physical compaction of crystal mushes (Higgins, 2002b; Boorman *et al*., 2004). Recent numerical modelling of crystal nucleation and the resultant CSDs by Špillar & Dolejš (2014) suggests that log-linear to concave-down profiles, the latter often proposed to be caused by crystal coarsening, can be formed by variable growth and nucleation rates. Concave-up CSD profiles, often attributed to be the result of mixing populations or crystal accumulation, can be produced by heterogeneous nucleation (Špillar & Dolejš,

2015a). CSD parameters such as characteristic length and intercept have been shown to share a relationship irrespective of the volume percentage of the mineral phase analysed (Higgins, 2002a). The consideration of closure in CSDs can reveal important information about the quality of CSD calculations and the degrees of freedom available to interpret CSD data; i.e., samples which are close to or on the closure limit cannot have undergone processes that significantly alter the volumetric phase proportions between samples, such as textural coarsening (Higgins, 2002a). Conversely, if a population does not come close to its closure limits, more freedom to interpret changes in the volumetric abundance exists (Higgins, 2002a).

The CSDs reported in this study were determined from polished thin-sections and calculated following the approach of Higgins (2000; using *CSDCorrections version 1.4*). Cr-spinel and olivine crystals were manually digitised using reflected and cross-polarised light, respectively. Reflected light images were used for Cr-spinel to avoid misidentification of annealed opaque crystals in transmitted light (see O'Driscoll *et al*., 2010; Vukmanovic *et al*., 2013). The digitised images were then processed using *ImageJ* image analysis software (Schneider *et al.*, 2012) to calculate the input parameters for *CSDCorrections*. For Cr-spinel in this study, we employed 'feret-length', the length of a square with an area equal to the analysed crystal, as our main size parameter, following O'Driscoll *et al*. (2010). No alignment of Cr-spinel is observed in any of the samples (i.e., a 'massive' fabric setting was used). An aspect ratio of 1:1:1 and roundness factor of 0.5 were input into *CSDCorrections*. In total, 37 CSDs were produced from various WLI Cr-spinel seams (see Fig. 13), covering the range of different Cr-spinel seam textural types described above. Data were produced for a minimum of 500 crystals in each sample, where possible, to produce a statistically robust representation of each seam (Mock & Jerram, 2005). As the smallest crystals are easily distinguishable using reflected light, the lower crystal size limit is taken as the true lower limit of the sample. The quantification of crystallinity used in some CSD derivative plots was calculated using *ImageJ*, with the R-value calculated within *CSDCorrections version 1.4* (see. Jerram *et al*., 1996; Higgins, 2006).

*Results*

The CSD plots are presented in Figure 13, with the raw CSD output data provided in Online Appendix 3. The different groupings of Cr-spinel seams established based on petrographic observations are generally not distinguishable in the CSD dataset. All CSDs display a log-linear profile at larger size portions, with deviation in some profiles at smaller size fractions, and reveal a range of slope values from -38.0 to -6.4 $mm^{-1}$. Granular-textured and boundary-type Cr-spinel seams (Figs., 13a, b) have very similar slope values (-37.8 to 17.1 $mm^{-1}$). Harrisite-hosted Cr-spinel seams have shallow CSD slopes (Fig. 15c) but can be delineated based on the dominant olivine morphology of the host. Specifically, skeletal olivine-dominated harrisite-hosted Cr-spinel seams have slope values between -38.0 and -32.0 $mm^{-1}$, whereas hopper olivine-dominated harrisite-hosted Cr-spinel have shallower slope values between -26.6 to -11.8 $mm^{-1}$. Chromitite seams have the shallowest slopes (i.e., $\leq$ -14 $mm^{-1}$; Fig. 13d). Composite chromitite seams display variable CSD profiles across the different textural zones, where coarser-grained zones have distinctly shallower slopes than the central finer-grained zone (Fig. 13e). Downturns at the smallest size fractions are observed in CSDs from Cr-spinel seam types, except for harrisite-hosted seams, in which the downturn is absent in skeletal olivine-dominated harrisite-hosted seams, but present in hopper olivine-dominated harrisite-hosted seams (Fig. 13c). Foliated peridotite-hosted seams have a distinctive CSD profile similar to those reported for the Unit 10 peridotite (Hepworth *et al*., 2017). They display a log-linear profile at the largest size portions but have a broadly 'humped' profile at the small size fraction. The TSM Cr-spinel seam CSD profiles show similar patterns to those in the AMP (Fig. 13f), with log-linear profiles at larger size portions, and some downturns at smaller size fractions. The data from the TSM and AMP show a comparatively restricted range of slope values between -16.3 and -24.1 $mm^{-1}$, which mainly represent the large size fractions of the CSDs. The TSM CSDs exhibit slightly higher population densities and complex profile shapes at the smaller size fractions, than the AMP (Fig. 13f)

CSD derivative diagrams can be found in Online Appendix 4, with selected plots illustrated in Figure 14. A characteristic length (CL) versus volumetric proportion plot distinguishes some of the Cr-spinel seam as outlined previously (Fig. 14a), such as the chromitite seam group, which plot with distinctly higher CL and a relatively high-volume proportion of Cr-spinel, and a harrisitic peridotite-hosted Cr-spinel seam outlier. The other seam groups cluster closely together with low CL and

volumetric abundance. The volume percentage of Cr-spinel (calculated in *ImageJ*) was plotted against the crystallinity of each sample (vol.% olivine – assumed to be pre-existing; see Hepworth *et al*., 2017), with a good negative correlation ($R^2 = 0.77$; Fig. 14b) suggesting a correlation between the availability of space in the crystal framework and Cr-spinel abundance. Most samples plot well below the closure limits defined by 100% volumetric abundance. Spatial Distribution parameters, such as R-value (which quantifies the degree of clustering versus ordering of a grain population; see Jerram *et al*., 1996; 2003; Špillar & Dolejš, 2014; 2015a), plotted against the vol. % Cr-spinel reveal a strong positive correlation ($R^2 = 0.83$; Fig. 14c). Furthermore, an increase in crystallinity results in a moderate negative correlation with R-value (Fig. 14d), also highlighting a relationship between clustering, Cr-spinel abundance, and available space within the crystal mush (i.e., more Cr-spinel forms where more space is available).

## MINERAL CHEMISTRY

### Methods

Mineral chemical data were obtained using a JEOL JXA-8900RL electron microprobe at the Department of Geochemistry, Geowissenschaftliches Zentrum der Universität Göttingen (GZG) in 2014 and 2015. The Cr-spinel compositions were obtained using an acceleration voltage of 20 kV with a beam current of ~20 nA and a typical beam diameter of 1 μm. Cr-spinel count times on peak and background for Mg, Al, Cr, Fe and Si were 15 s and 5 s, respectively, and for V, Ti, Mn, Ni and Zn were 30 s and 15 s, respectively. Plagioclase compositions were obtained with an acceleration voltage of 15 kV with a beam current of ~15 nA and a typical beam diameter of 20 μm. Plagioclase count times on peak and background for Si, Na, K, Ca, Fe and Al were 15 s and 5 s, respectively, and for Ba and Sr, were 30 s and 15 s, respectively. Clinopyroxene compositions were obtained with an acceleration voltage of 15 kV, a beam current of 15 nA, and a typical beam diameter of 15 μm. Clinopyroxene count times on peak and background for Si, Na, K, Ti, Fe, Al, Mg, Ca and Mn were 15 s and 5 s, respectively, and for Cr and Ni, were 30 s and 15 s, respectively. The ferric iron content of Cr-spinel in this study was calculated following Droop (1987), assuming the spinel composition to be

stoichiometric. Thus, small variations in ferric iron content of Cr-spinel should be treated with caution (Quintiliani *et al*., 2006; O'Driscoll *et al*., 2010).

Cr-spinel compositions in eighteen different seams from the AMP (16) and TSM (2) were measured in two vertical traverses across each seam, each traverse consisting of ~20 points and extending into the host peridotite above and below. In the HBM and UAM where no Cr-spinel seams occur, disseminated Cr-spinel crystals were analysed. Plagioclase and clinopyroxene mineral chemical data from the AMP, UAM, TSM, and HBM were obtained from selected samples where optically zoned and unzoned crystals were observed, to evaluate the maximum range of compositions of these phases present in the WLI. A minimum of one rim and one core was analysed per zoned crystal in each case, with unzoned crystals analysed as well. Previously published mineral chemical analyses of plagioclase and clinopyroxene from the AMP (Worrell, 2002) have been plotted with the new data, for comparison.

**Results**

The full mineral chemical dataset discussed below can be accessed in Online Appendix 5.

*Cr-spinel*

The composition of Cr-spinel in the AMP is highly variable, with some of the most aluminous Cr-spinel yet documented from the RLS (up to 39 wt.% $Al_2O_3$; Cr# [$Cr^{3+}/(Cr^{3+}/Al^{3+})$] 0.29). Accessory Cr-spinel disseminated throughout the AMP peridotites typically has higher Cr# and lower Mg# [$Mg^{2+}/(Mg^{2+}/Fe^{2+})$] values than Cr-spinel that occurs within seams, the latter yielding higher $Al_2O_3$ and MgO values (Figs. 15a). There is significant overlap in the Cr-spinel chemistry of boundary and granular-textured peridotite-hosted Cr-spinel seams. However, the chromitite seams have distinctively low Cr# and high Mg# values (Fig. 15a). Some compositional variation is also present in harrisite-hosted Cr-spinel seams, where Cr-spinel has consistently higher $Fe_2O_3$ contents (~17.7 wt. %; Fig. 16) and elevated $TiO_2$ concentrations (typically ~3 wt. %, and as high at 7 wt. %; Fig. 15b). It is noteworthy that the Cr content of the Cr-spinel does not vary substantially between the different seam types (overall range is 34 to 38 wt.%). Compositional traverses across Cr-spinel seams of all types

reveals consistent variations in Cr# (and Mg#), $Fe_2O_3$ and $TiO_2$. Specifically, Cr# and Mg# typically increase towards the centres of Cr-spinel seams, while $Fe_2O_3$ increases towards seam margins (e.g., Sample AM6; Fig. 20). In most seams, $TiO_2$ content is constant throughout, except at the outer margins where it increases sharply (e.g., Sample AM18; Fig. 17). Chromitite seams display constant Cr-spinel compositions within the seam, but these usually change dramatically above and below the seam (AM18; Fig. 17). In one relatively thick, texturally composite chromitite seam (AM18; Fig. 20), $TiO_2$ concentration remains constant, except at the internal textural boundary, across which a step-change of ~0.5 wt.% $TiO_2$ occurs (AM18; Fig 17). Compositional zoning of coarse-grained Cr-spinel crystals occurs locally in some chromitite seams, e.g., in sample AM18 (Fig. 18) which exhibits an increase in $TiO_2$ and $Fe_2O_3$ towards the rim of the crystal.

The composition of Cr-spinel from the UAM shows modest differences to that in the AMP, with slightly elevated Cr# and lower Mg# (Fig. 18a). The ferric iron content of UAM Cr-spinel is higher, up to 19 wt. % (Fig. 16), whilst $TiO_2$ is similar to that in the AMP.

Cr-spinel in the TSM exhibits distinctly lower Mg# and higher Cr# values than the AMP, with disseminated Cr-spinel displaying some of the lowest Mg# values in the WLI (Figs. 15a, 16). The ferric iron content of Cr-spinel is considerably higher in the TSM, with $Fe_2O_3$ contents ~28 wt. %, and $TiO_2$ also consistently relatively high (~3 wt. %; Fig. 15b). Vertical traverses through Cr-spinel seams reveal similar trends to those observed in the AMP, with a broadly symmetrical pattern through the Cr-spinel seam with increasing $Fe_2O_3$ and Cr# towards the edges of and outside seams. However, $TiO_2$ contents remain comparatively constant through the seam traverse, increasing sharply into the overlying peridotite (TM1; Fig. 17). The $TiO_2$ content of all Cr-spinel in the TSM traverse is elevated compared to AMP traverses (~4 wt.%). Another traverse across a diffuse Cr-spinel seam in the TSM shows a broadly similar pattern to TM1 (Fig. 17) with an overall enrichment in $TiO_2$, but a notable sharp increase as the boundary into wehrlitic peridotite is crossed. (see Online Appendix 5).

Cr-spinel in the HBM is disseminated throughout both peridotites and gabbros and no seams are present. The Cr-spinels generally have high Cr# and very low Mg# (Fig. 15), and exhibit significant Fe-enrichment, particularly $Fe_2O_3$, with values as high as 66% wt. %. The HBM Cr-spinel is poor in $Al_2O_3$ overall, they are best classified as ferrian-chromite–Cr-magnetite (Fig. 16). Like the

disseminated Cr-spinel in the other members of the WLI, $TiO_2$ contents are relatively elevated (>3 wt. %; Fig. 15b).

*Clinopyroxene*

Clinopyroxene in the AMP is predominantly diopside, with a limited Mg# range (84–90). $Cr_2O_3$ contents are typically ~1 wt. %, with $TiO_2$ consistently >1 wt.% (Figs. 19a, b). There is no correlation between $Cr_2O_3$ or $TiO_2$ with Mg#; instead a largely scattered array is observed that corresponds well to the data reported by Worrell (2002). Clinopyroxene oikocrysts in the UAM ubiquitously exhibit chemical zoning. Weak normal zoning with respect to $Cr_2O_3$ is observed, with rims containing lower values. $TiO_2$ content also varies significantly between the cores and rims of UAM oikocrysts, with the cores characterised by lower (<0.5 wt.%) contents, whilst the rims have similar values (~1 wt.%) to the unzoned clinopyroxene of the AMP (Fig. 19b).

Clinopyroxene in the TSM is also diopside, with lower Mg# (~83) than in the AMP. Normal zoning is rarely apparent, but where present is characterised by the variation of $TiO_2$ contents from cores to rims of ~0.5 to ~1 wt. %, respectively, up to a maximum rim value of ~1.8 wt. % (Fig. 19b). Clinopyroxene in the TSM is unzoned with respect to $Cr_2O_3$ content and reveals a scattered array of values between 0.72–1.19 wt.% (Fig. 19a). There is a weak positive correlation between $Cr_2O_3$ and Mg#, and a weak negative correlation with $TiO_2$ and Mg# (Fig. 19b).

Clinopyroxene in the HBM has a similar composition to that of the overlying members, but is most like clinopyroxene of the TSM, with relatively low Mg# and with similar trends in $TiO_2$ and $Cr_2O_3$ to the TSM (Figs. 19a, b). Clinopyroxene crystals in the HBM are abundantly and strongly normally-zoned with variation observed in both $Cr_2O_3$ and $TiO_2$ contents. The highest $TiO_2$ and lowest $Cr_2O_3$ contents are measured in the rims. Mg# and $TiO_2$ are negatively correlated in HBM clinopyroxene, as also observed in the TSM (Fig. 19b).

*Plagioclase*

Plagioclase oikocrysts from the UAM consistently have a slightly lower An-content (~81 mol. %) and higher FeO contents (up to ~0.5 wt. %) than those in the AMP (Worrell, 2002; Fig. 19c). Plagioclase

zoning is present, with lower An contents (~70 mol.%) at the rims (Fig. 19c).

Plagioclase in the TSM is typically normally zoned, though oscillatory zoning and reverse zoning are also observed (Fig. 19c). Plagioclase cores have average An-contents ~84 ±2 mol. %, as in the AMP, while the rims are less calcic (~66 ±3 mol.%). The FeO content of plagioclase in the TSM is elevated (typically >0.4 wt.%) compared to plagioclase in the AMP (Worrell, 2002; Fig. 19c).

Plagioclase oikocrysts in one harrisite sample in the HBM are normally and oscillatory zoned. The An-content of cores is comparable to the other WLI members, with high anorthite values between 72–86 mol.%. Normally-zoned rims have among the lowest An-contents (~56 mol.%) in the WLI. The FeO content of all plagioclase is elevated (>0.3 wt.%) in comparison to the AMP, overlapping with the UAM and TSM.

## DISCUSSION

### The origin of olivine cumulates in the Western Layered Intrusion

*Sill emplacement of harrisite*

Harrisite is a type example of 'crescumulate', as defined by Wager *et al* (1960). These authors envisaged the skeletal, harrisitic olivine as having grown upwards from the magma chamber floor, so this texture also represents a key example of *in situ* crystallisation in layered intrusions. The presence of numerous harrisite layers throughout the WLI has been cited as evidence for multiple replenishment events in the WLI, with each harrisite taken as representative of a discrete influx of picritic magma (Wadsworth, 1961; O'Driscoll *et al*., 2007a). These studies considered magma replenishment to have occurred at the magma chamber floor, where the undercooled picrite crystallised harrisitic olivine on the substrate. The replenishment events were thought to have been separated by periods of crystal settling and density current (slurries) deposition, to produce the granular-textured peridotites (Worrell, 2002; O'Driscoll *et al*., 2007a). Donaldson (1981) pointed out that harrisite layers in the WLI locally terminate laterally and bifurcate and suggested that at least some harrisite could therefore form within the crystal mush from expelled intercumulus liquid. A similar idea was recently invoked for the Unit 10 peridotite of the ELI, where harrisite bodies with irregular contacts (e.g., apophyses on their upper surfaces) were highlighted as evidence for an

intrusive origin (Hepworth *et al*., 2017). The latter authors suggested that harrisite bodies in Unit 10 represent apparently randomly-distributed, sill-like intrusions of picrite. Harrisite layers from the WLI bear striking similarities to those in the Unit 10 peridotite, but with some important differences. In the HBM, the intercalation of harrisite bodies comprising single or multiple layers (see Greenwood, 1987 and Online Appendix 3) into the Western Granite, strongly suggests sill emplacement of harrisite into its country rocks. The outcrop-scale features described by Donaldson (1982) and Hepworth *et al.* (2017) are observed ubiquitously in the WLI harrisite layers, including bifurcation (Fig. 4a), and upward-oriented apophyses (Fig. 4c), as well as rarer undercutting apophyses (Fig. 4d). Harrisite apophyses in the WLI protrude into the overlying cumulate as dome-like structures, <1 m vertically, but over several metres laterally. Upward-oriented apophyses emanating from some WLI harrisite bodies can be several metres high and over a metre wide, forming 'harrisite columns' which cross-cut and deflect the layering in the host granular-textured peridotite (Fig. 4e). The texture of the harrisite, including olivine morphology and grainsize, the proportion of intercumulus material and overall mineral mode is unchanged from the layer to the apophyses (including the downward oriented apophyses), so we interpret the apophyses as primary magmatic features, and not the result of late-stage filter-pressing of intercumulus liquid (Donaldson, 1982). Collectively, these observations point strongly to an intrusive origin, as sill-like bodies, for most if not all the harrisites in the WLI.

The distribution of harrisite layers through the WLI appears random, with very little lateral correlation between layers (see Online Appendix 1). The source of most magma is postulated to be the LLF to the east of the WLI (Fig. 1), in agreement with Emeleus *et al*. (1996). However, the observation that harrisite bodies form vertically-oriented domes and column-like structures, deforming the layering in the cumulate that they intrude (Figs. 4e), suggests that at least some harrisite could be linked to sub-vertically oriented syn-magmatic conduits within the WLI crystal mush (see Fig. 7d). Late-stage peridotite plugs, representing pipe-like magmatic conduits, are common in the RLS, cross-cutting the stratigraphy of the layered rocks, and are also well known to occur as satellites outside the margins of the RLS (Holness *et al*., 2012), suggesting that is not an unusual mode of magma emplacement on Rum.

Hepworth *et al.* (2017) proposed that hot tearing (and shearing) of a crystal mush under lateral shear stress formed ideal pathways for magma to migrate into the crystal mush of the Unit 10 peridotite in the ELI. Similar mechanisms have been invoked to explain melt concentrations within spatially restricted lenses or pods in natural silicate crystal mushes (Phillpotts *et al.,* 1996; Geshi, 2001; Humphreys & Holness, 2010; Namur *et al*., 2013). There are strong parallels between the field and petrographic observations in the WLI and those in the Unit 10 peridotite, including the evidence for deformation of layering (Fig. 4i), foliations (Fig. 4g), and the lithological relationships of harrisite. The entire cumulate pile also dips towards the feeder zone ~15º. The dip increases (>60º) with proximity to the feeder fault, attesting to a similar lateral-dominated stress regime to the Unit 10 peridotite, suggesting a similar mode of sill emplacement in the WLI.

*Petrogenesis of harrisite and the thermal history of the WLI crystal mush*

The WLI contains an extreme variety of olivine crystal sizes and morphologies for a comparatively small peridotite body, encompassing a range from mm-sized granular-textured (polygonal) olivine crystals to m-sized branching and skeletal varieties (Donaldson, 1974; O'Driscoll *et al*. 2007a). The conditions necessary to form the complex, skeletal and branching olivine crystals that comprise harrisite were studied experimentally by Donaldson (1974) where he proposed that harrisite represents picritic magma that underwent significant degrees of undercooling. The cause of this undercooling in the WLI is still uncertain. Donaldson (1974) speculated that volatile or water exsolution might have been responsible for lowering the liquidus of the parental magma, however, given the absence of primary hydrous phases (or fluid and melt inclusions), the role of volatiles is unlikely to be significant. It might also be expected that harrisites contain more hydrous phases than granular-textured peridotites, which is not observed. O'Driscoll *et al.* (2007a) suggested the temperature difference between the replenishing picrite and resident magma in the chamber was sufficient to cause undercooling, while Hepworth *et al*. (2017) suggested that the Unit 10 harrisites formed from intrusive picrites that undercooled against the mostly solid crystal mush. Given the evidence presented here for an intrusive origin for harrisite in the WLI, the latter model may also be appropriate here. Harrisite in the WLI typically occurs within granular-textured peridotite (Fig. 4c). The field

observations presented here show that no harrisite is visibly cross-cut by granular-textured peridotite. If the granular-textured peridotites represent an early (pre-harrisite) episode of crystallisation, they must have cooled significantly for the requisite undercooling to occur, so that picrite intrusions could form harrisites. The field relations reported here show that the rate of magma replenishment into the WLI was not necessarily constant and may have been linked to movements on the LLF (Volker & Upton, 1990; Emeleus *et al*., 1996). During periods of relative quiescence, cooling of the crystal pile likely occurred, such that a temperature gradient existed between new picrite replenishments and their host. The sharp unconformable boundary between the HBM and the TSM might indicate a particularly significant time-gap, given the clear change to the parental magma to each.

Different members of the WLI are characterised by different olivine morphologies. The most complex (branching and skeletal) olivine morphologies occur in the lower TSM and HBM, while the AMP is dominated by hopper and coarse-grained granular morphologies. From experimental work carried out on olivine morphology (e.g., Donaldson, 1974; Lofgren & Donaldson, 1975; Donaldson, 1976; Faure *et al*., 2003), it seems reasonable that the variation in olivine morphology both between individual peridotite-harrisite layers and between different members might have been caused by variable degrees of undercooling. A caveat to this is raised by the work of Means & Park (1994), who showed that given sufficient time at high sub-solidus temperatures, complex crystal shapes (i.e., high surface area to volume ratio) may revert to more polyhedral shapes. This is driven by textural equilibration, where the high interfacial energy in skeletal crystals is thermodynamically unstable and reduces to more stable, low surface area forms. Assuming no late stage mechanical remobilisation or disruption, it might be expected that the originally skeletal, now polyhedral crystals would remain in optical continuity in thin section. This is rarely observed and, where it is observed, can be explained by the cut effect of complex skeletal crystal forms. This is not to say that textural equilibration did not occur locally, but we interpret the intrusion-scale morphological variation of olivine in the WLI, from the HBM and TSM to the AMP, as a primary magmatic feature given how rapidly harrisite has been shown to crystallise under these conditions (see O'Driscoll *et al*., 2007a).

The laboratory experiments of Donaldson (1976) on olivine morphology provide a useful gauge for crystallisation conditions in the WLI. It is speculated that the earliest episode of intrusion would

have been characterised by the highest thermal gradient into the country rocks, but presumably ΔT°C did not exceed 250°C, or the replenishing magmas would have quenched, with a liquidus temperature between 1360 and 1175°C (Donaldson, 1976). This would mean that the country rocks were already hot (>700°C) when the WLI began to form, which is supported by observed radial cooling joints around harrisite sills in the Western Granite (see Online Appendix 3). The HBM, containing the coarse-grained bladed–skeletal olivine crystals required the steepest thermal gradient (and a temperature difference ~200 ΔT°C), according to the study of Donaldson (1976), which might indicate that the HBM represents the earliest stages of construction of the RLS (see also Greenwood, 1987; Greenwood *et al*., 1990). The morphology of olivine in the TSM (and the lowermost AMP) is generally coarse-grained and bladed–branching (Fig. 7e), suggesting a slightly reduced ΔT relative to the HBM of ~150–200°C, and pointing to crystal mush temperatures of ~900°C as the TSM and some AMP peridotites were being intruded. The AMP exhibits significantly greater variability in olivine texture than the other members (Fig. 20). Overall, it is envisaged that the complex interplay between small volume replenishments, time, and undercooling resulted in the diverse array of olivine textures observed in the AMP peridotites. There is an abundance of layers of harrisite dominated by hopper olivine morphologies, suggesting degrees of undercooling of ~50 ΔT°C and therefore a relatively hot crystal mush. However, there are less common examples of skeletal olivine-dominated harrisite in the AMP (see Online Appendix 2), suggesting that the crystal mush had the opportunity to cool significantly. These harrisite bodies may therefore represent some of the final magma emplacement events of the WLI (Fig. 20).

*Syn-magmatic reworking of harrisite in deforming crystal mush*

Some granular-textured peridotite layers contain megacrysts of harrisitic olivine, suggesting that at least some granular-textured peridotite formed contemporaneously with harrisite. Furthermore, the association of granular-textured peridotite with Cr-spinel seams (Fig. 3; Facies L) suggests a process like that proposed for harrisite formation, except that the intruding picrite may have carried an olivine cargo (Worrell, 2002), suppressing harrisitic olivine growth (Donaldson, 1976).

A dynamic, high-crystallinity framework undergoing sufficient shear stress to form hot tears is not necessarily conducive to forming fragile skeletal olivine crystals in harrisites. High strain environments would likely deform and/or fragment these crystals, particularly as harrisites formed within the shear zones and hot tears, i.e., the areas of greatest strain. The WLI, specifically the AMP, contains layers of porphyritic peridotite (Fig. 5e, 12), consisting of abundant blocky–rounded, cm-sized olivine megacrysts, which always carry a strong foliated oriented parallel to layering (Fig. 4j, 10). The layers are typically thin (<5 cm thick), with a 'groundmass' of fine-grained granular-textured olivine. Porphyritic peridotite layers are often associated with Cr-spinel seams, usually along the layer bases (or more rarely tops). The porphyritic layers themselves are generally Cr-spinel rich (>5%). As noted above, the megacrysts have abundant inclusions of skeletal magnetite while the groundmass olivine is inclusion free (Fig. 10b, c). The different characteristics of the two olivine populations points to an autocrystic origin for the large olivine crystals, i.e., they represent 'clasts'. O'Driscoll *et al.* (2007a) reported an occurrence of these megacrysts that showed imbrication fabrics at the outcrop-scale, and consequently suggested they represented fragments of harrisitic olivine that were reworked on the magma chamber floor. The presence of the skeletal magnetite inclusions points to deeper undercooling of the magmas that crystallised the megacrysts (see Barnes, 1985; Shore & Fowler, 1999; Godel *et al*., 2013).

Given that we suggest harrisite forms within the crystal mush, a re-evaluation of the petrogenesis of the porphyritic peridotites is required. We suggest that the porphyritic peridotite layers such as that illustrated in Figure 4j are harrisite sills that underwent shearing within the crystal mush, causing fragmentation of the large skeletal crystals within the hot tears and shear zones (see Hepworth *et al*., 2017), and producing the strong foliations that characterise both the megacrysts and groundmass olivine. O'Driscoll *et al*. (2015) showed that the porphyritic peridotites also exhibit a well-developed olivine lineation, supporting the idea that a component of simple shear was involved in fabric development. The consistency of thickness of the porphyritic peridotite layers might mean that this process is only important where the sill is thin, where magma-static pressure is overcome by shear stress, where the inflation rate (or flux rate) in the sill is too low. The relative thinness (< 5 cm) of the layers also precludes formation by bed-load transport within sills, particularly as imbrication of

olivine is not observed within harrisite layers (see Online Appendix 2). The disruption and disarticulation of homogenously crystallising harrisite would produce new heterogeneous nuclei, suppressing the ability of the magma to undercool, and forming granular-textured olivine (Donaldson, 1976).

**The petrogenesis of Cr-spinel seams in the Western Layered Intrusion**

*Textural evidence for in situ crystallisation of Cr-spinel seams within the WLI crystal mush*

The petrogenesis of Cr-spinel seams (chromitites, *sensu lato*) in layered intrusions is contentious. A variety of mechanisms has been proposed to explain the concentration of Cr-spinel in different layered intrusions, such as pressure changes and roof-rock assimilation in the Stillwater Complex, USA (Lipin, 1993; Spandler *et al*., 2005), magma-mixing in the Muskox Intrusion in Canada (Irvine, 1977), and stratified magma columns, crystal slurries, and cumulate assimilation in the Bushveld Complex, South Africa (Mondal & Mathez, 2007; Junge *et al*., 2014; Latypov *et al*. 2015). There have also been several models proposed for the petrogenesis of the Cr-spinel seams found in the RLS, including crystal settling and felsic cumulate (magma chamber floor) assimilation by primitive magma (e.g., mixing; Irvine; 1975; Henderson & Suddaby, 1971; O'Driscoll *et al*., 2009a; 2010). Though quite different in many respects, the models above are similar in that they all call for chromitite formation at the magma chamber floor. The WLI contains hundreds, if not thousands of Cr-spinel seams, which suggests numerous replenishment events. An array of outcrop- to crystal-scale features point to crystallisation of Cr-spinel seams on Rum *in situ* (O'Driscoll *et al*., 2010; Latypov *et al*., 2013). The close spatial association of Cr-spinel with harrisite in the WLI, where the seams occur along the bases, tops, and interiors of harrisite layers, also points to the formation of the Cr-spinel seams by *in situ* crystallisation. The presence of near vertically-oriented Cr-spinel seams within harrisite bodies also argues against crystal settling (Fig. 5e). The textures of many Cr-spinel seams, in which Cr-spinel occurs in the intercumulus spaces around olivine crystals, also makes crystal settling difficult to envisage (Jackson, 1961), particularly as the olivine displays corroded and deeply embayed shapes (Fig. 9a, f), suggesting a reaction between the two phases (necessarily also involving the interstitial melt). The close association of Cr-spinel seams with harrisite also points to formation

within the crystal mush, as it has been argued above that harrisite forms by intrusion of magma (see also Ballhaus, 1988; Latypov *et al*., 2015). This is particularly true for those seams found within, and on the upper surfaces of harrisite layers. Anastomosing Cr-spinel seams (Fig. 5d), as well as those that bifurcate, and exhibit braiding are also indicative of intra-mush processes. Similar features have been reported for chromitite seams in the Bushveld Complex (Voordouw *et al*., 2009), where intrusive chromitite has also been documented (Mukherjee *et al*., 2017). The petrographic observation that large optically continuous olivine crystals are cross-cut by Cr-spinel seams also constitutes evidence for seams forming within the crystal mush (Fig. 9f), as harrisitic olivine (which is cross-cut) requires near homogenous crystallisation conditions (Donaldson, 1974; 1976) so must pre-date the spinel and not represent overgrowth (see also Hepworth *et al*., 2017). This feature could not feasibly develop on the magma chamber floor.

The crystal size distribution (CSD) data presented here support the field and petrographic evidence; that the Cr-spinel seams formed by *in situ* crystallisation. The majority of CSD profiles for Cr-spinel seams in the WLI are log-linear at the larger size portions (Fig. 13), typical of a relatively simple relationship between nucleation and growth, without changing the crystallisation conditions (Marsh, 1998). There is a paucity of population densities of larger crystals, often cited as evidence of size-dependant sorting (Marsh, 1998; Higgins, 2002b), with similar profiles observed for Cr-spinel seams in the ELI (O'Driscoll *et al*., 2009a; 2010; Hepworth *et al*., 2017) and in the Coobina Layered Intrusion in Western Australia (Barnes & Jones, 2013), where *in situ* crystallisation has also been invoked. The general lack of complexity in the CSD profiles is a feature of all seam types (e.g., boundary, granular-textured), where even the population density of the CSD groups is very similar. Thus, despite the structural and lithological heterogeneity that is evident from the field observations of different Cr-spinel groups (e.g., continuity, host rock lithology, seam thickness, diffusiveness), the controls and limitations on Cr-spinel crystal nucleation and growth appear to be similar, suggesting a common petrogenetic origin.

At the smallest size fractions, many of the CSD profiles deviate from log linear behaviour and display humped profiles. This reduction in the smallest crystal size fraction could be a function of post-crystallisation coarsening or annealing (i.e., Ostwald ripening), resulting in a net loss of the

smallest crystals with minor increases in the larger grain sizes (see Higgins, 2002b). However, there is a lack of fanning in the large size fractions among CSD groups (Fig. 13) so textural coarsening has not operated on all size fractions. The prevalence of sharp downturns in the CSDs at small crystal sizes has been attributed to filter-pressing in crystal mushes (Higgins, 2002b; 2006). However, we do not envisage compaction as having been an important process during the construction of the WLI. Although granular-textured and hopper olivine-textured peridotites comprise rounded olivine crystals, which will compact if interstitial melt is present (McKenzie, 1984), Worrell (2002) deemed the effects of compaction to be negligible in the WLI based on a comprehensive study of olivine CSDs. One obvious difference can be found in the skeletal olivine-textured harrisites that yield log-linear Cr-spinel CSDs with no downturn at small crystal sizes. The Cr-spinel crystal populations in these peridotites are fine-grained in contrast to the CSDs for the hopper olivine peridotite-hosted seams and are also characterised by much higher nucleation densities. The high nucleation density of Cr-spinel may be a primary feature of the seams in skeletal olivine-textured harrisite layers or suggest that the process responsible for removing the smallest crystal sizes operated more efficiently in skeletal frameworks. For example, the profile shape may be a result of variable through-flow, removing smaller crystals i.e., an elutriation effect.

*Cr-spinel seam petrogenesis in focused zones of melt-rock reaction in the WLI cumulates*

Textural, petrographic, and field observations suggest that the Cr-spinel seams in the WLI crystallised *in situ* from a process that occurred repeatedly. As noted above, the intimate association of Cr-spinel seams with harrisites, whether seams occur within harrisite bodies or along their upper/lower surfaces, strongly points to a genetic relationship between them. Furthermore, this evidence also points to a ubiquitous formation mechanism for all seam types. Cr-spinel compositions in the WLI are variable, essentially the entire range of major element (e.g., Mg#, Cr#) variation reported from the rest of the RLS is present within the WLI Cr-spinel (Fig. 15). There is no clear geochemical distinction between boundary-type and granular-textured peridotite-hosted Cr-spinel seams (Figs. 15, 16). However, in comparison with these, Cr-spinel in harrisite-hosted seams are enriched in $Fe_2O_3$, with lower $Al_2O_3$ contents. This relationship has been attributed to the reaction of Cr-spinel with a relatively evolved

interstitial melt (O'Driscoll *et al*., 2009a; Lenaz *et al*., 2011; Leuthold *et al*., 2014; 2015). The most compositionally distinct Cr-spinel population occurs in the chromitite seams. Here, Cr-spinel has the highest $Al_2O_3$ contents in the WLI (~39 wt.%), as well as in the RLS overall (Cr# 0.29, Mg# 71.4; Fig. 15a). High Mg#-low Cr# Cr-spinel characterises the so-called 'Rum-trend' (Henderson, 1975; Barnes & Roeder, 2001), and is typically present in Cr-spinels at the bases of the ELI unit boundary seams. O'Driscoll *et al.* (2010) suggested that these compositions represent the closest approximation to the hybrid magma (picrite plus troctolite) that crystallised the Cr-spinels, a conclusion also reached by Bell & Claydon (1992) for Cr-spinel in coeval peridotites of the Skye igneous centre. Titanium ($Ti^{4+}$) is incompatible in Cr-spinel and serves as a potentially useful indicator of magmatic environment (Roeder & Campbell, 1985; Scowen *et al*., 1991; Barnes & Roeder, 2001; Wijbrans *et al*., 2015). In the WLI, the $TiO_2$ content of Cr-spinel is typically ~2 wt. % but can be as high as ~7 wt. % in harrisite-hosted seams. Chromitite seams have the lowest $TiO_2$ contents (<1 wt. %); like those reported from the unit boundary seams in the ELI by O'Driscoll *et al*. (2010). These show a congruous decrease in $TiO_2$ with Cr# (Fig. 15b). Low initial $TiO_2$ in the parental melt of the Cr-spinel seam is a function of the activity of $Al_2O_3$ (Kamenetsky *et al*., 2001), which in turn is controlled by the assimilant that triggered Cr-spinel crystallisation. For example, assimilation of plagioclase (or a plagioclase-normative liquid) increases $Al_2O_3$ in the melt, reducing the potential for uptake of $TiO_2$ into enter Cr-spinel (O'Driscoll *et al*., 2009a; 2010). High $TiO_2$ values are therefore attributable to postcumulus processes, which are enhanced in the porous skeletal frameworks of harrisite where $TiO_2$ is consistently high. Conversely, it may be possible that $TiO_2$ activity is buffered in chromitites (<1 wt.% $TiO_2$), but not in other seam types. There is a linear relationship with decreasing $TiO_2$ as $Al^{3+}$ increases through granular and harrisite, boundary, and chromitite (Fig. 15b). This corresponds more strongly with the abundance of Cr-spinel within the seam i.e., the more Cr-spinel per unit volume the more aluminous the spinel.

Electron microprobe traverses taken through seams reveal relatively constant Cr-spinel compositions, even in the thickest seams (up to 2cm), until above or below the limits of the seam, where Cr-spinel composition changes considerably (Fig. 17; see also Online Appendix 5). Above and below the seams, Cr-spinels are relatively enriched in $Fe_2O_3$ and $TiO_2$. In contrast, the composite

chromitite seam (AM18; Fig. 17) exhibits an internal step-change in $TiO_2$ content, which matches the position of the textural boundary (see also Online Appendix 5). A similar phenomenon has been reported from the UG-2 chromitite in the Bushveld Complex of South Africa, where repeated step-changes in the $TiO_2$ content of Cr-spinel throughout the seam were interpreted as reflecting incremental, rather than instantaneous, construction of the chromitite (Junge *et al*., 2014). The outer edges of the AM18 seam are coarser-grained, and CSD profiles taken from different portions of the seam display fanning (Fig. 13e), suggesting textural coarsening of the marginal zones with respect to the inner portion. The Cr-spinel crystals in the coarse-grained marginal zones of AM18 have lobate grain boundaries (Fig. 18). Compositional zoning also occurs in individual crystals, with enrichments of $TiO_2$ and $Fe_2O_3$ towards the edges of the crystals (see Fig. 18). These observations indicate a crystal-melt disequilibrium reaction during the growth of these crystals. Thus, it seems likely that the coarse-grained marginal zones of the composite Cr-spinel seam are the result of a supra-solidus textural equilibration process (i.e., annealing). However, it is not immediately clear why the thickness of the upper marginal zone is significantly greater than the lower zone (Fig. 18), given that the texture of the peridotite is identical on either side. One explanation might be the tendency for melt to migrate upwards, particularly as this process is occurring within the crystal mush where small degrees of overpressure will occur. This suggestion would necessitate the trapping of melt within this seam (or melt channel), with little or no exchange with the adjacent cumulate.

We find further support for a melt channel model from textural analysis. There is a strong correlation between spatial distribution and textural characteristics, which reveal a linear relationship between available space within the crystal mush (minimum crystallinity) and Cr-spinel abundance (Fig. 14b, c). Chromitite seams have the highest volumetric abundance of Cr-spinel, lowest crystallinity, and highest $Al^{3+}$compositions, suggesting there was more space for melt within the channel. Conversely, granular-types have a high crystallinity and lower volumetric abundance, something also mirrored in the clustering index (R-value; Fig. 14d), and therefore low $Al^{3+}$ compositions. There is also a decrease in olivine abundance and a change from euhedral to anhedral crystals along this trend, with the most anhedral (and presumably corroded) olivine occurring in

chromitites. Intermediary values also exist, forming a spectrum of textures and compositions, corresponding well to volumetric spinel abundance and crystallinity.

With the evidence presented above, notably of cross-cutting and anastomosing Cr-spinel seams (Figs. 5d; 9e), *in situ* crystallisation, and mineral chemistry, the Cr-spinel seams are best explained by progressive melt channel formation within the crystal mush. Each Cr-spinel seam preserves different degrees of melt through-flow, where granular-textured peridotite-hosted seams record the lowest volume of (porous) melt throughflow, while chromitite seams reflect the highest degree of (channelized) through-flow (see Fig. 21). We assessed the likelihood that melt might be able to flow through a semi-solid crystal mush over time-scales which fit the experimentally-derived dissolution rates of minerals such as plagioclase, considered here to be the critical assimilant that triggered Cr-spinel crystallisation (O'Driscoll *et al*., 2010; 2009a; Latypov *et al*., 2015; Hepworth *et al*., 2017). Using flow equations based on Darcy's law, the following equation can be determined:

$$q = \frac{(\varphi)(pB - pA)}{\mu}$$

where $q$ is the flux within the channel, φ is the permeability of the matrix, $pB$ is the bulk matrix density of the crystal mush (~3.049 g/cm$^3$, e.g., for a typical granular-textured peridotite modal mineralogy of 70% olivine, 20% plagioclase, 10% pyroxene), $pA$ is the bulk density of the liquid of 2.66 g/cm$^3$ (Holness *et al*., 2007), and μ is the viscosity of the liquid determined experimentally around ~1 Pa/s/m$^2$ by (Donaldson, 1976), with similar values used by Holness *et al*. (2007). From this, the velocity of melt ($v$) within the mush can be derived as:

$$v = \frac{q}{\Phi}$$

where $q$ is the flux determined from equation (1), and ϕ is the porosity of the bulk matrix (the crystal mush). A range of permeability and porosity values are possible, as the degree to which crystal mush was solidified when magma injection occurred is not known (see below), but based on previously modelled estimates, Holness *et al.* (2007) used a permeability value of $10^{-10}$ m$^2$ and noted that Elliot *et al.* (1997) suggested an even higher permeability of $10^{-9}$ m$^2$. The typically orthocumulate texture of the WLI peridotites, with crystallinities typically in the range 90–40%, would have had a significant

melt interstitial fraction. Furthermore, as the olivine crystal size in the WLI is typically > 1 mm, permeability could be higher still, i.e., > $10^{-8}$–$10^{-7}$ $m^2$ (von Bargen & Waff, 1986). At a permeability value of $10^{-8}m^2$, we calculate a bulk directional melt velocity of 0.099mm/hr. This value is of the same order magnitude as experimental calculations of plagioclase dissolution rates (~0.086 mm/hr; Donaldson, 1985) which might be dissolving at a similar rate to the melt flux to produce the Cr-spinel saturated liquid, allowing for steady propagation of the channel. The velocity of melt migration laterally through the crystal mush over length-scales of 1 m, even given the comparatively low porosities of 20% in the granular-textured peridotite, are comparable to crystallisation times of days and weeks for harrisitic olivine (O'Driscoll *et al*., 2007a). A minimum crystallinity of 5% in chromitite seams yields velocities of ~$m^2$/hr. We suggest therefore that composite chromitite seams, such as AM18 (Fig. 17; 18), where melt through-flow was channelized (i.e., not porous), represent an end-member of this process, where flow of melt within the channel progressively decreased crystallinity (i.e., olivine) by melt-rock reaction during chromitite development. The rates of melt migration calculated above are all in agreement with crystallisation timescales of harrisite from months to hours suggested by O'Driscoll *et al.* (2007a), particularly as we have suggested multiple sill-like intrusive events, which will keep the mush nearer to liquidus temperatures, facilitating the movement of melt within a hot, semi-solid crystal mush.

The transition from porous to channelized flow has been studied numerically in upper mantle peridotite bodies, including within ophiolites, and explains the formation of dunite bodies therein (e.g., Quick, 1981; Kelemen *et al*., 1995). Critically, this process produces a strong positive-feedback effect, whereby, as dissolution proceeds, permeability increases, thus allowing more melt through-flow, thereby increasing the rate of dissolution and porosity, and so on (Chadam *et al*., 1986; Ortoleva *et al*., 1987). This process was studied experimentally by Daines & Kolhstedt (1993; 1994) where the change from porous to channelized flow was achieved because of disequilibrium within the system (i.e., between the hybrid liquid and peridotite crystal mush), producing a porous reaction zone on the removal of phases (e.g., clinopyroxene and orthopyroxene). The combined petrographic, textural and chemical data presented here illustrate this continuum between porous (granular-type seams) and channelized flow (chromitite seams) of a Cr-spinel-saturated reactive melt though the crystal mush,

where the continuum between these end members is a function of melt volume and dissolution rates, with an ultimate control on the composition and texture of Cr-spinel within the seams (Fig. 21). The seams form synchronously with harrisite (i.e., picrite sills) in the same hot tears and shear zones, with the spatial relationship between the two controlled by how far the sill migrates along the hot tear (see Hepworth *et al*. 2017). Intra-harrisite seams form from the continued flow of melt within the rapidly crystallising framework, with multiple generations of melt recorded within Cr-spinel seam melt channels (Fig. 21). Based on our discovery of the clinopyroxene-rich roof zone (UAM) to the WLI, the evolved components (interstitial melt) of these seam-forming reactions may have escaped upwards through the cumulate pile (see discussion below).

The model presented in Figure 21 helps to solve the long-standing mass balance problem implicit in concentrating so much Cr in the seams compared to parental melts with ~3000 ppm Cr (i.e., Upton *et al*., 2002), as more melt has moved through the channel than is represented by the net volume of the seam. Our model also helps to account for the elevated base-metal sulphide and PGM populations in the chromitites compared to granular-type seams (e.g., Butcher *et al*., 1999; O'Driscoll *et al*., 2009b; Hepworth *et al*., 2017). It may be that our model could also be readily applied to a variety of Cr-spinel seams (and chromitites) in much larger intrusions such as the Bushveld and Stillwater Complexes, where sill emplacement has been recently recognised around chromitite-bearing units (Mungall *et al*., 2016; Mukherjee *et al*., 2017; Wall *et al*., 2018). Furthermore, it may be of particular importance where this PGE-mineralisation is found in conjunction with ultramafic pegmatoids like harrisite (e.g., Cawthorn & Boerst, 2006; Mondal & Mathez, 2007; Wilson, 2015).

**Late-stage infiltration metasomatism of crystal mush in the WLI: The UAM and TSM members**

*The Upper Ard Mheall roof zone*

Clinopyroxene is rare in the AMP, occurring in abundances <10 vol.% throughout most of the sequence until the top several tens of metres, where it increases to >20 vol.% across the AMP/UAM boundary (Fig. 6a, d). Compositional zoning in clinopyroxene crystals also becomes apparent at this interval. Plagioclase veins are very common in the UAM, which coupled with the increase in clinopyroxene abundance, points to the upward migration of evolved interstitial melts. The mineral

chemistry of clinopyroxene is distinct from the underlying AMP, with $TiO_2$ poor, high Mg# cores, and slightly lower Mg# and $TiO_2$-rich rims. $Cr_2O_3$ contents remain similar (Fig. 19a, b). The rim compositions overlap well with clinopyroxene from the underlying AMP, while the UAM clinopyroxene cores exhibit distinctly lower $Cr_2O_3$ and $TiO_2$ contents than other WLI clinopyroxene compositions (Figs. 19a, b). The UAM plagioclase is slightly more evolved (sodic) than that in the AMP, as reported by Worrell (2002), and the FeO content of the plagioclase is also marginally higher in the UAM than the AMP (Fig. 19c). The presence of more evolved mineral assemblages in the UAM supports a process involving the migration of an evolved clinopyroxene-saturated melt upwards through the crystal mush, promoting new rim growth onto pre-existing crystals and enriching the very top of the WLI mush, i.e., the UAM, in clinopyroxene. The balance of evidence above therefore suggests that the UAM represents a metasomatised zone of cumulate. Such a process has been well-documented for clinopyroxene oikocryst-bearing cumulates in the ELI (Holness *et al*., 2007; Leuthold *et al*., 2014). It follows that the metasomatising agent came from the crystal pile beneath and that the clinopyroxene-rich zone comprising the UAM is the roof zone to the AMP, and hence to the WLI. In the cumulate underlying the UAM, the repeated intrusion of new sills is likely to have inhibited clinopyroxene crystallisation, buffering the liquidus until later in the evolution of the crystal mush, and the evolved liquid was expelled upwards. Such a model is inconsistent with there being a sheet of magma above the crystal mush as an escaping clinopyroxene-rich melt would migrate into the chamber and presumably be mixed into the resident magma. This suggests instead that the WLI crystal mush was directly roofed by country rock and the most westerly dipping layers in the UAM may record the orientation of the roof/cumulate boundary (i.e., the same as the orientation of the contact with the Western Granite; Greenwood, 1987; Petronis *et al*. 2009).

*The Transitional Member metasomatic horizon*

The TSM is classified as ‘transitional’ because it represents a combination of features from the overlying and underlying members and was interpreted to represent an intermediary fractionation product of the WLI magma (Wadsworth, 1961). The TSM exhibits similarities to the overlying AMP, i.e., identical layering characteristics and lithologies (including Cr-spinel seams), but contains

abundant clinopyroxene-oikocrysts, a feature more consistent with the underlying gabbroic HBM. There are differences in the compositions of the primary minerals in different members. For example, the AMP and TSM have very similar plagioclase (core) compositions (An ~80 mol. %), while the HBM is more evolved, with more Fe-rich olivine (<Fo 70 mol. %) and more albitic plagioclase (<70 mol. %; Greenwood, 1987). Indeed, An-contents as low as 56 mol.% are revealed in the HBM (Fig. 19c). Normally-zoned rims of plagioclase from the TSM show a strong overlap with the plagioclase compositions from the HBM. The clinopyroxene compositions of the TSM and HBM overlap significantly, with similar trends observed between Mg# and $TiO_2$, while the AMP clinopyroxene compositions are scattered, tending to higher Mg# (Fig. 19b). The similarity in clinopyroxene chemistry between the HBM and TSM, and TSM plagioclase rim compositions with HBM plagioclase points to metasomatism of the TSM by evolved melt from the HBM. Cr-spinel chemistry in the TSM and HBM contain the most $Fe_2O_3$ and $TiO_2$-rich compositions, with crystals of ferroan-chromite and Cr-magnetite found alongside Cr-spinel in both members. Textural analysis of the Cr-spinel seams in the TSM suggests they have formed in a very similar environment to those in the AMP, with clear similarities in CSD characteristics (e.g., Figs. 13f; 14). However, Cr-spinel seams are not abundant in the TSM, and where present are extremely discontinuous (i.e., only traceable for a few centimetres), unlike those in the AMP. Cr-spinel in the TSM is also typically enclosed in clinopyroxene oikocrysts with little or no plagioclase present. This is an intriguing observation, as abundant Cr-spinel should not be able to co-crystallise in a clinopyroxene-saturated melt, as the excess $SiO_2$ should cause spinel to be re-dissolved (Morse, 1980). It is possible that this process has occurred and has been responsible for the extreme rarity of Cr-spinel seams in the TSM and heavily modified Cr-spinel compositions (Fig. 17; see Leuthold *et al*., 2014). The patchy zoning and intra-crystal resorption textures in intercumulus plagioclase in the TSM point to a dissolution process (Fig. 11a). Furthermore, large oikocrysts of clinopyroxene contain small, rounded and optically continuous olivine crystals inclusions (Fig. 11f), similar to textures observed by Barnes *et al.* (2016) in layered pyroxenites. Those authors suggested that this texture arises from infiltration of a comparatively siliceous melt, dissolving olivine and precipitating pyroxene (orthopyroxene in their case). However, clinopyroxene saturated melts have been shown to be particularly reactive, with the potential to

dissolve or significantly modify the existing cumulate mineralogy (Holness *et al*., 2007; Leuthold *et al*., 2014), supporting mineral chemical observations that a reactive clinopyroxene-normative melt was present throughout the formation of the TSM.

Based on the above discussion, we suggest that the TSM represents another metasomatic horizon within the WLI. The field observations (e.g., upward gradation of AMP/TSM boundary), and olivine morphological constraints discussed above suggest the TSM and AMP are petrogenetically related, sharing the same lithological and textural characteristics, while the HBM is distinctly gabbroic. The similarity of the TSM and HBM clinopyroxene chemistry and the high abundance of this phase in these members compared to the AMP suggest that the clinopyroxene-normative melt was sourced from the HBM. The infiltration metasomatic event saturated the crystal mush in clinopyroxene, forming large oikocrysts throughout the lowermost 45m of the AMP (now the TSM) and causing moderate but pervasive dissolution of existing plagioclase (Fig. 11a), Cr-spinel, and olivine, to produce the relict and reabsorption textures (Fig. 11f), and heavily modified Cr-spinel compositions (including Cr-magnetite; O'Driscoll *et al*., 2009a; Leuthold *et al*. 2014; 2015).

The HBM could evidently exchange interstitial melt with the TSM, but the relative timing of this process to emplacement of either member is still uncertain. The sharp discordant boundary between the HBM and TSM signifies a time-gap between both. Historically, it has been considered that emplacement of the HBM predates that of the TSM and AMP, and there is no new unambiguous evidence in this study to suggest otherwise. However, either intrusion of the AMP magmas into/onto the HBM, or intrusion of the HBM into the AMP could equally trigger the upward-percolating fluids that metasomatised the TSM. A scenario where the HBM is the younger intrusion would not create problems for the undercooling model presented above, provided the time-gap across the unconformity between the HBM and TSM was sufficient to allow the requisite undercooling of ~200 ΔT°C to form the coarse-grained bladed–skeletal olivine crystals that characterise the HBM (Fig. 20). Considering recent work on out-of-sequence layering in other layered intrusions (e.g., Mungall *et al*., 2016), we suggest that constraining the relative age of the HBM in the WLI represents an important avenue for future research.

## CONCLUSIONS

Contrary to the well-established view of the RLS as a classic example of a layered intrusion; built from an upward-younging stratigraphy and gravity settling of crystals to form cumulates at the base of the magma chamber floor, we conclude that the WLI originated as a series of sills into an incrementally developed crystal mush. Similar interpretations invoking sill emplacement have also been put forward for peridotite cumulates in the ELI, highlighting the importance of this underlying construction process for cumulates across the RLS (e.g., Hepworth *et al*., 2017). Our results provide evidence that Rum WLI was built-up of multiple, sill-like replenishment events into an incrementally developing crystal mush, where sills are best (but not exclusively) represented by harrisite. The emplacement of sills is facilitated by slow gravitational collapse of the high-crystallinity cumulate, producing hot tears and shear zones enabling magma injection and contemporaneous reworking of some crystallising sills, emphasising the dynamic crystal mush. The injection of new magma into the crystal mush formed Cr-spinel seams along the same tears and shear zones as invading sills in progressively developing (permeable to porous flow) melt channels, which given the high flux rates could have further developed as channels. The associated PGE-enrichment must therefore have occurred *within* the crystal mush. Despite the difference in scale between Rum and other intrusions (e.g., Bushveld), this conclusion has significant implications for the formation (and mechanism of enrichment) of Cr-spinel (and PGE)-horizons more generally in layered intrusions, traditionally assumed to occur at the magma chamber floor (e.g., Bushveld; UG2 or Merensky Reef). The evolution of the layered WLI crystal mush was likely highly chaotic, given its formation by the apparent spatially and temporally random juxtaposition of sills. However, because olivine is abundant, the undercooling (approximated from olivine morphology) can be used as a simple proxy for temperature (Donaldson, 1976), providing better insight into the WLI system, allowing a simplified timeline where sill-emplacement, Cr-spinel seam petrogenesis and metasomatic processes can be better understood. Lastly, the evidence for non-aggrading layered igneous bodies presented here has important implications for the build-up of other olivine-rich cumulates found at the base of many layered intrusions (e.g., Jackson, 1961; Wilson, 2015), where the current structural level is not necessarily unambiguous indicator of relative age.

## ACKNOWLEDGEMENTS

Scottish National Heritage (SNH) is thanked for sampling permission on the Isle of Rum during 2014–2016. Peter Greatbatch and David Wilde (Keele University) are thanked for excellent thin-section preparation, and Andreas Kronz for assistance with electron-microprobe analysis at the University of Göttingen. Madeline Humphreys, Wolf Maier, and an anonymous reviewer are thanked for their thoughtful critique which improved the quality of the manuscript. We would like to dedicate this paper to the memory of our esteemed co-author, friend and mentor, Henry Emeleus, who sadly passed away while this paper was in review.

## FUNDING

L.N.H acknowledges funding from a Natural Environmental Research Council (NERC) Studentship [Grant Number: 1361482] and Keele University. J.S.D. was supported by a UCD Seed Funding Grant and by Science Foundation Ireland Grant No. 13/RC/2092, which is co-funded under the European Regional Development Fund.

## REFERENCES

Ballhaus, C. (1988). Potholes of the Merensky reef at Branspruit shaft, Rustenburg platinum mines; primary disturbances in the magmatic stratigraphy. *Economic Geology* **83**, 1140–1158

Barnes, S.J. (1985) The petrography and geochemistry of Komatiite flows from the Abitibi greenstone-belt and a model for their formation. *Lithos* **18**, 241–270

Barnes, S.J., Mole, D.R., Le Vaillant, M., Campbell, M.J., Verrall, M.R., Roberts, M.P. & Evans, N.J. (2016). Poikilitic Textures, Heteradcumulates and Zoned Orthopyroxenes in the Ntaka Ultramafic Complex, Tanzania: Implications for Crystallization Mechanisms of Oikocrysts. *Journal of Petrology* **57**, 1171–1198

Barnes, S.J. & Jones, S. (2013). Deformed Chromitite Layers in the Coobina Intrusion, Pilbara Craton, Western Australia. *Economic Geology* **108**, 337–354

Barnes, S.J. & Roeder, P.L. (2001). The Range of Spinel Compositions in Terrestrial Mafic and Ultramafic Rocks. *Journal of Petrology* **42**, 2279–2302

Bédard, J. H., Sparks, R. S. J., Renner, R., Cheadle, M. J. & Hallworth, M. A. (1988). Peridotite sills and metasomatic gabbros in the Eastern Layered Series of the Rhum Complex. *Journal of the Geological Society, London* **145**, 207–224

Bell, B.R. & Claydon, R.V. (1992). The cumulus and post-cumulus evolution of chrome-spinels in ultrabasic layered intrusions: evidence from the Cuillin Igneous Complex, Isle of Skye, Scotland. *Contributions to Mineralogy and Petrology* **112**, 242–253

Boorman, S., Boudreau, A. & Kruger, F.J. (2004). The Lower Zone–Critical Zone transition of the Bushveld Complex: a quantitative textural study. *Journal of Petrology* **45**, 1209–1235

Butcher, A.R., Pirrie, D., Prichard, H.N. & Fisher, P. (1999). Platinum-group mineralisation in the Rum layered suite, Scottish Hebrides, UK. *Journal of the Geological Society, London* **156**, 213–216

Brandiss, M.E., Mason, S. & Winsor, K. (2014) Rhythmic Layering Formed by Deposition of Plagioclase Phenocrysts from Influxes of Porphyritic Magma in the Cuillin Centre, Isle of Skye. *Journal of Petrology* **55**, 1479–1510.

Brown, G.M. (1956). The layered ultrabasic rocks of Rhum, Inner Hebrides. *Philosophical Transactions of the Royal Society of London Series B* **668**, 1–53

Campbell, I.H. (1978). Some problems with the cumulus theory. *Lithos* **11,** 311–323

Cashman, K.V. &. Marsh, B.D. (1988). Crystal size distribution (CSD) in rocks and the kinetics and dynamics of crystallisation II. Makaopuhi lava lake. *Contributions to Mineralogy and Petrology* **99**, 292–305

Cawthorn, R.G. & Boerst, K. (2006). Origin of the Pegmatitic Pyroxenite in the Merensky Unit, Bushveld Complex, South Africa. *Journal of Petrology* **47**, 1509–1530

Chadam. J., Hoff, D., Merino, E., Ortoleva, P. & Sen, A. (1986) Reactive Infiltration Instabilities. *IMA Journal of Applied Mathematics* **36**, 207–221.

Daines, M. J. & Kohlstedt, D. L. (1993). A laboratory study of melt migration. *Philosophical Transactions: Physical Sciences and Engineering* **342**, 43–52

Daines, M. J. & Kohlstedt, D. L. (1994). The transition from porous to channelized flow due to melt/rock reaction during melt migration. *Geophysical Research Letters* **21**, 145–148

Donaldson, C.H. (1974). Olivine Crystal Types in Harrisitic Rocks of the Rhum Pluton and in Archaean Spinifex Rocks. *Geological Society of America Bulletin* **85**, 1721–1726

Donaldson, C.H. (1976). An Experimental Investigation of Olivine Morphology. *Contributions to Mineralogy and Petrology* **57**, 187–213

Donaldson, C.H. (1982). Origin of some of the Rhum harrisite by segregation of intercumulus liquid. *Mineralogical Magazine* **45**, 201–209

Donaldson, C.H. (1985). The rates of dissolution of olivine, plagioclase and quartz in a basaltic melt. *Mineralogical Magazine* **49**, 683–693

Droop, G.T.R. (1987). A general equation for estimating Fe3+ concentrations in ferromagnesian silicates and oxides from microprobe analyses using stoichiometric criteria. *Mineralogical Magazine* **51**, 431–435

Eales, H.V. & Cawthorn, R.G. (1996). The Bushveld Complex. *In*: Cawthorn, R.G *Layered igneous rocks. Developments in petrology, vol 15, Elsevier Science BV: Amsterdam*, 181-230

Elliot, M.T., Cheadle, M.J. & Jerram, D.A. (1997) On the identification of textural equilibrium in rocks using dihedral angle measurements. *Geology* **25**, 355–358

Emeleus, C.H. (1994). Rum solid geology map 1:20000. Scottish Natural Heritage

Emeleus, C.H. & Bell, B.R. (2005). *British Regional Geology: the Palaeogene Volcanic Districts of Scotland*. (4th Ed). Keyworth: British Geological Survey

Emeleus, C.H., Cheadle, M.J., Hunter, R.H., Upton, B.G.J. & Wadsworth, W.J. (1996). The Rum Layered suite. In: Cawthorn, R.G (ed). *Layered igneous rocks*. *Developments in petrology*, vol **15**, Elsevier Science BV: Amsterdam, 404–440

Emeleus. C.H. & Troll, V.R. (2014). The Rum Igneous Centre, Scotland. *Mineralogical Magazine* **78**, 805–839

Faure, F., Trolliard, G., Nicollet, C. & Montel, J-M. (2003). A developmental model of the olivine morphology as a function of the cooling rate and the degree of undercooling. *Contributions to Mineralogy and Petrology* **145**, 251–263

Geshi, N. (2001). Melt segregation by localized shear deformation and fracturing during crystallization of magma in shallow intrusions of the Otoge volcanic complex, central Japan. *Journal of Volcanology and Geothermal Research* **106**, 285–300.

Godel, B.M., Barnes, S.J., Gürer, D., Austin, P. & Fiorentini, M.L. (2013). Chromite in komatiites: 3D morphologies with implications for crystallization mechanisms. Contributions to Mineralogy and Petrology **165**, 173–189

González-Jiménez, J.M., Griffin, W.L., Proenza, J.A., Gervilla, F., O'Reilly, S.Y., Akbulut, M., Pearson, N.J. & Arai, S. (2014). Chromitites in ophiolites: How, where, when, why? Part II. The crystallization of chromitites. *Lithos* **189**, 140–158

Greenwood, R.C. (1987). Geology and petrology of the margin of the Rhum ultrabasic intrusion, Inner Hebrides, Scotland. *Unpublished PhD thesis.* University of St Andrews.

Greenwood, R.C., Donaldson, C.H. & Emeleus, C.H. (1990) The contact zone of the Rhum ultrabasic intrusion: evidence of peridotite formation from magnesian magmas. *Journal of the Geological Society, London* **147**, 209–212

Hamilton, M.A., Pearson, D.G., Thompson, R.N., Kelley, S.P. & Emeleus, C.H. (1998). Rapid eruption of Skye lavas inferred from precise U–Pb and Ar–Ar dating of the Rum and Cuillin plutonic complexes. *Nature* **394**, 260–263

Harker, A. (1908). The Geology of the Small Isles of Inverness-shire. *Memoir of the Geological Survey of Scotland*

Henderson, P. (1975). Reaction trends shown by chrome-spinels of the Rhum layered intrusion. *Geochimica et Cosmochimica Acta* **39**, 1035-1044

Henderson, P. & Suddaby, P. (1971). The Nature and Origin of the Chrome-Spinel of the Rhum Layered Intrusion. *Contributions to Mineralogy and Petrology* **33**, 21–31

Hepworth, L.N., O'Driscoll, B., Gertisser, R., Daly, J.S. & Emeleus, C.H. (2017). Incremental Construction of the Unit 10 Peridotite, Rum Eastern Layered Intrusion, NW Scotland. *Journal of Petrology* **58**, 137–166

Higgins, M.D. (1994). Numerical modelling of crystal shapes in thin-sections; estimation of crystal habit and true size. *American Mineralogist* **79**, 113–119

Higgins, M.D. (2002a). Closure in crystal size distributions (CSD), verification of CSD calculations, and the significance of CSD fans. *American Mineralogist* **81**, 171–175

Higgins, M.D. (2002b). A crystal size-distribution study of the Kiglapait layered mafic intrusion, Labrador, Canada: evidence for textural coarsening. *Contributions to Mineralogy and Petrology* **144**, 314–330

Higgins, M.D. (2006). *Quantitative textural measurements in igneous and metamorphic petrology*: Cambridge, Cambridge University Press, UK

Higgins, M.D. (2000). Measurement of Crystal Size Distributions. *American Mineralogist* **85**, 1105–1116

Holness, M.B. (2005). Spatial Constraints on Magma Chamber Replenishment Events from Textural Observations of Cumulates: the Rum Layered Intrusion, Scotland. *Journal of Petrology* **46**, 1585–1601

Holness, M.B. (2007). Textural immaturity of cumulates as an indicator of magma chamber processes: infiltration and crystal accumulation in the Rum Eastern Layered Intrusion. *Journal of the Geological Society, London* **164**, 529–539

Holness, M.B., Hallworth, M.A., Woods, A. & Sides, R.E. (2007). Infiltration Metasomatism of Cumulates by Intrusive Magma Replenishment: the Wavy Horizon, Isle of Rum, Scotland. *Journal of Petrology* **48**, 563–587

Holness, M.B., Sides, R.E., Prior, D.J., Cheadle, M.J. & Upton, B.G.J. (2012). The peridotite plugs of Rum: Crystal settling and fabric development in magma conduits. *Lithos* **135**, 23–40.

Holness, M.B., Vukmanovic, Z., Mariani, E. (2017) Assessing the Role of Compaction in the Formation of Adcumulates: a Microstructural Perspective. *Journal of Petrology* **58**, 643–674

Holness, M.B. & Winpenny, B. (2008). The Unit 12 allivalite, Eastern Layered Intrusion, Isle of Rum: a textural and geochemical study of an open-system magma chamber. *Geological Magazine* **146**, 437–450.

Humphreys, M.C.S, & Holness, M.B. (2010). Melt-rich segregations in the Skaergaard Marginal Border Series: Tearing of a vertical silicate mush. *Lithos* **119**, 181–192

Irvine, T.N. (1977). Origin of chromitite layers in the Muskox intrusion and other stratiform intrusions: A new interpretation. *Geology* **5**, 273–277

Jackson, E.D. (1961). Primary Textures and Mineral Associations in the Ultramafic Zone of the Stillwater Complex, Montana. *Geological Survey Professional Paper* **358**

Jerram, D.A., Cheadle, M.J., Hunter, R.H. & Elliot, M.T. (1996). The spatial distribution of grains and crystals in rocks. *Contributions of Mineralogy and Petrology* **125**, 60–74

Jerram, D.A., Cheadle, M.J. & Philpotts, A.R. (2003). Quantifying the Building Blocks of Igneous Rocks: Are Clustered Crystal Frameworks the Foundation? *Journal of Petrology* **44**, 2033–2051

Junge, M., Oberthür, T. & Melcher, F. (2014). Cryptic variation of chromite chemistry, platinum group element and platinum group mineral distribution in the UG-2 chromitite: an example from the Karee mine, western Bushveld Complex, South Africa. *Economic Geology* **109**, 795–810

Kamenetsky, V.S., Crawford, A.J. & Meffre, A. (2001) Factors Controlling Chemistry of Magmatic Spinel: an Empirical Study of Associated Olivine, Cr-spinel, and Melt Inclusions from Primitive Rocks. *Journal of Petrology* **42**, 655–671.

Kelemen, P., Shimizu, N. & Salters, V.J.M. (1995). Extraction of mid-ocean-ridge basalt from the upwelling mantle by focused flow of melt in dunite channels. *Nature* **375**, 747–753

Latypov, R., Chistyakova, S., Page, A. & Hornsey, R. (2015). Field evidence for the *in situ* crystallisation of the Merensky Reef. *Journal of Petrology* **56**, 2341–2372

Latypov, R., O'Driscoll, B. & Lavrenchuk, A. (2013). Towards a model for the *in situ* origin of PGE reefs in layered intrusions: insights from chromitite seams of the Rum Eastern Layered Intrusion, Scotland. *Contributions to Mineralogy and Petrology* **166**, 309–327

Le Maitre, R.W. ed. (2002) *Igneous Rocks: A Classification and Glossary of Terms* Cambridge University Press, Cambridge, UK.

Lenaz, D., O'Driscoll, B. & Princivalle, F. (2011). Petrology of the anorthosite–chromitite seam association: crystal-chemical and petrological insights from the Rum Layered Suite, NW Scotland. *Contributions to Mineralogy and Petrology* **162**, 1201–1213

Leuthold, J., Blundy, J.D. & Brooker, R.A. (2015). Experimental petrology constraints on the recycling of mafic cumulate: a focus on Cr-spinel from the Rum Eastern Layered Intrusion, Scotland. *Contributions to Mineralogy and Petrology* **170**: 12

Leuthold, J., Blundy, J.D., Holness, M.B. & Sides, R. (2014). Successive episodes of reactive liquid flow through a layered intrusion (Unit 9, Rum Eastern Layered Intrusion, Scotland). *Contributions to Mineralogy and Petrology* **167**, 1021–1038

Lipin, B.R. (1993). Pressure Increases, the Formation of Chromite Seams, and the Development of the Ultramafic Series in the Stillwater Complex, Montana. *Journal of Petrology* **34**, 955–976

Lofgren, G.E. & Donaldson, C.H. (1975). Curved branching crystals and differentiation in comb-layered rocks. *Contributions to Mineralogy and Petrology* **49**, 309–319

Maier, W.D., Barnes, S.-J., Groves, D.I. (2013) The Bushveld Complex, South Africa: formation of platinum–palladium, chrome- and vanadium-rich layers via hydrodynamic sorting of a mobilized cumulate slurry in a large, relatively slowly cooling, subsiding magma chamber. *Mineralium Deposita* **48**, 156

Marsh, B.D. (1998). On the Interpretation of Crystal Size Distributions in Magmatic Systems. *Journal of Petrology* **39**, 553–599

Marsh, B.D. (2002). On bimodal differentiation by solidification front instability in basaltic magmas, part 1: Basic mechanics. *Geochimica et Cosmochimica Acta* **66** (12), 2211–2229.

McBirney, A.R. & Nicolas, A. (1997). The Skaergaard Layered Series. Part II. Magmatic flow and Dynamic Layering. *Journal of Petrology* **38**, 569–580.

McKenzie, D. (1984). The Generation and Compaction of Partially Molten Rock. *Journal of Petrology* **25**, 719–765

Means, W.D. & Park, Y. (1994). New experimental approach to understanding igneous texture. *Geology* **22**, 323–326.

Morse, S.A. (1980). *Basalts and phase diagrams*. Springer Verlag, New York. 493 pp

Mock, A. & Jerram, D.A. (2005). Crystal Size Distributions (CSD) in Three Dimensions: Insights from the 3D Reconstruction of a Highly Porphyritic Rhyolite. *Journal of Petrology* **46**(8), 1525–1541

Mondal, S.K. & Mathez, E.A. (2007). Origin of the UG2 chromitite seam layer, Bushveld Complex. *Journal of Petrology* **48**, 495–510

Mukherjee, R., Latypov, R. & Balakrishna, A. (2017). An intrusive origin of some UG-1 chromitite layers in the Bushveld Igneous Complex, South Africa: Insights from field relationships. *Ore Geology Reviews* (in press).

Mungall, J.E., Kamo, S.L. & McQuade, S. (2016). U-Pb geochronoglogy documents out-of-sequence emplacement of ultramafic layers in the Bushveld Igneous Complex of South Africa. *Nature Communications* **7**, 13385

Mungall, J.E & Naldrett, A.J, 2008. Ore Deposits of the Platinum-Group Elements. *Elements* **4**, 253–258

Namur, O., Humphreys, M.C.S. & Holness, M.B. (2013). Lateral Reactive Infiltration in a Vertical Gabbroic Crystal Mush, Skaergaard Intrusion, East Greenland. *Journal of Petrology* **54**, 985–1016.

O'Driscoll, B., Donaldson, C.H., Daly, J.S. & Emeleus, C.H. (2009a). The roles of melt infiltration and cumulate assimilation in the formation of anorthosite and a Cr-spinel seam in the Rum Eastern Layered Intrusion, NW Scotland. *Lithos* **111**, 6–20

O'Driscoll, B., Donaldson, C.H., Troll, V.R., Jerram, D.A. & Emeleus, C.H. (2007a). An Origin for Harrisitic and Granular Olivine in the Rum Layered Suite, NW Scotland: a Crystal Size Distribution Study. *Journal of Petrology* **48**, 253–270

O'Driscoll, B., Emeleus, C.H., Donaldson, C.H. & Daly, J.S. (2010). Cr-spinel Seam Petrogenesis in the Rum Layered Suite, NW Scotland: Cumulate Assimilation and *in situ* Crystallisation in a Deforming Crystal Mush. *Journal of Petrology* **51**, 1171–1201

O'Driscoll, B., Day, J.M.D., Daly, J.S., Walker, R.J. & McDonough, W.F. (2009b). Rhenium–osmium isotopes and platinum-group elements in the Rum Layered Suite, Scotland: Implications for Cr-spinel seam formation and the composition of the Iceland mantle anomaly. *Earth and Planetary Science Letters* **286**, 41–51

O'Driscoll, B., Ferré, E.C., Stevenson, C.T.E., & Magee, C. (2015). The significance of Magnetic Fabric in Layered Mafic-Ultramafic Intrusions. In: Charlier B., Namur, O., Latypov, R. & Tegner, E. (eds.) *Layered Intrusions*. Springer Geology, Dordrect, Netherlands.

O'Driscoll, B., Hargraves, R.B., Emeleus, C.H., Troll, V.R., Donaldson, C.H. & Reavy, R.J. (2007b). Magmatic lineations inferred from anisotropy of magnetic susceptibility fabrics in Units 8, 9, and 10 of the Rum Eastern Layered Series, NW Scotland. *Lithos* **98**, 27–44

O'Driscoll, B. & VanTongeran, J.A. (2017). Layered Intrusions: From Petrological Paradigms to Precious Metal Repositories. *Elements* **13**, 383–389.

Ortoleva, P., Merino, E., Moore, C. & Chadam, J. (1987). Geochemical self-organisation I: reaction-transport feedbacks and modelling approach. *American Journal of Science* **287**, 979–1007

Palacz, Z.A. & Tait, S.R. (1985). Isotopic and geochemical investigation of unit 10 from the Eastern Layered Series of the Rhum Intrusion, Northwest Scotland. *Geological Magazine* **122**, 485–490

Petronis, M. S., O'Driscoll, B., Troll, V. R., Emeleus, C. H. & Geissman, J. W. (2009). Palaeomagnetic and anisotropy of magnetic susceptibility data bearing on the emplacement of the Western Granite, Isle of Rum, NW Scotland, *Geological Magazine* **146**, 419–436

Philpotts, A.R., Carroll, M. & Hill, J.M. (1996). Crystal-Mush Compaction and the Origin of Pegmatitic Segregation Sheets in a Thick Flood-Basalt Flow in the Mesozoic Hartford Basin, Connecticut. *Journal of Petrology* **37**, 811–836.

Quick, J.E. (1981). The Origin and Significance of Large, Tabular Dunite Bodies in the Trinity Peridotite, Northern California. *Contributions to Mineralogy and Petrology* **78**, 413–422

Quintiliani, M., Andreozzi, G.B. & Graziani, G. (2006). Fe2+ and Fe3+ quantification by different approaches and fO2 estimation for Albanian Cr-spinels. *American Mineralogist* **91**, 907-916

Renner, R. & Palacz, Z. (1987). Basaltic replenishment of the Rhum magma chamber: evidence from unit 14. *Journal of the Geological Society* **144**, 961–970.

Roeder, P.L.& Campbell, I.H. (1985). The Effect of Postcumulus Reactions on Composition of Chrome-spinels from the Jimberlana Intrusion. *Journal of Petrology* **26**, 763–786.

Schneider, C. A., Rasband, W. S. & Eliceiri, K. W. (2012). NIH Image to ImageJ: 25 years of image analysis, *Nature methods* **9** 671-675

Scowen, P.A.H., Roeder, P.L. & Helz, R.T. (1991). Requilibration of chromite within Kiliauea Iki lava lake, Hawaii. *Contributions to Mineralogy and Petrology* **107**, 8–20.

Shore, M. & Fowler, A.D. (1999). The origin of spinifex texture in komatiites. *Nature* **397**, 691–694

Spandler, C., Mavrogenes, J. & Arculus, R. (2005). Origin of chromitites in layered intrusions: Evidence from chromite-hosted melt inclusions from the Stillwater Complex. *Geology* **33**, 893–896

Sparks, R.J.S. & Huppert, H.E. (1984). Density changes during the fractional crystallization of basaltic magmas: fluid dynamic implications. *Contributions to Mineralogy and Petrology* **85**, 300–309.

Špillar, V. & Dolejš, D. (2014) Kinetic model of nucleation and growth in silicate melts: implications for igneous textures and their quantitative description. *Geochimica et Cosmochimica Acta* **131**, 164–183

Špillar, V. & Dolejš, D. (2015a). Heterogeneous nucleation as the predominant mode of crystallization in natural magmas: numerical model and implications for crystal-melt interaction. *Contributions to Mineralogy and Petrology* **169**, 4

Tait, S.R. (1985). Fluid dynamic and geochemical evolution of the Cyclic Unit 10: Rhum intrusion. *Geological Magazine* **122**, 469–484

Tegner, C. & Robins, B. (1996). Picrite sills and crystal-melt reactions in the Honningsvåg Intrusive Suite, northern Norway. *Mineralogical Magazine* **60**, 53–66

Tepley, F.J. III. & Davidson, J.P. (2003). Mineral-scale Sr-isotope constraints on magma evolution and chamber dynamics in the Rum Layered Intrusion, Scotland. *Contributions to Mineralogy and Petrology* **145**, 628–641

Upton, B.G.J., Scovgaard, A.C., McClurg, J., Kirstein, L., Cheadle, M., Emeleus, C.H., Wadsworth, W.J. & Fallick, A.E. (2002). Picritic magmas and the Rum ultramafic complex, Scotland. *Geological Magazine* **139**, 437–452

von Bargen, N. & Waff, H.S. (1986) Permeabilities, interfacial areas and curvatures of partially molten systems: results of numerical computations of equilibrium microstructures. *Journal of Geophysical Research* **91**, 9261–9276

Volker, J.A, & Upton, B.G.J. (1990). The structure and petrogenesis of the Trallval and Ruinsival areas of the Rhum ultrabasic complex. *Transactions of the Royal Society of Edinburgh: Earth Sciences* **81**, 69–88.

Voordouw, R., Gutzmer, J., Beukes, N.J. (2009). Intrusive origin for Upper Group (UG1, UG2) stratiform chromitite seams in the Dwars River area, Bushveld Complex, South Africa. *Contributions to Mineralogy and Petrology* **97**, 75–94

Vukmanovic, Z., Barnes, S.J., Reddy, S.M., Godel, B. & Fiorentini, M.L. (2013). Morphology and microstructure of chromite crystals in chromitites from the Merensky Reef (Bushveld Complex, South Africa). *Contributions to Mineralogy and Petrology* **165**, 1031–1050

Wadsworth, W.J. (1961). The layered ultrabasic rocks of south-west Rhum, Inner Hebrides. *Philosophical Transactions of the Royal Society of London. Series B* **244**, 21–64

Wager, L.R., Brown, G.M. & Wadsworth, W.J. (1960). Types of Igneous Cumulates. *Journal of Petrology* **1**, 73–85

Wager, L. R. & Deer, W. A. (1939). Geological investigations in East Greenland. Part III. The petrology of the Skaergaard intrusion, Kangerdlussuaq, East Greenland. *Meddelelser om Grønland* **105**

Wall. C.J., Scoates, J.S., Weis, D., Friedman, R.M., Amini, M. & Meurer, W.P. (2018) The Stillwater Complex: Integrating Zircon Geochronological and Geochemical Constraints of the Age, Emplacement History and Crystallisation of a Large, Open-System Layered Intrusion. *Journal of Petrology* **59**, 153–190

Wijbrans, C.H., Klemme, S., Berndt, J. & Vollmer, C. (2015). Experimental determination of trace element partition coefficients between spinel and silicate melt: the influence of chemical composition and oxygen fugacity. *Contributions to Mineralogy and Petrology* **169**, 1128-1161

Wilson, A.H. (2015) The Earliest Stages of Emplacement of the Eastern Bushveld Complex: Development of the Lower Zone, Marginal Zone and Basal Ultramafic Sequences. *Journal of Petrology* **56**, 347–388

Worrell, L.M. (2002). The Origin of Igneous Cumulates: Integrated Studies of Peridotites from the Western Layered Series of the Rum Layered Intrusion. *Unpublished Ph.D Thesis*, University of Liverpool

## FIGURE CAPTIONS

Figure 1. (a) Location of the Isle of Rum within Scotland. (b) Location of the Isle of Rum within Scotland. (b) Constituent intrusions of the Rum Layered Series (RLS): CI = Central Intrusion, WLI = Western Layered Series, ELI = Eastern Layered Intrusion (adapted from Emeleus, 1994).

Figure 2. Geological map of the Western Layered Series (WLI) mapped as part of this study. Note that topographic contours are in feet. Cross-sections of the WLI can be accessed in Online Appendix 1.

Figure 3. Simplified ‘facies’ scheme depicting lithological relationships of peridotite (and Cr-spinel seams) through the AMP, see text for further description. The reader is urged to see the high resolution graphic logs in Online Appendix 2.

Figure 4. Field relationships of peridotite in the AMP. (a) Bifurcating harrisite around fine grained granular-textured peridotite. Note the high intercumulus plagioclase fraction of granular-textured peridotite in contact with harrisite. (b) Irregular harrisite layer with upward oriented apophyses linked to the succeeding layer, see also the large branching olivine crystals (arrowed) protruding into the granular-textured peridotite. (c) Typical layering of harrisite and granular-textured peridotite, with irregular (upper) boundaries of harrisite. Note also the bifurcation in the top right, in the thickest harrisite layer. (d) Downward-oriented harrisite apophysis. Note possible continuation of plagioclase-rich layers through the apophysis. (e) ‘Harrisite column’ with metres high harrisite and deflected granular-textured peridotite. (f) Hopper dominated harrisite, with cm-sized rounded–hopper olivine crystals. (g) Strongly foliated harrisite with dome-like oriented elongated olivine crystals.

Figure 4 continued. (h) Cr-spinel seam showing a Cr-spinel seam cross-cut by an upward-oriented harrisite apophysis (seam outlined), close to which the Cr-spinel suddenly becomes disseminated. (i) Block of layered granular peridotite, as shown by layering oriented ~45º from normal shallowly dipping layers ~15º. (j) ‘Porphyritic peridotite’ layers within granular-textured peridotite. Arrowed example is composed almost entirely of strongly aligned cm-sized branching–elongate olivine crystals.

Figure 5. Cr-spinel seams in the AMP. (a) High concentration granular-type Cr-spinel seam in coarse-grained granular-textured peridotite. (b) Boundary-type Cr-spinel seam on the upper surface of coarse-grained granular-textured to hopper peridotite. (c) Chromitite seam within harrisite. Note the boundary irregularities along strike where Cr-spinel occupies intercumulus space around harrisitic olivine. (d) Anastomosing chromitite seam in fine-grained granular-textured peridotite. (e) Multiple-seams within harrisite layer (arrowed) with various concentrations of Cr-spinel. Note specifically the

vertical orientation of seams towards the left (arrowed). (f) Very coarse Cr-spinel seam from a harrisite-hosted Cr-spinel seam, scale bar = 2 mm.

Figure 6. Field relationships of the UAM. (a) Boundary between the AMP and UAM with distinct grey colour change due to the increase of plagioclase abundance. (b) Layering defined by subtle changes in intercumulus volume. (c) Sub-vertically oriented hopper-harrisite dyke cross-cutting layering. (d) Highly pyroxene-rich (wehrlitic) peridotite layer.

Figure 7. Field relationships of the TSM. (a) Typical layering between harrisite and wehrlitic granular-textured peridotite. White scale bar ~5cm (b) Granular-type Cr-spinel seam. Note the highly discontinuous nature, even on a cm-scale. (c). Undulose upper surface of harrisite with well-layered granular-textured peridotite. (d) Upward oriented apophysis (bridge) linked between harrisite layers with granular-textured peridotite in between. (e) Very coarse, highly skeletal olivine. Note also the gabbroic pegmatite common in the upper TSM. (f) Complex harrisite in the upper TSM with hopper harrisite zones.

Figure 8. Field relationships in the HBM. (a) Typical layering within the upper portions of the HBM with harrisite and gabbro layers. (b) Very coarse, highly skeletal olivine (arrowed) in harrisite with irregular upper surface (shown by black dashed line). (c) Bifurcating, complex harrisite layer (boundaries shown by black dashed lines). (d) Strong foliation of granular-textured peridotite (arrowed) beneath harrisite layer. (e) Variation in gabbro textures in succession (arrowed) (f) Leucogabbro layer within olivine-gabbro.

Figure 9. Petrography of the AMP. (a) Patchy zoning of plagioclase in proximity to Cr-spinel seam. (b) Patchy zoning in rare clinopyroxene oikocryst. (c) Foliated olivine within Cr-spinel seam. (d) ‘Dunitic-peridotite’ with polyhedral olivine arrangement with 120° triple-junctions (circled). (e) Cr-spinel seam cross-cutting large olivine crystal (outlined) across the top surface of a chromitite seam within harrisite. Note the high birefringence (olivine) inclusions in Cr-spinel close to the large olivine.

(f) Reflected light image displaying sulphide and metal phases associated with Cr-spinel, including sieve texture of Cr-spinel by sulphide.

Figure 10. Porphyritic peridotite in the AMP. (a) Centimetre-sized blocky–elongate olivine crystals are part of porphyritic peridotite. Note the narrow (thin black lines), aligned magnetite inclusions throughout the crystal (arrowed examples). (b) large, blocky olivine crystals, with skeletal magnetite inclusions highlighted in (c).

Figure 11. Petrography of the TSM. (a) High abundance patchy zoning of intercumulus plagioclase, with highly skeletal, optically continuous harrisitic olivine. (b) Irregular zoning of clinopyroxene (outlined zones) (c) Cumulus and intercumulus (texture) clinopyroxene with exsolution lamellae. (d) Discontinuous Cr-spinel seam between wehrlitic and feldspathic peridotite. (e) Cr-spinel seam with intercumulus clinopyroxene, also displaying exsolution lamellae. Note the lack of plagioclase. (f) Large, intercumulus clinopyroxene with optically continuous, rounded olivine inclusions in circular arrangement. (g) Reflected light image showing abundant sulphides, with spatially association with Cr-spinel and replacement texture in wehrlitic peridotite.

Figure 12. Petrography of the HBM. (a) Thin skeletal olivine typical in the HBM. (b) Cumulus appearing zoned plagioclase (arrowed). (c) Extremely irregular zoning in coarse clinopyroxene oikocryst. (d) Typical gabbro from the HBM, with rounded cumulus olivine and abundant intercumulus pyroxene. Note the zoning in plagioclase (arrowed). (e) Cumulus (appearing) alkali-feldspar (orthoclase) with abundant alblitic perthites and rim. (f) Reflected light image of highly skeletal spinel (magnetite–Cr-magnetite) from HBM gabbro.

Figure 13. CSD profiles of Cr-spinel seams from the AMP and TSM of Cr-spinel types in this study, with representative texture maps of the seam-groups defined in this paper. Output data can be found in Online Appendix 3.

Figure 14. Selected CSD derivative plots for Cr-spinel seams in this study. (a) Characteristic length (CL) versus volumetric percentage. Note the separation of the chromitite seams. (b) Negative correlation ($R^2 = 0.77$) of volumetric percentage of Cr-spinel versus crystallinity for Cr-spinel seams with a similar separation of chromitite as in (a). (c) Good correlation between the vol.% abundance of Cr-spinel and R-value. (d) Correlation between crystallinity (vol. % olivine) and R-value, suggesting a strong relationship with available space and crystallisation of Cr-spinel.

Figure 15. (a) Mg# vs Cr# and (b) Cr# vs $TiO_2$ wt. % plot for Cr-spinel seams from the WLI, including reference Cr-spinel from across the RLS. Unit 7, 8, 11, 12 data from O'Driscoll *et al.* (2009a; 2010). Unit 9 data from Holness *et al.* (2007), Unit 10 data from Hepworth *et al.* (2017), and M9 picrite dyke of Upton *et al.* (2002) from O'Driscoll *et al.* (2009a).

Figure 16. Trivalent ternary plots for Cr-spinel from the WLI. Peridotite hosted and other Cr-spinel seam data have been added for reference. Unit 7, 8, 11, 12 data from O'Driscoll *et al.* (2009a; 2010). Unit 9 data from Holness *et al.* (2007), Unit 10 data from Hepworth *et al.* (2017), and M9 picrite dyke of Upton *et al.* (2002) from O'Driscoll *et al.* (2009a). Errors are smaller than point size.

Figure 17. Cr-spinel seam traverses through Cr-spinel seams from the WLI. AM6 is a diffuse, boundary-type seam, AM18 is a composite chromitite seam from the AMP, while TM1 is a laterally discontinuous Cr-spinel seam from the TSM. Note the mirrored trends in AM6 and TM1 on either side of the seam, with enhanced $TiO_2$ contents in TM1. Note also the kinks in a stable composition through AM18 (arrowed) where textural changes are observed (highlighted), with another potential kink within AM6 seam, where the Cr-spinel becomes more diffuse. Errors smaller than point size.

Figure 18. Back-scattered electron image of a single crystal traverse of Cr-spinel from coarse textural zone in composite chromitite seam (arrowed) in sample AM18, showing increases in $TiO_2$ and $Fe_2O_3$ towards the lobate rim. Note also the abundance of rounded inclusions (typically with amphibole, plagioclase ± sulphide) in the core. Errors are smaller than point size.

Figure 19. Clinopyroxene and plagioclase mineral chemistry from the WLI. (a) $Cr_2O_3$ wt. % versus Mg# plot for clinopyroxene. (b) $TiO_2$ versus Mg# plot for clinopyroxene. (c) FeO wt.% versus anorthite mol. % plot for plagioclase. Data from Worrell (2002) has been added for comparison. See text for discussion.

Figure 20. Conceptual model for the formation of the WLI, including simple thermal history depicted by olivine texture at each stage (see Donaldson, 1976). (a) Emplacement of the WLI and rapid increase in temperature of the crystal mush due to high intrusion rate, restricting the undercooling to incoming picrite sills, resulting in granular-textured peridotite (and some hopper dominated harrisite sills). (b) After a period of quiescence (or reduced magma flux), the crystal mush cools, such that the input of new sills undergo higher degrees of undercooling, producing more hopper and branching olivine forms (i.e., harrisite). During the process of sill emplacement, evolved cpx-rich melt will migrate to the top of the crystal mush, pooling to form the UAM. (c) As the crystal mush continues to cool with time, fresh sills undergo higher degrees of undercooling, forming more complex olivine morphologies. Here, the intrusion of the HBM occurred, with the most complex olivine forms, suggesting the highest degrees of undercooling (see Fig. 8b). (d) Emplacement of the HBM at the base of the WLI produces a metasomatic horizon by partially melting the overlying crystal mush, saturating it in clinopyroxene, forming the TSM. Any injection of new sills will form rarer, highly complex olivine morphologies due to high degrees of undercooling (found mostly within the HBM).

Figure 21. Conceptual model depicting the petrogenesis of harrisite and Cr-spinel within hot tears and melt channels within a layered, shearing, peridotite crystal mush, with petrographic examples of the end member and intermediary Cr-spinel seams described in the text.

Figure 1

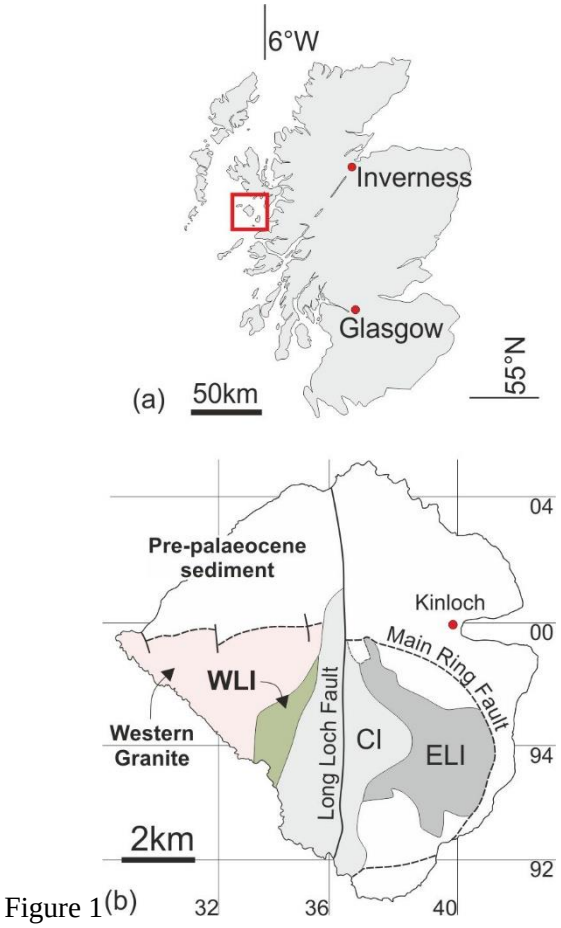


Figure 1

Figure 2

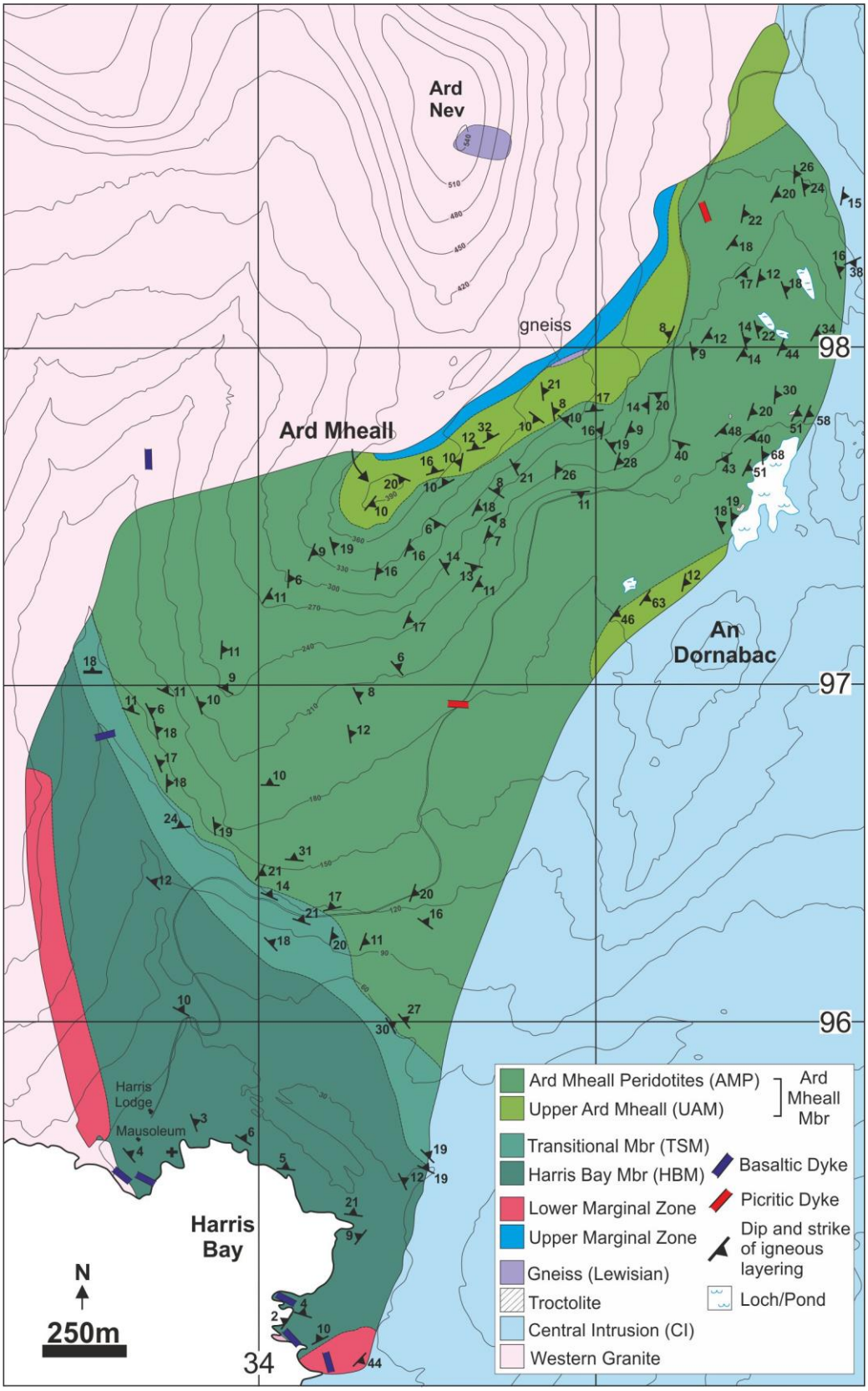
Ard
Nev
gneiss
Ard Mheall
An
Dornabac
98
97
96
34
Harris
Lodge
Mausoleum
Harris
Bay
N
250m
Ard Mheall Peridotites (AMP)
Upper Ard Mheall (UAM)
Ard Mheall Mbr
Transitional Mbr (TSM)
Harris Bay Mbr (HBM)
Lower Marginal Zone
Upper Marginal Zone
Gneiss (Lewisian)
Troctolite
Central Intrusion (CI)
Western Granite
Basaltic Dyke
Picritic Dyke
Dip and strike of igneous layering
Loch/Pond

Figure 3

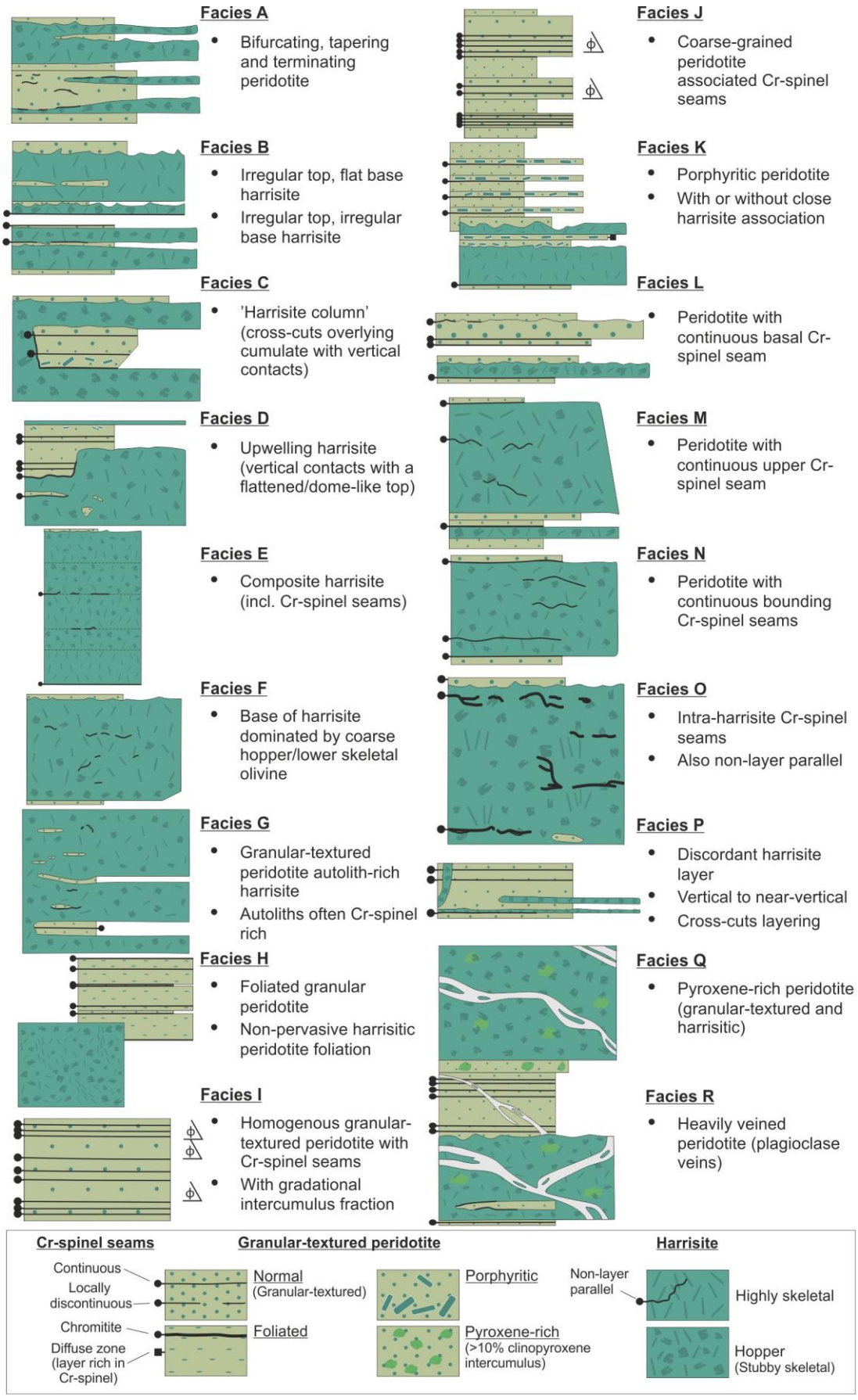
Facies A
Bifurcating, tapering and terminating peridotite
Facies B
Irregular top, flat base harrisite
Irregular top, irregular base harrisite
Facies C
'Harrisite column' (cross-cuts overlying cumulate with vertical contacts)
Facies D
Upwelling harrisite (vertical contacts with a flattened/dome-like top)
Facies E
Composite harrisite (incl. Cr-spinel seams)
Facies F
Base of harrisite dominated by coarse hopper/lower skeletal olivine
Facies G
Granular-textured peridotite autolith-rich harrisite
Autoliths often Cr-spinel rich
Facies H
Foliated granular peridotite
Non-pervasive harrisitic peridotite foliation
Facies I
Homogenous granular-textured peridotite with Cr-spinel seams
With gradational intercumulus fraction
Facies J
Coarse-grained peridotite associated Cr-spinel seams
Facies K
Porphyritic peridotite
With or without close harrisite association
Facies L
Peridotite with continuous basal Cr-spinel seam
Facies M
Peridotite with continuous upper Cr-spinel seam
Facies N
Peridotite with continuous bounding Cr-spinel seams
Facies O
Intra-harrisite Cr-spinel seams
Also non-layer parallel
Facies P
Discordant harrisite layer
Vertical to near-vertical
Cross-cuts layering
Facies Q
Pyroxene-rich peridotite (granular-textured and harrisitic)
Facies R
Heavily veined peridotite (plagioclase veins)
Cr-spinel seams
Continuous
Locally discontinuous
Chromitite
Diffuse zone (layer rich in Cr-spinel)
Granular-textured peridotite
Normal (Granular-textured)
Foliated
Porphyritic
Pyroxene-rich (>10% clinopyroxene intercumulus)
Harrisite
Non-layer parallel
Highly skeletal
Hopper (Stubby skeletal)

Figure 4

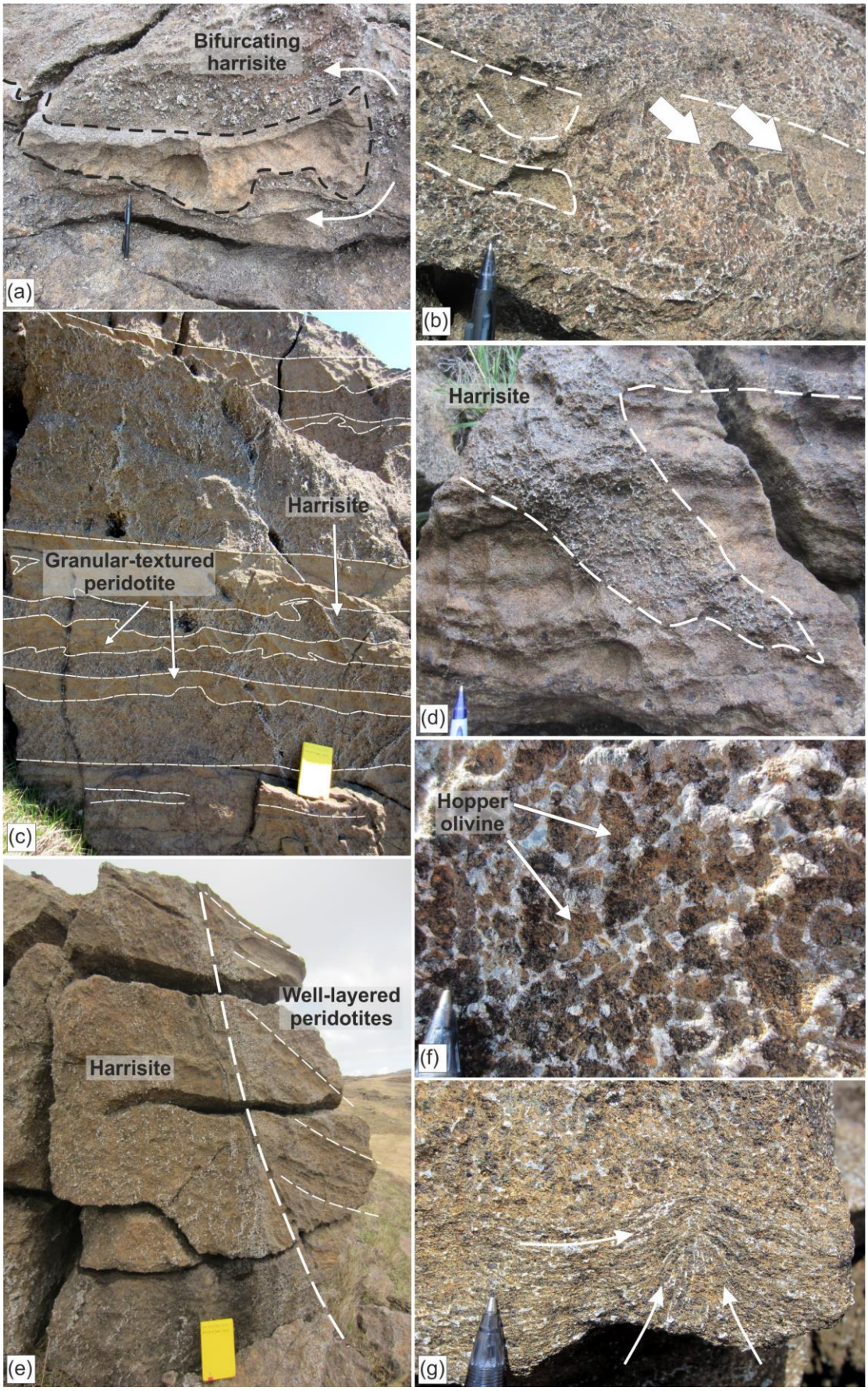


Figure 4 continued.

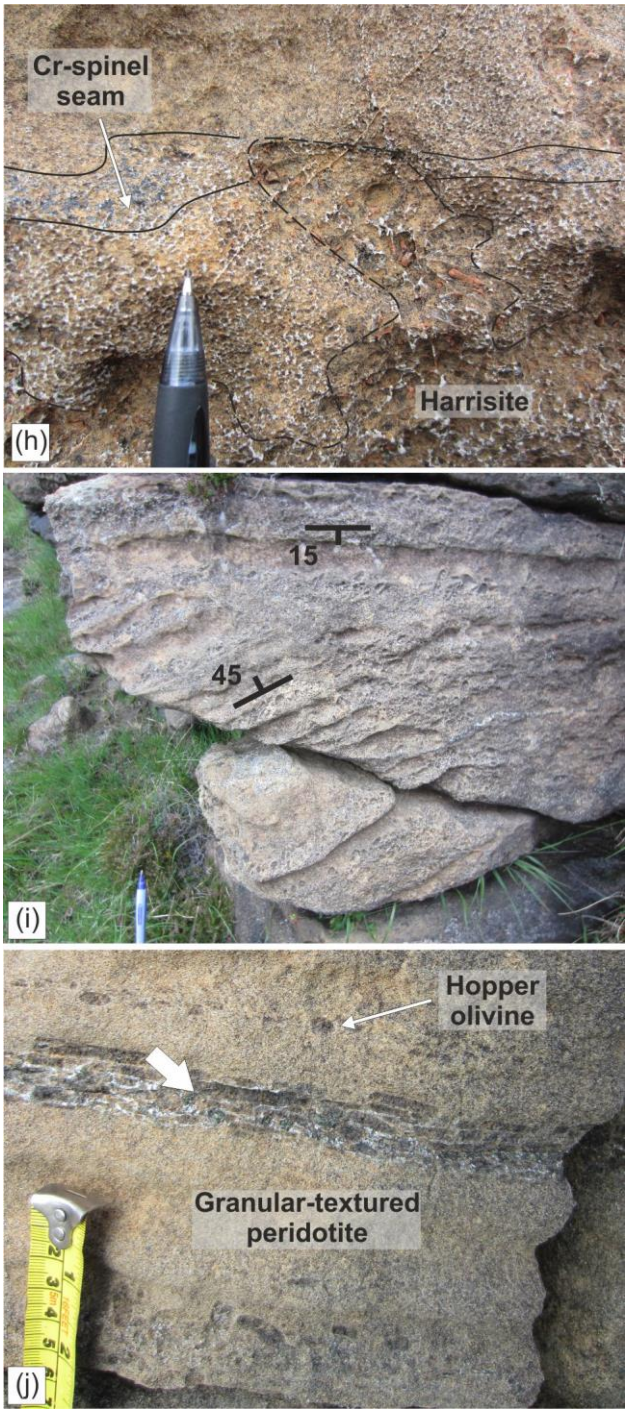
Cr-spinel seam
Harrisite
(h)
15
45
(i)
Hopper olivine
Granular-textured peridotite
(j)

Figure 5

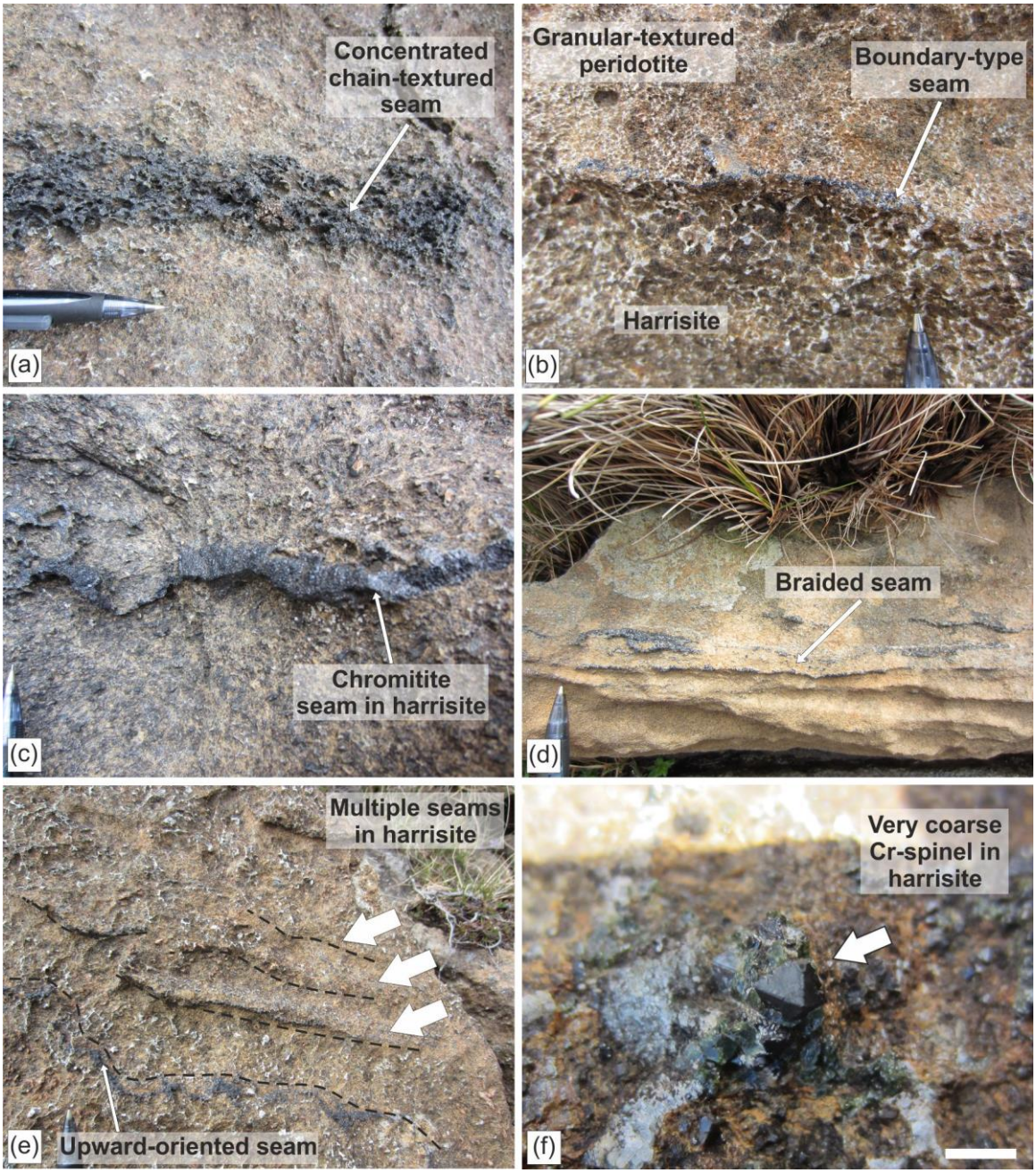
Concentrated chain-textured seam
(a)
Granular-textured peridotite
Boundary-type seam
Harrisite
(b)
Chromitite seam in harrisite
(c)
Braided seam
(d)
Multiple seams in harrisite
(e)
Upward-oriented seam
Very coarse Cr-spinel in harrisite
(f)

Figure 6

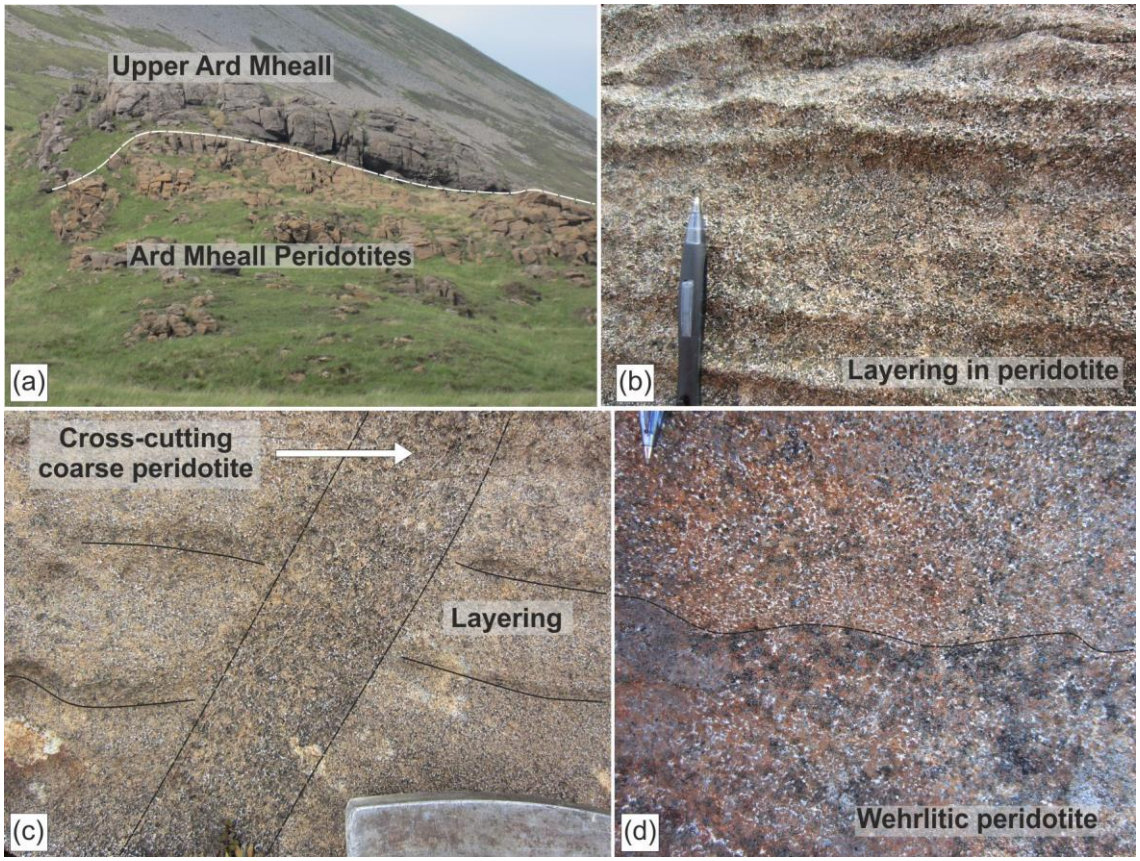
Upper Ard Mheall
Ard Mheall Peridotites
(a)
(b)
Layering in peridotite
Cross-cutting
coarse peridotite
Layering
(c)
(d)
Wehrlitic peridotite

Figure 7

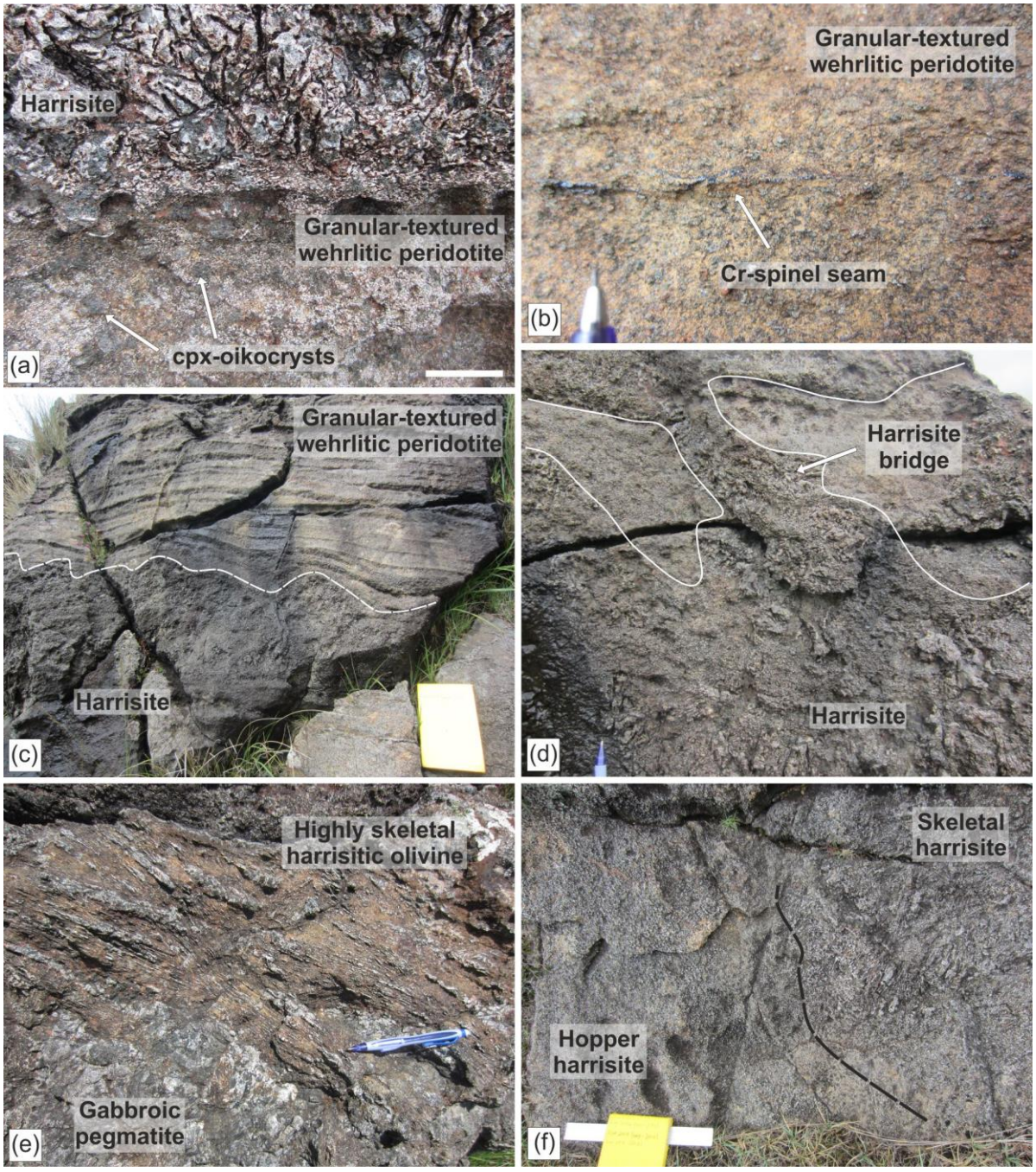
Harrisite
Granular-textured wehrlitic peridotite
cpx-oikocrysts
(a)
Granular-textured wehrlitic peridotite
Cr-spinel seam
(b)
Granular-textured wehrlitic peridotite
Harrisite
(c)
Harrisite bridge
Harrisite
(d)
Highly skeletal harrisitic olivine
Gabbroic pegmatite
(e)
Skeletal harrisite
Hopper harrisite
(f)

Figure 8


Gabbro
Melagabbro
Harrisite
(a)
(b)
(c)
(d)
Melagabbro
Gabbro
(e)
Leucogabbro
Olivine-gabbro
(f)

Figure 9

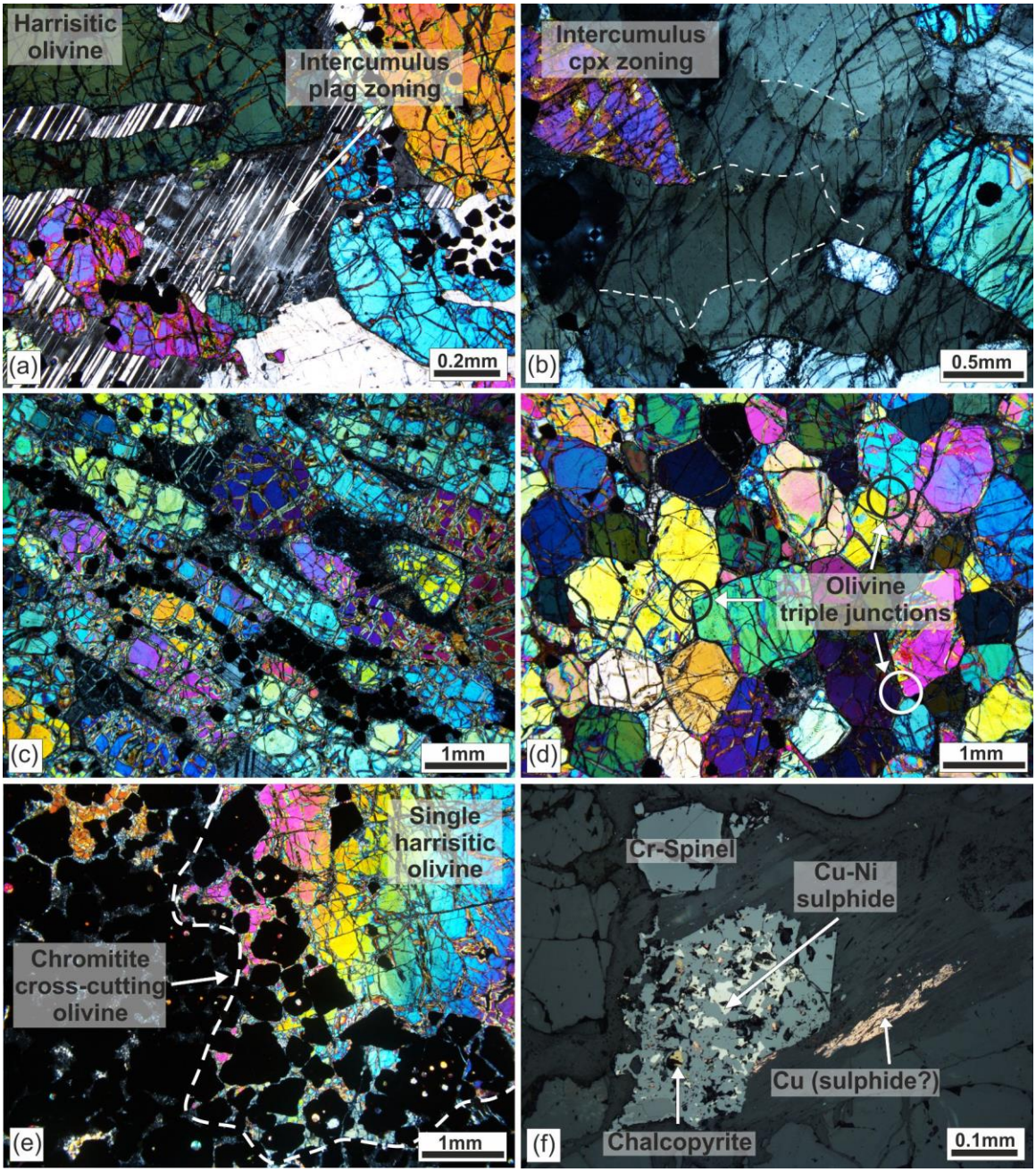
Harrisitic olivine
Intercumulus plag zoning
(a)
0.2mm
Intercumulus cpx zoning
(b)
0.5mm
(c)
1mm
Olivine triple junctions
(d)
1mm
Single harrisitic olivine
Chromitite cross-cutting olivine
(e)
1mm
Cr-Spinel
Cu-Ni sulphide
Cu (sulphide?)
Chalcopyrite
(f)
0.1mm

Figure 10

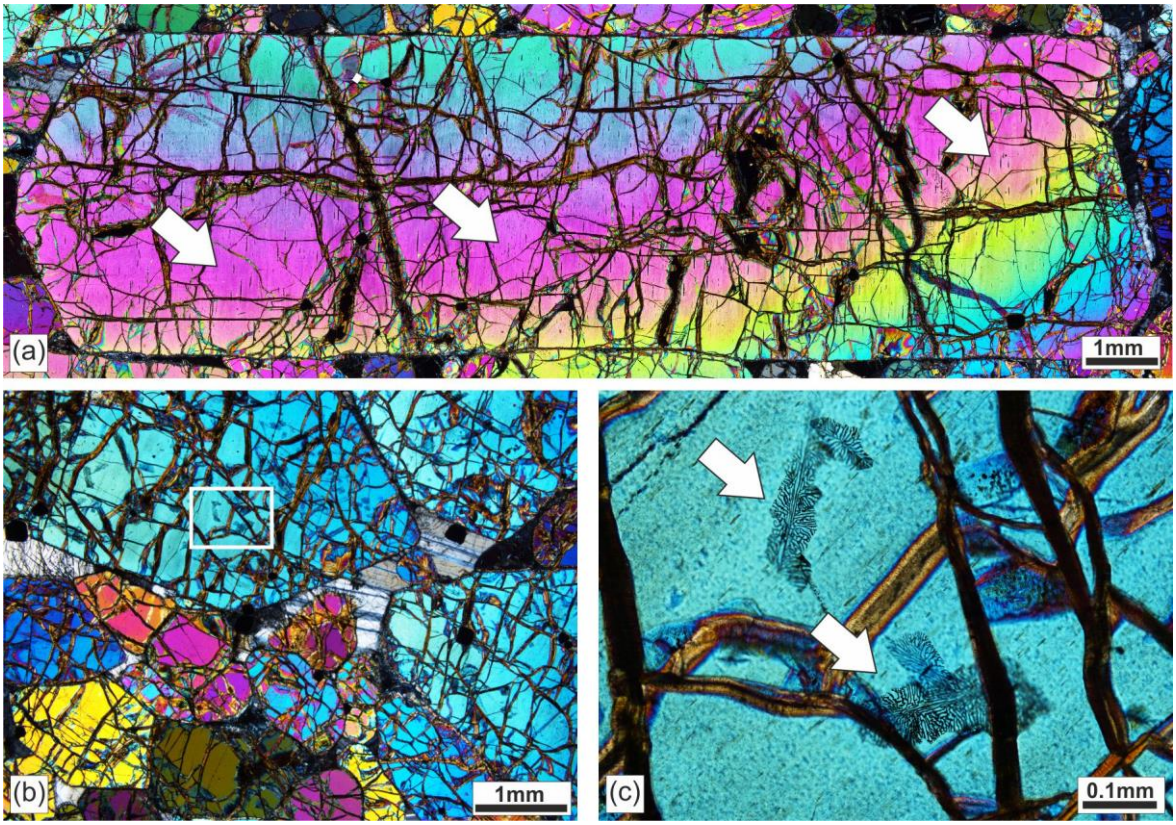


Figure 11

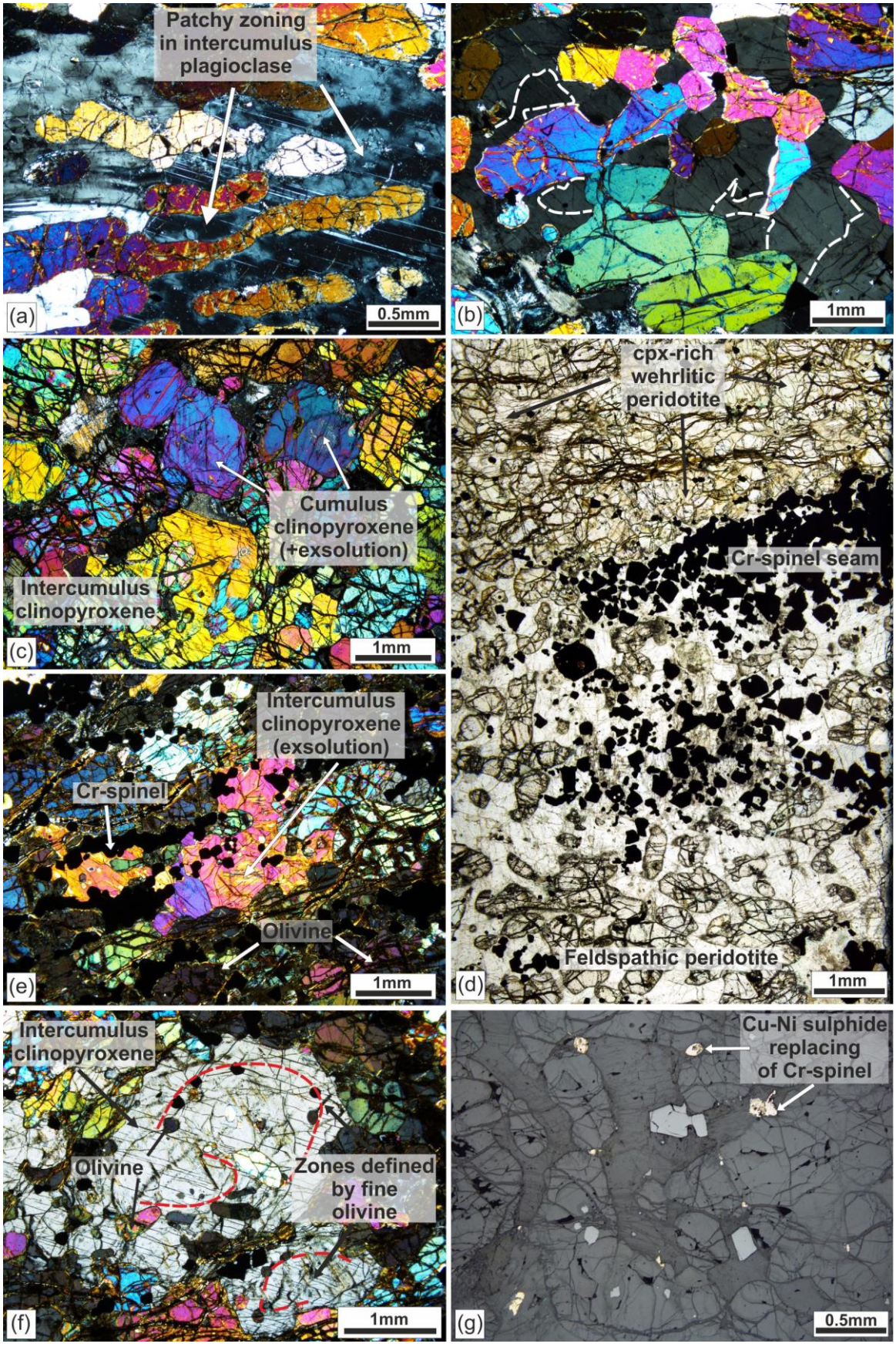
Patchy zoning in intercumulus plagioclase
(a)
0.5mm
(b)
1mm
Cumulus clinopyroxene (+exsolution)
Intercumulus clinopyroxene
(c)
1mm
cpx-rich wehrlitic peridotite
Cr-spinel seam
Feldspathic peridotite
(d)
1mm
Intercumulus clinopyroxene (exsolution)
Cr-spinel
Olivine
(e)
1mm
Intercumulus clinopyroxene
Olivine
Zones defined by fine olivine
(f)
1mm
Cu-Ni sulphide replacing of Cr-spinel
(g)
0.5mm

Figure 12

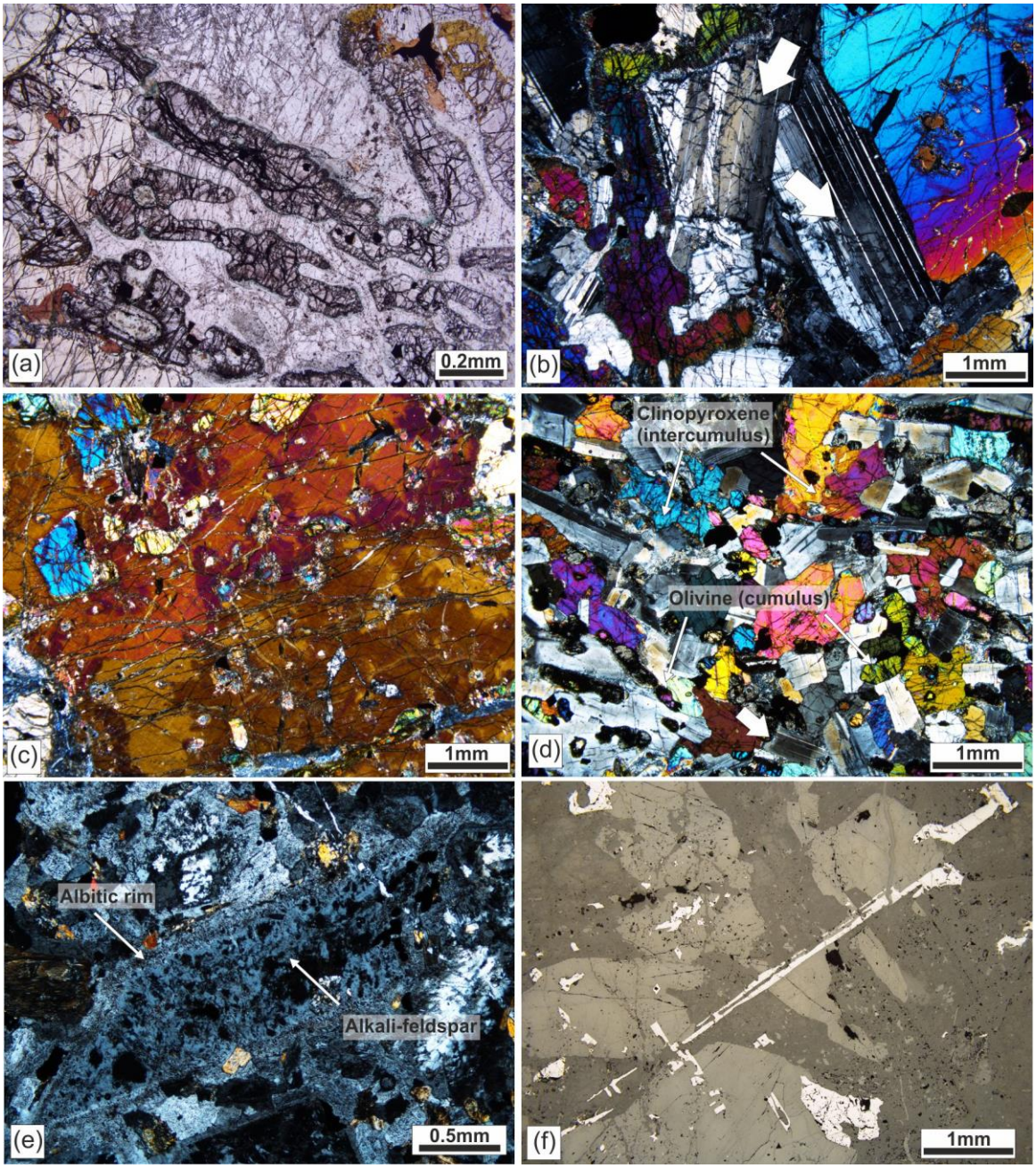
(a)
0.2mm
(b)
1mm
(c)
1mm
Clinopyroxene
(intercumulus)
Olivine (cumulus)
(d)
1mm
Albitic rim
Alkali-feldspar
(e)
0.5mm
(f)
1mm

Figure 13

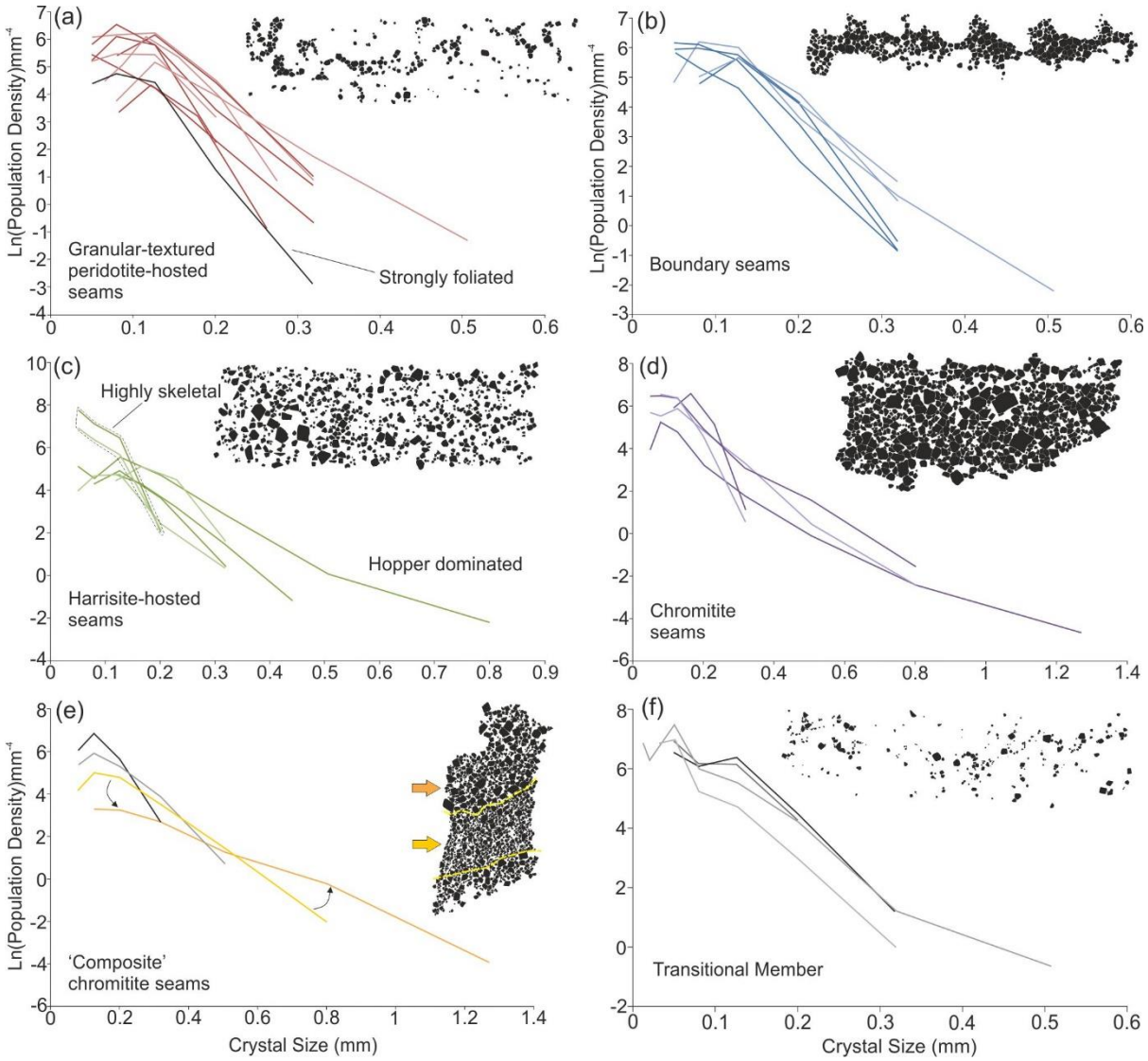
(a)
Ln(Population Density)mm⁻⁴
Granular-textured peridotite-hosted seams
Strongly foliated
(b)
Boundary seams
(c)
Highly skeletal
Hopper dominated
Harrisite-hosted seams
(d)
Chromitite seams
(e)
'Composite' chromitite seams
Crystal Size (mm)
(f)
Transitional Member
Crystal Size (mm)

Figure 14

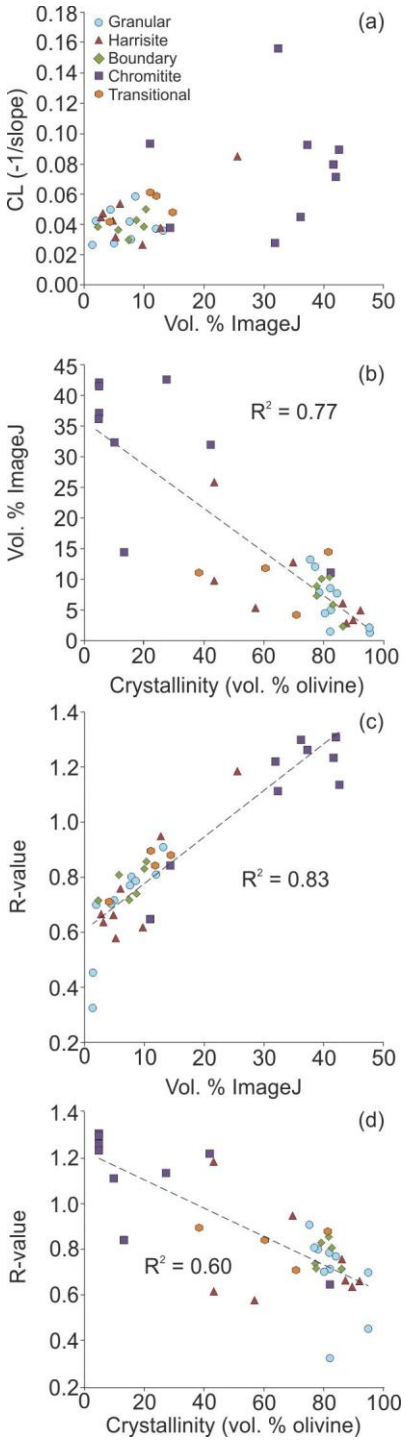
(a)
Granular
Harrisite
Boundary
Chromitite
Transitional
CL (-1/slope)
Vol. % ImageJ
(b)
R² = 0.77
Vol. % ImageJ
Crystallinity (vol. % olivine)
(c)
R² = 0.83
R-value
Vol. % ImageJ
(d)
R² = 0.60
R-value
Crystallinity (vol. % olivine)

Figure 15

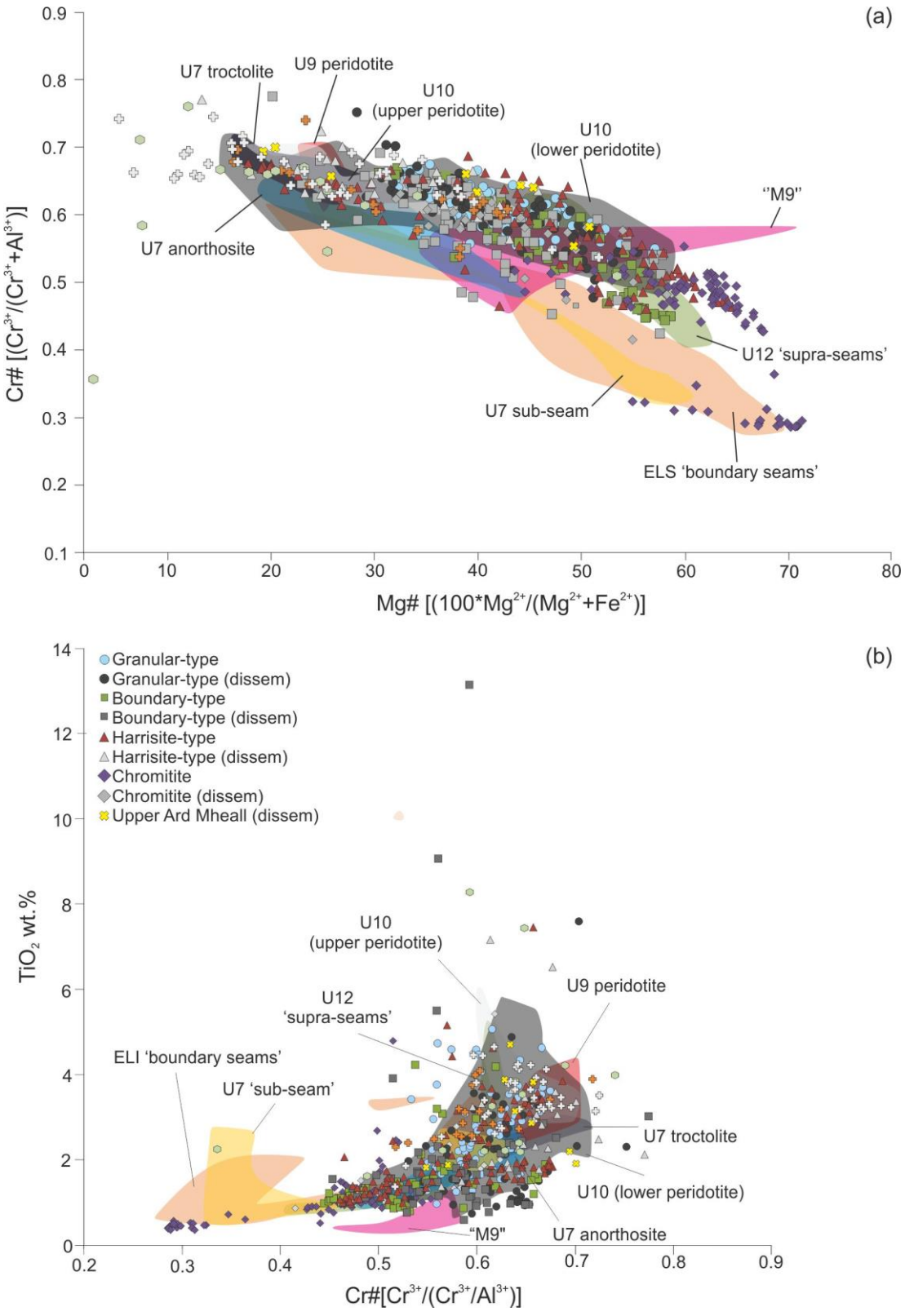
(a)
U7 troctolite
U9 peridotite
U10
(upper peridotite)
U10
(lower peridotite)
''M9''
U7 anorthosite
U12 'supra-seams'
U7 sub-seam
ELS 'boundary seams'
Cr# [(Cr3+/(Cr3+ +Al3+)]
Mg# [(100*Mg2+/(Mg2+ +Fe2+)]
(b)
Granular-type
Granular-type (dissem)
Boundary-type
Boundary-type (dissem)
Harrisite-type
Harrisite-type (dissem)
Chromitite
Chromitite (dissem)
Upper Ard Mheall (dissem)
U10
(upper peridotite)
U9 peridotite
U12
'supra-seams'
ELI 'boundary seams'
U7 'sub-seam'
U7 troctolite
U10 (lower peridotite)
"M9"
U7 anorthosite
TiO2 wt.%
Cr#[Cr3+/(Cr3+/Al3+)]

Figure 16

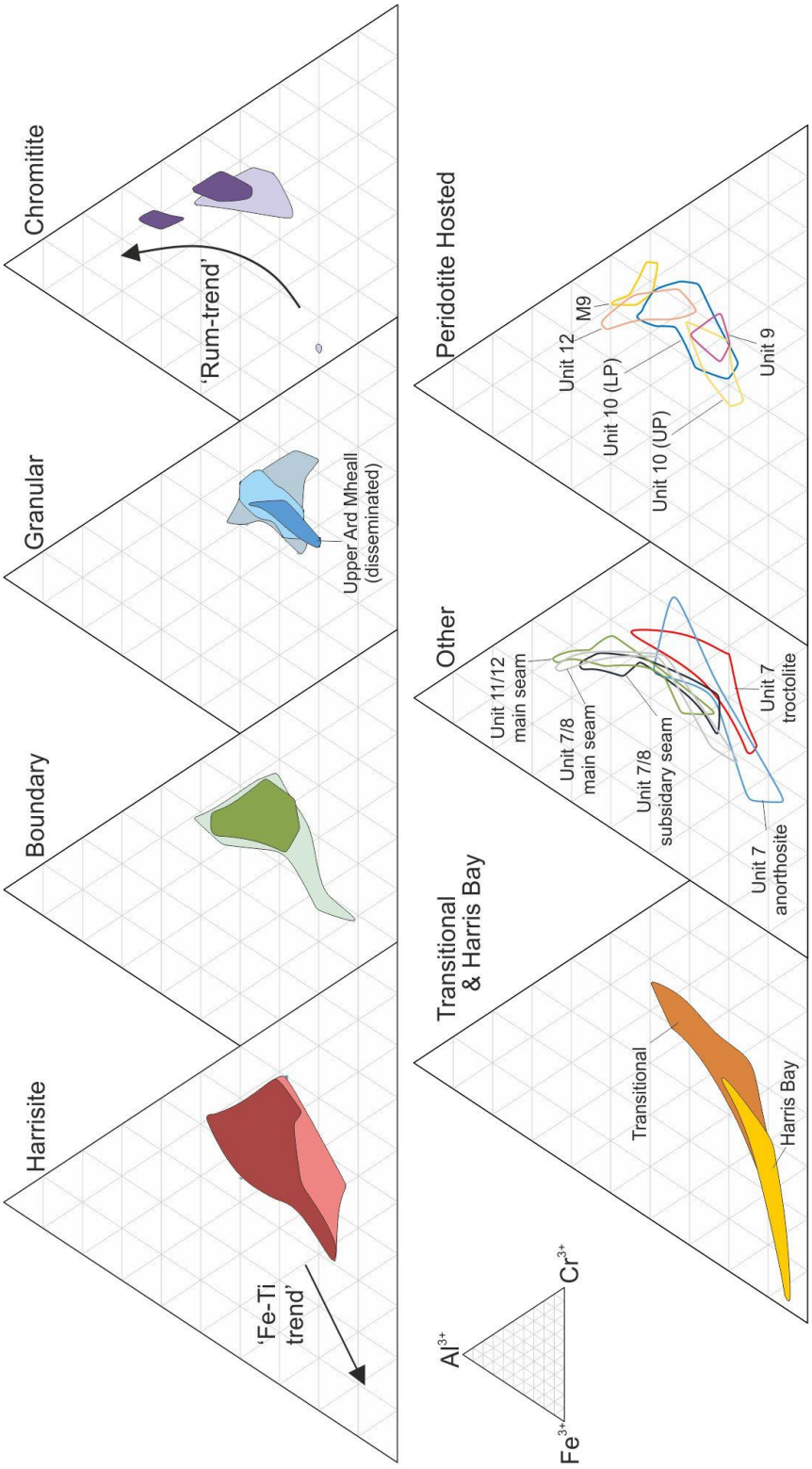
Chromitite
'Rum-trend'
Granular
Upper Ard Mheall (disseminated)
Boundary
Harrisite
'Fe-Ti trend'
Peridotite Hosted
Unit 12
M9
Unit 10 (LP)
Unit 10 (UP)
Unit 9
Other
Unit 11/12 main seam
Unit 7/8 main seam
Unit 7/8 subsidary seam
Unit 7 troctolite
Unit 7 anorthosite
Transitional & Harris Bay
Transitional
Harris Bay
Al3+
Cr3+
Fe3+

Figure 17

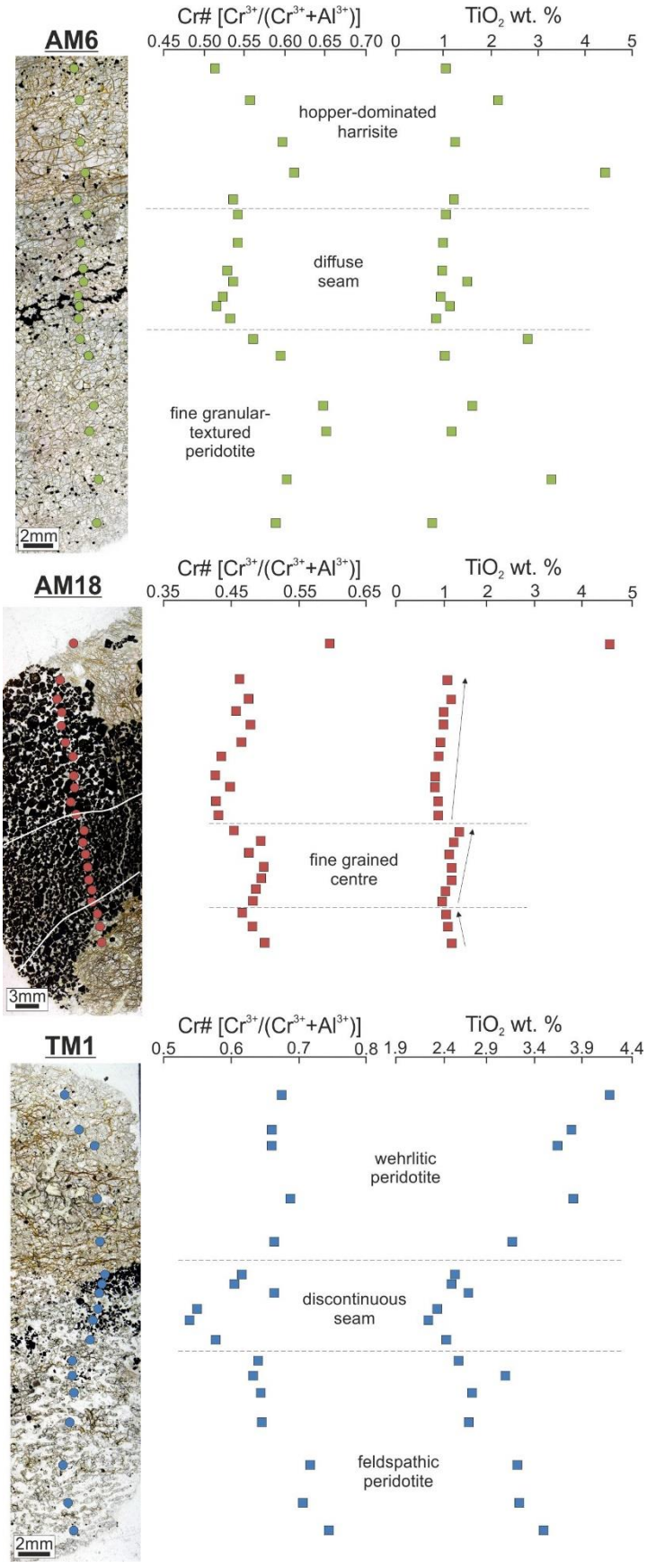
AM6
Cr# [Cr3+/(Cr3++Al3+)]
0.45 0.50 0.55 0.60 0.65 0.70
TiO2 wt. %
0 1 2 3 4 5
hopper-dominated harrisite
diffuse seam
fine granular-textured peridotite
2mm
AM18
Cr# [Cr3+/(Cr3++Al3+)]
0.35 0.45 0.55 0.65
TiO2 wt. %
0 1 2 3 4 5
fine grained centre
3mm
TM1
Cr# [Cr3+/(Cr3++Al3+)]
0.5 0.6 0.7 0.8
TiO2 wt. %
1.9 2.4 2.9 3.4 3.9 4.4
wehrlitic peridotite
discontinuous seam
feldspathic peridotite
2mm

Figure 18

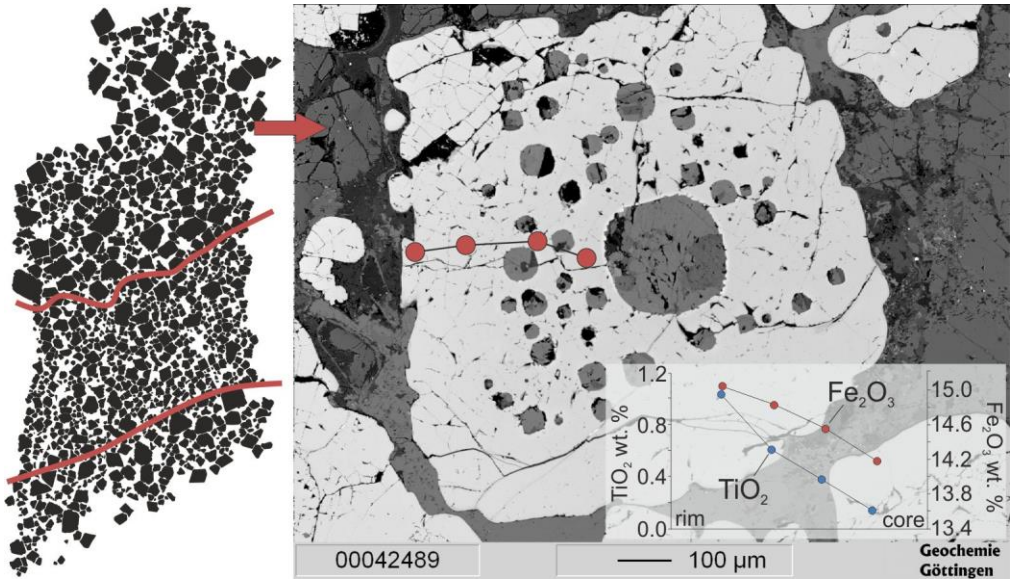
1.2
0.8
0.4
0.0
TiO2 wt. %
Fe2O3
TiO2
rim
core
15.0
14.6
14.2
13.8
13.4
Fe2O3 wt. %
00042489
100 µm
Geochemie
Göttingen

Figure 19

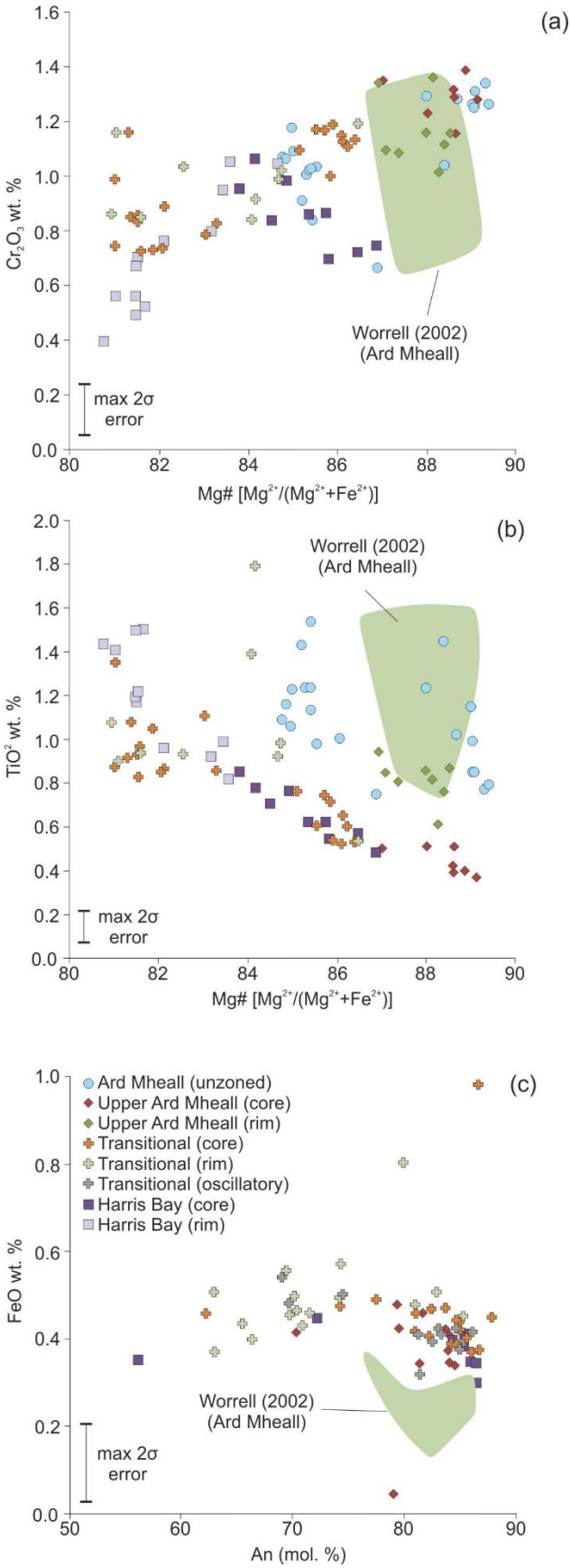
(a)
$Cr_2O_3$ wt. %
Mg# [$Mg^{2+}$/($Mg^{2+}$+$Fe^{2+}$)]
Worrell (2002)
(Ard Mheall)
max 2σ
error
(b)
$TiO^2$ wt. %
Mg# [$Mg^{2+}$/($Mg^{2+}$+$Fe^{2+}$)]
Worrell (2002)
(Ard Mheall)
max 2σ
error
(c)
Ard Mheall (unzoned)
Upper Ard Mheall (core)
Upper Ard Mheall (rim)
Transitional (core)
Transitional (rim)
Transitional (oscillatory)
Harris Bay (core)
Harris Bay (rim)
FeO wt. %
An (mol. %)
Worrell (2002)
(Ard Mheall)
max 2σ
error

Figure 20

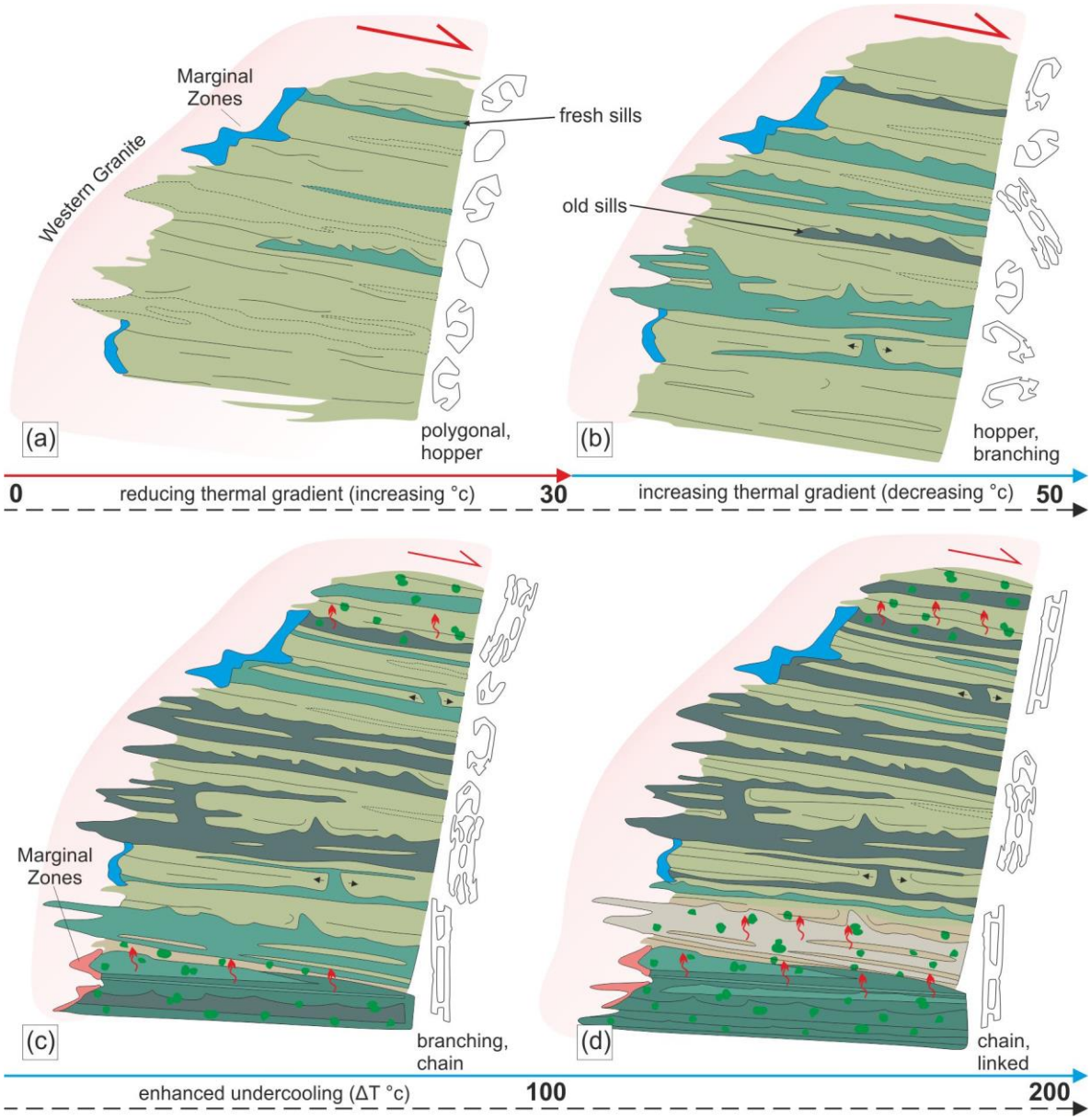
Marginal
Zones
Western Granite
fresh sills
old sills
(a)
polygonal,
hopper
(b)
hopper,
branching
0
reducing thermal gradient (increasing °c)
30
increasing thermal gradient (decreasing °c)
50
Marginal
Zones
(c)
branching,
chain
(d)
chain,
linked
enhanced undercooling (ΔT °c)
100
200

Figure 21

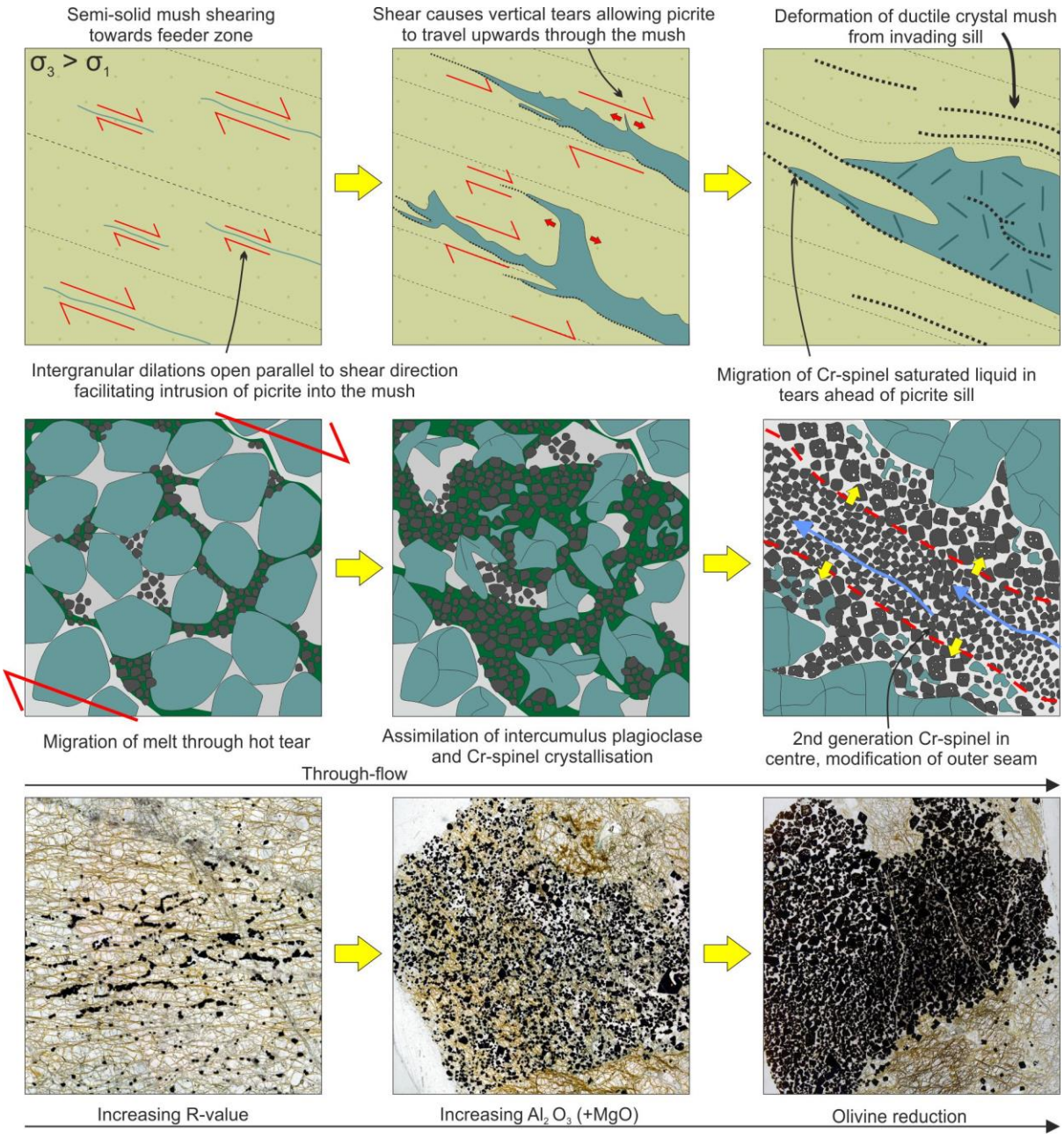
Semi-solid mush shearing towards feeder zone
$\sigma_3 > \sigma_1$
Shear causes vertical tears allowing picrite to travel upwards through the mush
Deformation of ductile crystal mush from invading sill
Intergranular dilations open parallel to shear direction facilitating intrusion of picrite into the mush
Migration of Cr-spinel saturated liquid in tears ahead of picrite sill
Migration of melt through hot tear
Assimilation of intercumulus plagioclase and Cr-spinel crystallisation
2nd generation Cr-spinel in centre, modification of outer seam
Through-flow
Increasing R-value
Increasing $Al_2O_3$ (+MgO)
Olivine reduction